Spin-orbit interaction and gate operation in custom-tailored InAlAs-based two-dimensional electron systems

DISSERTATION

ZUR ERLANGUNG DES DOKTORGRADES
DER NATURWISSENSCHAFTEN (DR. RER. NAT)

DER FAKULTÄT FÜR PHYSIK
DER UNIVERSITÄT REGENSBURG

vorgelegt von
Michael Prager
aus Viechtach

im Jahr 2022

Das Promotionsgesuch wurde eingereicht am 15.06.2022.

Die Arbeit wurde angeleitet von Prof. Dr. Dominique Bougeard.

Prüfungsausschuss:
Vorsitzender: Prof. Dr. John Schliemann
1. Gutachter: Prof. Dr. Dominique Bougeard
2. Gutachter: Prof. Dr. Mariusz Ciorga
Weiterer Prüfer: Prof. Dr. Sergey Ganichev

Contents

1. Introduction

Due to the ongoing rapid increase of performance requirements for computational circuitry, the semiconductor industry faces crucial challenges regarding the operational principle of future computation. The traditionally utilized 'classical' bit based on charge transport offers large scalability however the computation rate is stretched to its limits. This has fueled research in fundamental physics with the objectives to develop novel concepts, both for more efficient 'classical' computing and for computation beyond the 'classical' bit. A prominent candidate for a more efficient computing is the field of the so-called spintronics [1], where the spin degree of freedom in the form of spin currents is envisaged to replace charge currents as the vector of information. Very timely regarding novel ways of computing is the field of quantum computing, where a quantum mechanical two-level system is envisaged as the computation basis. These 'novel bits' are so-called quantum bits (qubits). Several principles and platforms were proposed for the realization of such qubits. A superconducting qubit recently demonstrated quantum supremacy [2] over the 'classical' computation for the first time. Two further qubit concepts also target the spin of the charge carrier in a solid state system: one based on the manipulation of spin of charge carriers in semiconductors [3] and a second on the topological nature of Majorana modes [4].

The aspiration to be able to build all-electrically controlled devices for these fields of applications of the spin degree of freedom has put a fundamental phenomenon of solid-state physics on top of the map: the spin-orbit interaction (SOI), which emerges from the bandstructure and crystal symmetries, in particular in semiconductor heterostructures. Indeed, this coupling of spin to charge carrier momentum allows an access to the spin degree of freedom via electrical fields. Hence this allows the operation through gated devices in semiconductor heterostructures, opening up the field of the so called spin-orbitronics. Majorana mode-based qubits rely on the interplayer of a semiconductor two-dimensional electron system (2DES) with strong SOI coupled to a superconductor [5], whereas Datta and Das [6] proposed the so-called all-electrical spin transistor in a 2DES with strong SOI, which could render 'classical' computing more efficient.

Since the novel description of SOI effects in low-dimensional carrier systems by Dresselhaus [7] and Bychkov, Yu and Rashba [8] especially indium-based heterostructures emerged as promising candidates due to their large intrinsic SOI. Specifically, 2DESs in QWs with InAlAs-based barriers were demonstrated as a versatile platform. The general questions in the field of spin-orbitronics, such as possibilities to tailor and maximize the SOI emerging from the crystal properties, but also the manipulation of spins via electric fields, have been addressed in this heterostructure platform over the recent years [9–17]. This includes a first proof-of-principle basis for the all-electrical spin transistor [18] and topological superconductivity with the observation of Majorana zero modes [5, 19–22]. As gating reflects a control parameter of the Rashba-type SOI while it is at the same time a tool to investigate the SOI in the systems, it has been frequently used in this context in these systems [10–14, 23–29]. However, literature is lacking a consensus of how experimentally observed SOI and gate response characteristics in similarly designed gated heterostructures [23–29] may be linked to heterostructure design and materials properties. This poses the question of the origin of these discrepancies.

In this thesis, we utilize molecular beam epitaxy (MBE) to design the heterostructures, allowing us to custom-tailor the bandstructure, where we characterize and investigate the parameters defining the gating and the SOI of MBE-grown InAlAs-based heterostructures via magnetotransport at low temperatures. This thesis is structured as follows:
Ch. 2 briefly describes the essential theoretical concepts necessary to assess and follow the experiments and its interpretations presented over the course of this thesis. This includes very generally the realization of and the magnetotransport in a 2DES for weak and strong magnetic fields. In this context, quantum interference corrections are introduced as well as the concept of gating in a 2DES. This chapter then concludes with the description of SOI and how it can be characterized via magnetotransport experiments. Subsequently following is a presentation of the experimental methods and setups in Ch. 3, elucidating briefly MBE growth of In-based III/V semiconductors and crystal characterization concepts before a short application-oriented overview of the magnetotransport is elaborated. Ch. 4 comprises a short discussion of the challenges arising with the calibration of the indium concentration in In-based MBE-grown heterostructures. Ch. 5 presents an extensive experimental study of the gate response of top-gated 2DES confined in InAlAs-embedded InGaAs QWs. We deduce a phenomenological microscopic model based on our experiments which we are able to explain and predict observed features in the gate response. Our model highlights the crucial role of intrinsic InAlAs defect states in the electrostatics in gated heterostructures. We elucidate gate-operation strategies to bring the 2DES from a metastable situation into the classical field-effect range. This chapter concludes with design discussions regarding the indium concentration and the depth of the QW in favor of enhanced gate response and stable operation. Along with the gate response findings in the previous chapter, we focus in Ch. 6 on the Rashba-type SOI in various InAlAs embedded QW designs. In particular we elucidate the separation of the Rashba parameter into a contribution from the electrostatics in the heterostructure and the interfaces within the QW. Custom-tailoring the bandstructure allows us to investigate impacts from specific changes in the heterostructure. Ch. 7 elaborates the influence of external electric fields from top- and backgate on the SOI. The first part of this chapter presents a extensive study of the backgate response of a 2DES, from which the second part illustrates the impact on the SOI for separately operated gates as well as for a dual-gated configuration. The conclusive discussion and evaluation of the results is given in Ch. 8, highlighting the importance of the intrinsic InAlAs defect states in the design process of InAlAs-containing devices for spin-orbitronic applications. The appendices briefly present a first attempt of Sb-incorporation in the QW in App. B and a detailed overview of the peculiar details in the growth of a InAlAs step-graded buffer in App. C.

2. Theoretical concepts

This chapter presents the fundamentals of the theoretical background relevant in this study. We illustrate the basics of magnetotransport in two-dimensional III/V semiconductor electron systems, particularly in InAs-based ternary alloy heterostructures. This electron system allows for a tunability based on the field effect while it inherits a strong spin-orbit interaction (SOI) which can be characterized by peculiarities arising in the magnetotransport.

2.1. Magnetotransport in a two-dimensional electron gas

We characterize the samples discussed in this thesis via analysis of magnetotransport. This section introduces the concept of a two-dimensional electron system for which we apply an electric field featuring electron transport for small and large magnetic fields.

2.1.1. The two-dimensional electron gas

Electrons moving freely in all three dimensions x, y and z in a crystal lattice can be described by means of $\mathbf{k} \cdot \mathbf{p}$—perturbation theory from the Bloch equation with the dispersion relation

$$E_c(\mathbf{k}) \approx E_c + \frac{\hbar^2 \mathbf{k}^2}{2m_e^*}, \tag{2.1}$$

with the wave vector $\mathbf{k}$, minimum of the conduction band E_c and the effective electron mass m_e^*. However by confining the motional degree of the electron in one direction leaves the electron to move freely perpendicular to this direction in the plane spanned by the other two directions, thus creating a so-called two-dimensional electron system. We realize this electron confinement via band engineering in a semiconductor heterostructure. By creating an interface of two distinctive materials with different energy bandgaps we introduce a confinement potential in the growth direction z. We extend this single interface to a so-called quantum well (QW) structure by embedding a low-bandgap material like InGaAs and InAs into InAlAs, which is characterized by a much higher bandgap energy. When only the lowest of the quantized energy subbands is populated, the system is then characterized as effectively two-dimensional and thus called a two-dimensional electron system (2DES). Each subband state n in the 2DES can then by described in the framework of the envelope function approximation by

$$\psi_{n,\mathbf{k}}(x, y, z) = \phi_{n,\mathbf{k}}(x, y) \cdot \xi_n(z), \tag{2.2}$$

where $\phi_{n,\mathbf{k}}(x, y) \propto e^{i(k_x x + k_y y)}$ represents the free motion in the xy-plane by Bloch waves, while $\xi_n(z)$ characterizes the confinement potential in z-direction. The dispersion relation then is parabolic and can be written as

$$E_n(\mathbf{k}_{||}) = E_n + \frac{\hbar \mathbf{k}_{||}^2}{2m_e^*}, \tag{2.3}$$

for which $\mathbf{k}_{||} = \sqrt{k_x^2 + k_y^2}$ is the in-plane wave vector. The resulting density of states (DOS) in the 2DES is then constant (independent of the energy due to the parabolic dispersion) for each subband n and can be written as

$$D_{2D}(E) = \frac{g_s g_v m_e^*}{2\pi\hbar^2}, \tag{2.4}$$

with the degree of spin degeneracy g_s and the valley degeneracy of conduction band minima g_v. For the InAlAs-based heterostructures we use in this thesis, we can apply $g_s = 2$ and $g_v = 1$ [30]. The electron sheet density n_s of the 2DES can be written as

$$n_s = D_{2D}(E) \cdot E_F, \tag{2.5}$$

where the Fermi energy E_F corresponds to the highest occupied energy state of the system. Accordingly, the corresponding states are occupied up to the Fermi wave vector

$$k_F = \sqrt{\frac{2m_e^* E_F}{\hbar^2}} = \sqrt{\frac{4\pi n_s}{g_s g_v}} = \sqrt{2\pi n_s}. \tag{2.6}$$

2.1.2. Drude model

The description of the motion of electrons in a 2DES is given by the Drude model [30, 31]. In this semi-classical model, the electrons are treated as a gas of free carriers. Their motion is dominated by elastic scattering on lattice atoms or other carriers characterized by the mean transport scattering time τ_{tr}. By applying an electric field $\mathbf{E}$, the electrons gain, on average between scattering events, the so-called drift velocity $\mathbf{v}_D$. From this, the current density $\mathbf{j}$ is determined as

$$\mathbf{j} = \sigma\mathbf{E} = -en_s\mu\mathbf{E} = -en_s\mathbf{v}_D, \tag{2.7}$$

with the electrical conductivity σ and the electron mobility

$$\mu = \frac{|e|\tau_{tr}}{m_e^*}. \tag{2.8}$$

In a magnetic field $\mathbf{B} = (0, 0, B)$ oriented in z-direction perpendicular to the 2DES motion, electrons are deflected by the Lorentz force. B is chosen so that quantum phenomena are negligible, i.e. $\omega_c\tau_{tr} \ll 1$ with the cyclotron frequency

$$\omega_c = \frac{|e|B}{m_e^*}. \tag{2.9}$$

The equation of motion in steady state can then be written as

$$\frac{m_e^*}{\tau_{tr}}\mathbf{v}_D = -e\left(\mathbf{E} + \mathbf{v}_D \times \mathbf{B}\right). \tag{2.10}$$

With this configuration, σ transforms into a 2×2 tensor $\boldsymbol{\sigma}$ for which the current density is determined as

$$\begin{pmatrix} j_x \\ j_y \end{pmatrix} = \begin{pmatrix} \sigma_{xx} & \sigma_{xy} \\ \sigma_{yx} & \sigma_{yy} \end{pmatrix} \cdot \begin{pmatrix} E_x \\ E_y \end{pmatrix}. \tag{2.11}$$

Due to symmetry arguments in isotropic systems, the components of the conductivity tensor $\boldsymbol{\sigma}$ can be combined as $\sigma_{xx} = \sigma_{yy}$ and $\sigma_{xy} = -\sigma_{yx}$. The electrical resistivity tensor $\boldsymbol{\rho} = \boldsymbol{\sigma}^{-1}$ can be calculated by tensor inversion, resulting in the components

$$\rho_{xx} = \quad \rho_{yy} = \frac{\sigma_{xx}}{\sigma_{xx}^2 + \sigma_{xy}^2} = \frac{m_e^*}{n_s e^2 \tau_{tr}}, \tag{2.12}$$

$$\rho_{xy} = -\rho_{yx} = \frac{\sigma_{xy}}{\sigma_{xx}^2 + \sigma_{xy}^2} = \frac{B}{|e| n_s}. \tag{2.13}$$

The longitudinal resistivity component ρ_{xx} is independent of B and determined by the transport scattering time τ_{tr}, thus directly limiting the mobility of the system. The Hall resistivity ρ_{xy} however depends linearly on B.

Based on these Eq. 2.12 and 2.13, the essential properties which characterize the system, the electron sheet density n_s and the electron mobility, can be derived as

$$n_s = \left(e \cdot \left. \frac{\mathrm{d}\rho_{xy}}{\mathrm{d}B} \right|_{B=0} \right)^{-1}, \tag{2.14}$$

$$\mu = \left(e \cdot n_s \cdot \rho_{xx} \left(B = 0 \right) \right)^{-1}. \tag{2.15}$$

2.1.3. Landau quantization

When the applied magnetic field increases up to $\omega_c \tau_{tr} > 1$, the semi-classical description of the magnetotransport within the Drude model breaks down. The density of states evolves as a result of the Bohr-Sommerfeld quantization of self-interfering carriers [30] into a series of Landau levels (LL) represented by $\delta-$peaks, energetically separated by $\hbar\omega_c$. As a consequence, the system transitions into a fully quantized system (spatial confinement in z and Landau quantization in x, y). The quantized energy states characterized by the Landau quantum number n are given by

$$E_n = \hbar\omega_c \left(n + \frac{1}{2} \right). \tag{2.16}$$

The LLs in real systems experience a Lorentzian-type of broadening due to scattering with impurities in the system. They are highly degenerate. The number of states in each LL per unit area can be determined as

$$N_{LL} = \frac{|e| B g_s}{h}, \tag{2.17}$$

obeying the spin degeneracy g_s of the system. The LL filling factor ν, yielding the amount of populated LLs at a given magnetic field B, can be written as

$$\nu = \frac{n_s}{N_{LL}} = \frac{n_s h}{e B g_s}. \tag{2.18}$$

Here, spin levels are treated degenerate in each LL, however this degeneracy is lifted at higher magnetic fields by the Zeeman energy. As a result, each LL is characterized by two spin levels of states, up and down, such that $g_s = 1$. The Zeeman effect is further discussed later in this section.

Shubnikov-de Haas oscillations For a 2DES with a constant electron density n_s, the increase of the magnetic field B results in a decreasing number of occupied LLs as the number of states N_{LL} on each LL increases. As a consequence, E_F exhibits an oscillatory behavior which correspondingly results in a sinusodial oscillation of ρ_{xx} in $1/B$, known as Shubnikov-de Haas (SdH) oscillations. Coleridge *et al.* [32] gave a semi-classical description of $\rho_{xx}(B)$:

$$\rho_{xx}(B) = \rho_{xx}(0)\left[1 - 4 \cdot \exp\left(-\frac{\pi}{\tau_q} \cdot \frac{m_e^*}{eB}\right) \cdot \frac{\chi}{\sinh(\chi)} \cdot \cos\left(\frac{2\pi\xi}{\hbar}\frac{m_e^*}{eB} - \pi\right)\right], \tag{2.19}$$

with $\xi = E_F - E_n$, the quantum lifetime τ_q [32, 33] and the thermal damping factor $\chi = 2\pi^2 k_{\mathrm{B}} T / (\hbar\omega_c)$. The prefactor corresponds to the constant longitudinal resistivity described in the Drude model. This is then modulated with a description of a temperature-dependent DOS of the LLs with the Lorentzian energy broadening due to scattering. The exponential term $\exp\left(-\frac{\pi}{\tau_q} \cdot \frac{m_e^*}{eB}\right)$, commonly referred to as the Dingle factor, determines the amplitude of the SdH oscillations [30]. When the Fermi level lies between two subsequent LLs during a variation of B, a minimum in ρ_{xx} can be found. Accordingly when the Fermi level passes the center of the DOS of the topmost occupied LL, ρ_{xx} exhibits a maximum. Through evaluation of the neighbouring SdH minima i and $i+1$ in $1/B$ by means of Eq. 2.19, we can determine the electron sheet density n_s of the 2DES as follows:

$$\Delta\left(\frac{1}{B}\right) = \frac{1}{B_{i+1}} + \frac{1}{B_i} = \frac{g_s|e|}{hn_s}. \tag{2.20}$$

Quantum Hall effect Simultaneously, when minima in the SdH oscillations occur in ρ_{xx}, pronounced plateaus appear in the Hall (transversal) resistivity ρ_{xy}, known as the quantum Hall effect (QHE) [34, 35]. These plateaus exhibit well-defined values given by

$$\rho_{xy} = \frac{1}{\nu} \cdot \frac{h}{e^2} = \frac{1}{\nu} \cdot R_K, \tag{2.21}$$

with the von-Klitzing constant $R_K = h/e^2 = 25812.807\ \Omega$ [34]. The QHE can be explained within the Landauer-Büttiker formalism [36] by the existence of one-dimensional edge channels of a sample with finite size. When the Fermi level is in-between two LLs, i.e. an integer filling factor ν and a minima in ρ_{xx} (SdH oscillations), transport is carried only along these edge channels. They exhibit dissipationless and ballistic transport, spatially separated and counterpropagating at opposing sides of the sample due to localized states within the sample [30].

Zeeman effect An external magnetic field $\mathbf{B}$ lifts the spin degeneracy of each LL by the Zeeman energy

$$\Delta E_Z = g^* \cdot \mu_B \cdot B, \tag{2.22}$$

where g^* is the effective Landé g-factor and μ_B the Bohr magneton. As a consequence, the periodicity of the SdH oscillations is doubled in $1/B$ as well as observable QHE plateaus, due to now two spin levels per LL. In the experiments, this is only observable for $\Delta E_Z > k_{\mathrm{B}}T$. Note, that g^* is not a scalar but a tensor. The in- and out-of-plane anisotropy originates from the $\mathbf{k} \cdot \mathbf{p}-$coupling between different subbands in the 2DES. The in-plane anisotropy is predicted to scale with the strength of Dresselhaus SOI [37], which we find in Sec. 2.3.1 to be negligible in our heterostructures. Additionally, we solely apply out-of-plane magnetic fields in our experiments. This results in a negligible in-plane anisotropy, allowing us to treat g^* as a scalar. From the appearance of the doubled SdH frequency and T in the experiment, we are able to give an estimation for g^* for our system.

Magneto-intersubband scattering Over the course of this thesis, the electron density is adjusted with an external electric field (see Sec. 2.2). Within this, a population of the second size-quantized subband of the QW is not excludable. When that occurs, magnetotransport has to be treated with a contribution of the additional 2DES. Accordingly, this second 2DES adds another set of LL eigenenergies to Eq. 2.16, thus contributing as a second system to the SdH oscillations by means of Eq. 2.19. As a consequence, peculiar features in ρ_{xx} can arise, referred to as the magneto-intersubband scattering (MIS) effects [38]. This has to be taken into account for two spatially non-separated 2DESs, i.e. two populated subbands in a QW. When LLs of each of the subbands cross, an increased scattering between the subbands occurs. This LL crossing can be described with the following relation

$$E_1 + E_{LL,1} = E_2 + E_{LL,2} = E_1 + E_{1,2} + E_{LL,2}, \tag{2.23}$$

in which E_i represents the energetic onset of the first $i = 1$ and the second $i = 2$ subband of the QW, while $E_{1,2}$ describes their energy difference $E_{1,2} = |E_1 - E_2|$. $E_{LL,i}$ represents the LL energies of each of the subbands according to Eq. 2.16, for which Eq. 2.23 can then be written as

$$E_1 + \hbar\omega_c \left(n + \frac{1}{2}\right) = E_1 + E_{1,2} + \hbar\omega_c \left(m + \frac{1}{2}\right), \tag{2.24}$$

with n, m being the LL indices of the two subbands, n of the first and m of the second. Simplifying Eq. 2.24 to

$$(n - m) = \frac{m_e^*}{\hbar e} \cdot E_{1,2} \cdot \frac{1}{B} \tag{2.25}$$

then yields a magnetic field-dependent condition for the LL crossing in such a 2DES for which $n > m$ is always true. The resulting form of ρ_{xx} due to the MIS was described by means of Eq. 2.19 by [39, 40] as a system of two contributing SdH-terms with each a SdH frequency f_1 and f_2 in $1/B$ of the two subbands. A third term connects both and represents the MIS by introducing two additional frequencies $f_1 + f_2$ and $f_1 - f_2$. This manifests itself in the experiment as a beating pattern, characterized by the two additional frequencies in ρ_{xx}. A fast-Fourier-transform (FFT) analysis extracts the frequencies f_1 and f_2 of the two subbands.

2.1.4. Quantum interference correction: weak localization

Up to here, quantum mechanical scattering of carriers (electrons or holes) at individual impurities within a diffusive transport model was considered. As a consequence, coherent

motion between multiple scattering events was neglected. When we take the wave-character of the carriers into account, interference with themselves leads to quantum correction effects of the semi-classical Drude-like transport.
These considerations are based on time-reversed paths (in the 2D plane of motion) of two partial electron waves. By multiple scattering events on these paths, they return to the starting point and thus perform a loop. More simply said, the electrons experience backscattering. As the two paths are time-reversed, the propagation of the two partial waves is in opposite direction. The probability of return to the starting point can be written as

$$|A^+ + A^-|^2 = |A^+|^2 + |A^-|^2 + A^+A^{-*} + A^{+*}A^-, \tag{2.26}$$

with the quantum mechanical amplitude of each path, A^+ and A^- respectively [30, 41]. The first two terms in Eq. 2.26 represent the classical contribution to backscattering (considered in the Drude model), whereas the last two terms correspond to the interference of the partial electron waves at the start/end of the loop. At zero magnetic field, and thus with time-reversal symmetry, the two amplitudes can be written as

$$A^+ = A^- \equiv A, \tag{2.27}$$

by which the classical return probability P_{cl} (based on only the first two terms in Eq. 2.26) yields

$$P_{cl} = 2|A|^2, \tag{2.28}$$

while the corrected (quantum mechanical) return probability P_{qm} is given by

$$P_{qm} = 4|A|^2. \tag{2.29}$$

The doubled return probability due to the correction represents an enhanced backscattering because of constructive interference of the partial electron waves, denoted as weak localization (WL). This manifests experimentally in an increased ρ_{xx} at zero magnetic field. With the onset of a magnetic field, time-reversal symmetry is broken due to the addition of an Aharonov-Bohm phase $\phi_{AB} = 2\pi eBS/h$ to the amplitude. S denotes the area enclosed by the loop path. As a consequence, the amplitudes can be written as

$$A^\pm(B) = A\exp\{\pm i\phi_{AB}\}, \tag{2.30}$$

with which the return probability now yields

$$P = |A^+(B) + A^-(B)|^2 = 2|A|^2 + 2|A|^2\cos 4\pi\frac{eBS}{h}. \tag{2.31}$$

Due to the oscillating factor in P, the last term in Eq. 2.31 eventually averages out, yielding the classical return probability P_{cl}. As a result, the increase in ρ_{xx} decreases to the initial resistivity with increasing magnetic field.

2.2. The field effect

We are able to control the electron density in our 2DES by utilizing the so-called field effect. For this, we introduce a metallic plate as a gate electrode either on top (denoted as topgate) or beneath (denoted as backgate) of the 2DES, separated by insulating semiconductor barriers and dielectrics. With this, we create a situation similar to a parallel plate capacitor between the 2DES and the gate electrode. The 2DES is grounded via the applied source-drain voltage across the 2DES plane, while at the same time we apply the voltage V_{gate} across the gate electrode to ground. The capacitance C of a plate capacitor is determined by its charge Q on the plates and the applied voltage, here V_{gate}, which can then be written as

$$C = \frac{Q}{V_{gate}} = \epsilon_0 \epsilon_r \frac{A}{d}, \tag{2.32}$$

where ϵ_0 is the vacuum permittivity and ϵ_r the permittivity of the material in-between the plates. A represents the (effective) area of the capacitor plates and d the distance between the two plates. In our experiments, we characterize the response of the 2DES (in particular the electron sheet density n_s) to a variation of V_{gate} with the capacitive coupling c, given by

$$c = \frac{\partial n_s}{\partial V_{gate}} = \frac{C}{eA} = \frac{\epsilon_0 \epsilon_r}{ed}. \tag{2.33}$$

Our heterostructures typically have several different materials between the gate electrode and the 2DES (e.g. dielectric, semiconductor cap, semiconductor barrier), resulting in a series connection of individual capacitors i each with its own layer thickness d_i and permittivity ϵ_i. Thus, the total capacitive coupling c is given by

$$c = \frac{\epsilon_0}{e} \left(\sum_i \frac{d_i}{\epsilon_i} \right)^{-1}. \tag{2.34}$$

This is a classical description of the capacitor model, where we neglected two quantum mechanical contributions. First is the so-called quantum capacitance, which originates from an increased distance d between the gate electrode and the 2DES due to a significantly smaller DOS in the 2DES compared to the metallic plate. The second contribution takes the confinement energy in the QW into account, which modifies the z-extent of the wavefunction and thus has also an impact on the capacitive coupling. We can neglect these contributions in a good approximation, as both are significantly smaller than the classical contribution described in Eq. 2.34. A detailed description of the capacitive coupling including all contributions is given in [30].

2.3. Spin-orbit interaction (SOI)

The spatial motion of an electron in a crystal lattice and the spin of the electron are generally connected and can interact with each other. This so-called spin-orbit interaction (SOI) can significantly impact the magnetotransport in a 2DES. Basis of this SOI framework is an electron moving with velocity $\mathbf{v}$ in the electric field $\mathbf{E} = -\nabla V(r)$ of a crystal lattice, resulting from its Coulomb potential $V(r)$. In the rest frame of the electron, a relativistic Lorentz transformation translates this motion into an effective magnetic field $\mathbf{B}'$ experienced by the electron [30, 37]. The prime denotes the quantities in the electron rest frame. Note, that no external magnetic field is applied. This effective magnetic field is then in first approximation given by

$$\mathbf{B}' = -\frac{1}{c^2}\mathbf{v} \times \mathbf{E}, \tag{2.35}$$

where c denotes the velocity of light in vacuum. $\mathbf{B}'$ couples to the magnetic dipole moment of the electron, i.e. the spin via the Zeeman interaction. Within this description, a resulting Pauli spin-orbit correction term $\mathcal{H}_{SO}$ to the Hamiltonian of the system, in the nonrelativistic limit of the relativistic Dirac equation, can be written as

$$\mathcal{H}_{SO} = -\frac{\hbar}{4m_e^2c^2}\boldsymbol{\sigma} \cdot (\mathbf{p} \times \nabla V(r)) . \tag{2.36}$$

$\boldsymbol{\sigma} = (\sigma_x, \sigma_y, \sigma_z)$ is the vector of the Pauli spin matrices and $\mathbf{p}$ is the momentum operator. From this correction term follows a very general conclusion, that the strength of SOI is given by the gradient of the potential from the crystal lattice. As a consequence, elements in the crystal lattice with a higher nuclear charge enhance the SOI. For example in intrinsic silicon, SOI is weak compared to a stronger SOI in germanium or gallium. Indium and especially In-based alloys like InAs or InSb offer strong SOI. An important manifestation of the SOI is the effect of the so-called spin-orbit split-off band. This denotes an energetically lowered branch of the valence band due to the SOI.

2.3.1. Dresselhaus SOI

In general, semiconductors offer a spin degeneracy due to both, time and space inversion symmetry. By breaking the space inversion symmetry (either by the crystal lattice structure of the specific material or an intentionally created asymmetric potential), this spin degeneracy is lifted (although no external magnetic field is applied). The materials used in this thesis are without exception III/V-based alloys, for which the crystal structure is a face-centered-cubic (fcc) lattice with a diatomic basis - the so-called zinc blende structure. This lattice has no inversion symmetry center, thus creating a microscopic electric field contributing to the SOI. This contribution is denoted as the bulk inversion asymmetry (BIA), described by Dresselhaus [7]. For a 2DEG in a QW confined in the growth direction z, the resulting Hamiltonian for a Dresselhaus-type SOI is given by

$$\mathcal{H}_D^{2D} = \gamma_D \left[\sigma_x k_x \left(k_y^2 - \left\langle k_z^2 \right\rangle\right) + \sigma_y k_y \left(\left\langle k_z^2 \right\rangle - k_x^2\right)\right], \tag{2.37}$$

with the expectation value $\langle k_z^2 \rangle$ and the so-called cubic Dresselhaus parameter γ_D (cubic as it contains $\mathbf{k}^3$ contributions [7, 42]). Due to the z-confinement in the QW, we can assume $\langle k_z^2 \rangle \gg k_x^2, k_y^2$, with which Eq. 2.37 can be approximated by a linearized form

$$\mathcal{H}_D^{2D} = \beta_D \left(\sigma_x k_x - \sigma_y k_y\right), \tag{2.38}$$

[43, 44] with the linearized Dresselhaus parameter $\beta_D = -\gamma_D \langle k_z^2 \rangle \propto (\frac{\pi}{d_{QW}})^2$ [12, 42]. This parameter is given by the bandstructure of the system and the thickness of the QW d_{QW}. Practically, for a given system, the Dresselhaus SOI can (only) be tuned by d_{QW}.

2.3.2. Bychkov-Rashba SOI

Due to the confinement in z direction in a QW, a second contribution to the SOI has to be considered. This one is denoted as structure inversion asymmetry (SIA) and was first described by Bychkov and Rashba [8, 45], often only referred to as Rashba SOI. This contribution can be traced back to built-in electric fields, originating from the crystal lattice itself as well as from the specific bandstructure profile, including band edge discontinuities within the system. External electric fields (typically from gate electrodes parallel to the 2DES plane) can also modify this contribution to the SOI. Contrary to the cubic contribution of $\mathbf{k}$ in the Dresselhaus SOI, the Hamiltonian for Rashba SOI in a 2DES $\mathcal{H}_R^{2D}$ is linear in $\mathbf{k}$ and is given by

$$\mathcal{H}_R^{2D} = \frac{\alpha}{\hbar} (\boldsymbol{\sigma} \times \mathbf{p}) \cdot \hat{\mathbf{e}}_z = \alpha (\sigma_x k_y - \sigma_y k_x), \tag{2.39}$$

with the so-called Rashba parameter α. The dispersion relation is then characterized by two spin-split branches (characterized by + and −) and is given by

$$E(\mathbf{k}_{||}) = \frac{\hbar^2 \mathbf{k}_{||}}{2m_e^*} \pm \alpha \mathbf{k}_{||} = \frac{\hbar}{2m_e^*} \left(\mathbf{k}_{||} \pm \Delta k_R\right)^2 - \Delta E_R, \tag{2.40}$$

with the energetic difference ΔE_R at $\mathbf{k}_{||} = (0, 0)$ and the wave vector difference Δk_R [44]. The dispersion relation is depicted in Fig. 2.1, where the arrows indicate the spin orientation of the spin-split branches. Indicated in red are the energetic difference ΔE_R and the wave vector difference Δk_R. Both characteristic quantities can be calculated by the relation

$$\Delta E_R = \frac{1}{2} \alpha \Delta k_R \tag{2.41}$$

[46–48]. With a constant wave vector $k = k_F = \sqrt{2\pi n_s}$ in a 2DES with the electron sheet density n_s, the energy can be calculated by

$$\Delta E_R = \alpha \cdot \sqrt{\frac{\pi n_s}{2}}, \tag{2.42}$$

while for constant energy $E = E_F$, the wave vector difference is given by

$$\Delta k_R = \alpha \frac{2m_e^*}{\hbar^2}. \tag{2.43}$$

Combining both contributions to the SOI, Dresselhaus (BIA) and Rashba (SIA), yields a total contribution to the Hamiltonian of the SOI given as

$$\mathcal{H}_{SOI}^{2D} = \alpha (\sigma_x k_y - \sigma_y k_x) + \beta_D (\sigma_x k_x - \sigma_y k_y). \tag{2.44}$$

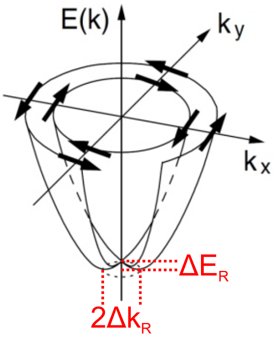

Fig. 2.1: *Dispersion relation of electrons in a 2DES with Rashba SOI lifting the spin-degeneracy. As a result, two spin-split branches occur where the arrows indicate the spin orientation. The energetic difference* ΔE_R *and the wave vector difference* Δk_R *of the spin-split branches are marked in red. Adapted from [37].*

Based on reports in the literature, the strength of each contribution (i.e. the value of their parameters β_D and α) varies strongly depending on the material system. Lommer *et al.* [49] have reported, that generally SIA dominates over the BIA for small bandgap semiconductors such as InAs or InSb. For large bandgap materials like GaAs, it is often the other way round. Similarly, a negligible BIA was found for InAs heterostructures by Luo *et al.* [50] and for $\mathrm{In}_{0.77}\mathrm{Ga}_{0.23}\mathrm{As/InP}$ heterostructures by Schäpers *et al.* [51]. Interestingly, while Winkler [37] pointed out that SIA and BIA yield comparable contributions in $\mathrm{In}_{0.53}\mathrm{Ga}_{0.47}\mathrm{As}$-based heterostructures, Faniel *et al.* [52] reported a dominating SIA contribution compared to BIA in such a $\mathrm{In}_{0.53}\mathrm{Ga}_{0.47}\mathrm{As}$-based QW. In this thesis, we investigate the SOI in 2DESs in InAs/InGaAs/InAlAs-based heterostructures with an indium concentration of 75%. From the reports in the literature we thus summarize, that we can expect a clearly dominating SIA contribution (Rashba-type) over the BIA contribution (Dresselhaus-type) in our heterostructures. As a consequence, we neglect the BIA contribution in our experiments and assign the SOI in our systems to the SIA contribution, characterized by the Rashba parameter α.

In the framework of the envelope function theory, Schäpers *et al.* [51] gave an expression for the Rashba parameter α based on a 2DES in a heterostructure comparable to the systems we use in this thesis. The QW consists of two different materials $M,1$ and $M,2$ where $M,1$ is the material with the smaller bandgap, embedded in material $M,2$ with the higher bandgap. The expression is then given by

$$\alpha = \frac{\hbar^2 E_P}{6m_e}\Big[\langle\Psi(z)|\, A_{el_{M,1}}\cdot(1-\Theta)\cdot\phi'(z)\,|\Psi(z)\rangle + \langle\Psi(z)|\, A_{el_{M,2}}\cdot\Theta\cdot\phi'(z)\,|\Psi(z)\rangle \\ +\frac{1}{2}\sum_n S_n\cdot A_{int}\cdot|\Psi(z_n)|^2\Big]. \tag{2.45}$$

E_P denotes the $\mathbf{k}\cdot\mathbf{p}-$ interaction parameter between conduction and valence bands, m_e is the invariant electron mass. The electron wavefunction of the first subband in the 2DES is given by $\Psi(z)$, for which z is the inverse growth direction (i.e. from the heterostructure surface $z=0$ towards the substrate $z>0$). The first two terms in Eq. 2.45 are denoted as the electrical contribution α_{el}, for which Θ is given by 0 within the QW (i.e. in material $M,1$) while it is 1 in the barriers of the QW (i.e. in material $M,2$). The second term originates from the finite energetical depth of the QW, thus allowing a non-vanishing part of the wavefunction within the barriers of the QW. The electric field within the structure is given by the derivative $-\phi'(z)$ of the confinement potential $\phi(z)$ creating the QW. The prefactor $A_{el_{M,j}}$ is given by

$$A_{el_{M,j}} = \frac{1}{\left(E_F - E_{\Gamma_7}^{M,j}\right)^2} - \frac{1}{\left(E_F - E_{\Gamma_8}^{M,j}\right)^2}, \tag{2.46}$$

with the Fermi energy E_F. $E_{\Gamma_i}^{M,j}$ denotes the energy in material M, j at the Γ-point of the degenerate heavy hole (HH)/light hole (LH) band Γ_8 and the split-off (SO) band Γ_7. The third (and thus last) term in Eq. 2.45 is denoted as the interface contribution α_{int}, where each interface n at z_n (i.e. a heterojunction of the two materials $M, 1$ and $M, 2$) is considered and added up separately. S_n is given by ± 1 depending on the order of the materials M, j with respect to z. The prefactor A_{int} is given by

$$A_{int} = \frac{\Delta E_{\Gamma_7}}{\left(E_F - E_{\Gamma_7}^{M,1}\right)^2} + \frac{\Delta E_{\Gamma_7}}{\left(E_F - E_{\Gamma_7}^{M,2}\right)^2} - \frac{\Delta E_{\Gamma_8}}{\left(E_F - E_{\Gamma_8}^{M,1}\right)^2} - \frac{\Delta E_{\Gamma_8}}{\left(E_F - E_{\Gamma_8}^{M,2}\right)^2}, \tag{2.47}$$

where ΔE_{Γ_i} describes the offset of the HH/LH band the SO band respectively at each interface n. As a conclusion of this expression, we split the Rashba parameter $\alpha = \alpha_{el} + \alpha_{int}$ into an electrical contribution α_{el}, which considers the electrostatic configuration within the QW with regard to the wavefunction, and the interface contribution α_{int}, which considers the overlap of the wavefunction with the interfaces within the QW.

2.3.3. Magnetotransport with SOI

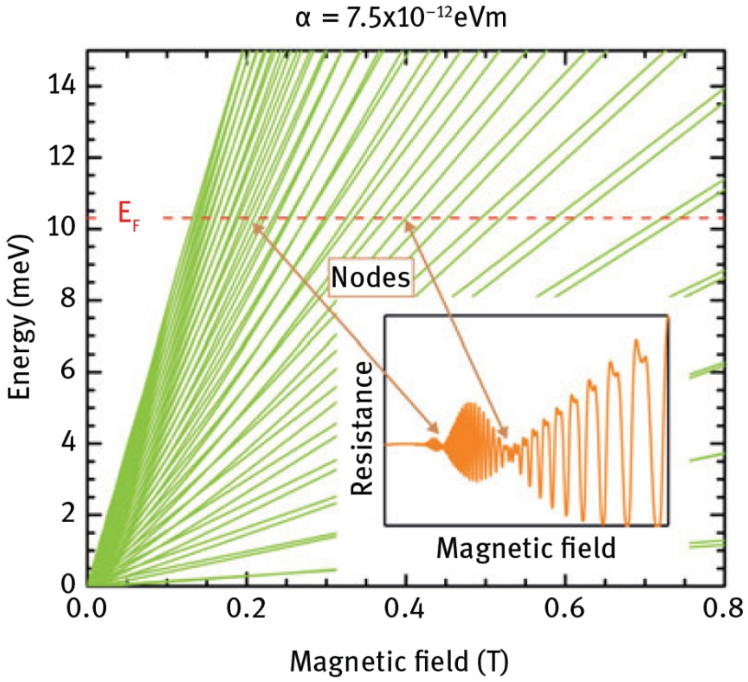

Fig. 2.2: *Energy spectrum of the LLs for a given 2DES with Rashba SOI. The Landau fan is modified due to the SOI and the energetic spacing of LLs is irregular. As a result, E_F and thus the magnetoresistivity exhibit a beating pattern in their oscillatory behavior. [44]*

The strength of the Rashba parameter can be experimentally determined by means of magnetotransport measurements, for which we denote the extracted Rashba parameter as α_{exp}. We exploit the occurrence of a beating pattern in the SdH oscillations due to the SOI. This beating pattern originates from the Landau quantization in combination with the spin-split branches in the dispersion relation of a 2DES with SOI. The external magnetic field, applied in z direction perpendicular to the $xy-$plane, modifies the Rashba-Hamiltonian in Eq. 2.39 via

$$\mathcal{H}_R^{2D} = \frac{\alpha}{\hbar} \left(\boldsymbol{\sigma} \times (\mathbf{p} + e\mathbf{A}) \right) \cdot \hat{\mathbf{e}}_z, \tag{2.48}$$

with the vector potential $\mathbf{A}$ written in Landau gauge as $\mathbf{A} = (0, Bx, 0)$. As a consequence, the quantized energy state of the $n-$th LL is split into two states with regard to the spin-split branches in the dispersion relation (see. Eq. 2.40). The energy of the $n-$th LL is then given by

$$E_{n,\pm} = \hbar\omega_c \left(n \pm \sqrt{\left(\frac{1}{2} - \frac{g^* m_e^*}{2m_e} \right)^2 + \frac{2\alpha m_e^*}{\hbar^3 \omega_c} n} \right). \tag{2.49}$$

This energy spectrum in Eq. 2.49 is visualized in Fig. 2.2 for a given 2DES with Rashba SOI (here α was set to 7.5×10^{-12} eVm). We observe irregular energetic spacing of LLs (green) with an increasing magnetic field. As a consequence, the oscillatory behavior of E_F (orange dotted) and thus from the magnetoresistivity (inset) is modified to a beating pattern including the occurrence of nodes. Equivalently, the beating pattern can be explained due to a slightly different electron population up to the Fermi energy of the two spin-split branches, denoted as + and − in the dispersion relation in Eq. 2.40. As a result, the 2DES inherits two slightly different electron densities n_+ and n_-, characteristic for the two spin-split branches. Both add up to the spin-degenerate electron sheet density n_s. As the SdH frequency is constant for a given density in $1/B$, the now two present frequencies are in superposition and result in the characteristic beating pattern. This is characterized by an average sum and difference frequency, visible as the carrier and the envelope frequency respectively of the beating pattern. The two individual densities n_+ and n_- can then be extracted via FFT (a detailed description of this extraction process is presented in Sec. 3.3) with which the Rashba parameter α_{exp} can be determined as follows [50, 51, 53]:

$$\alpha_{exp} = \frac{n_+ - n_-}{\sqrt{n_-}} \cdot \frac{\sqrt{\pi}\hbar^2}{2m_e^*}. \tag{2.50}$$

2.3.4. Quantum interference correction: weak anti-localization

In the description of the WL in Sec. 2.1.4, SOI was not taken into account. With SOI, the spin of an electron is strongly coupled to its direction of motion. Considering multiple scattering events, the electron changes its trajectory multiple times and thus, the spin also changes its direction with each scattering event. We assign the initial states by a certain spin state $|s\rangle$ on the Bloch sphere. Performing one loop in clockwise direction, the spin changes its direction multiple times and the final state after the loop is given by

$$|s'\rangle = \mathcal{R} \, |s\rangle\,, \tag{2.51}$$

where $\mathcal{R}$ is the rotation operator, representing the multiple spin orientation changes during the loop. When we consider a time-reversed path, i.e. an anti-clockwise loop, the spin rotation is reversed, represented by $\tilde{\mathcal{R}} = \mathcal{R}^{-1}$. The final state of this anti-clockwise loop is then given by

$$|s''\rangle = \tilde{\mathcal{R}} \, |s\rangle \, . \tag{2.52}$$

The return probability P_s with consideration of the spin state is then given by

$$P_s = \left(\langle s'| + \langle s''|\right)\left(|s'\rangle + |s''\rangle\right) = 2 + \langle s'|s''\rangle + \langle s''|s'\rangle \, . \tag{2.53}$$

Similar to the description for the WL, the first term with value 2 in Eq. 2.53 represents the classical return probability P_{cl}, while the last two terms represent the interference correction. These correction terms are then given by

$$\langle s''|s'\rangle = \langle s| \, \mathcal{R}^2 \, |s\rangle \, . \tag{2.54}$$

For a situation with no SOI, $\mathcal{R}$ is in good approximation given by the unity matrix. As a consequence, the two correction terms in Eq. 2.53 each yield 1, resulting in a total return probability P_s identical to P_{qm} (equals 4), thus representing WL. However when (strong) SOI is taken into account, the correction terms yield $-1/2$ each [54], with which the total return probability P_s is given by

$$P_s = 2 - \frac{1}{2} - \frac{1}{2} = 1. \tag{2.55}$$

This translates into a degraded backscattering probability compared to the classical probability P_{cl}, denoted as weak anti-localization (WAL). This manifests in the experiment as a decrease of ρ_{xx} at zero magnetic field. By an increase of the magnetic field, the Aharonov-Bohm phase destroys the WAL correction and the initial resistivity is restored. [30]

3. Experimental methods

In this chapter we present details on the experimental methods utilized during the course of this thesis. We give an insight into heterostructure growth via molecular beam epitaxy and illustrate the electrical characterization of our samples in low-temperature magnetotransport setups.

3.1. Molecular beam epitaxy

Via molecular beam epitaxy (MBE), we are able to create high quality semiconductor heterostructures. Epitaxy consists of two ancient Greek words and can be translated into 'arranging' or 'ordering'. This expresses exactly the MBE process of growing additional crystal layers on an already (perfect) crystalline substrate. Requirements for this epitaxial crystal growth are a pressure in the ultra high vacuum (UHV) regime with pressures of 10^{-11} mbar and a (mono)crystalline substrate with a lattice constant matched to the to-be-deposited additional layers. The substrate is heated while atoms, molecules or clusters of different elements are evaporated from effusion cells. Due to the UHV, scattering with residual gas particles is completely suppressed: the atoms, molecules or clusters form a beam, hence the name. When the beam hits the heated substrate surface, the evaporated particles stick to the surface and diffuse on the surface until they find the energetically most favorable site in the crystal lattice. Lattice-mismatch results in a build-up of strain in the growing crystal which eventually relaxes into crystalline defects (or in a worst case destroying the mono-crystalline lattice). In the right regime (e.g. temperature and beam flux), growth occurs in a layer by layer mode which allows to produce sharp interfaces with atomic monolayer (ML) precision between different materials. Heterostructures can be produced by employing appropriate shutter sequences for each element, exploiting also the characteristics of different alloys, e.g. matched lattice constant for gallium arsenide (GaAs) and aluminum gallium arsenide ($\mathrm{Al}_x\mathrm{Ga}_{1-x}\mathrm{As}$).

The heterostructures used in this thesis are grown in a modified Veeco Gen II chamber equipped for group III/V semiconductor heterostructures. The base pressure reaches $< 4.0 \times 10^{-11}$ mbar, pumped with a cryogenic pump. Group III elements are gallium (Ga), aluminum (Al) and indium (In), evaporated from the liquid state within pyrolitic boron nitride (pBN) crucibles in Knudsen-type effusion cells. Group V elements are arsenic (As) and antimony (Sb), both sublimated in valved cracker cells. Doping materials are carbon (C) and silicon (Si) in filament cells and manganese (Mn) in a sublimation effusion cell. Pneumatically operated shutters for each cell allow all material combinations while preventing cross contamination. We monitor the beam equivalent pressure (and thus also the flux ratios) with a beam flux ionization gauge. We regulate the growth rate with the beam flux of the group III elements (via the cell temperature) while the group V element is typically provided in abundance. The substrate temperature is monitored via a pyrometer and an analysis of the temperature dependent optical absorption edge. The chamber is also equipped with a reflection high-energy electron diffraction (RHEED) system which allows in-situ crystal analysis as well as monitoring of the growth rate of several materials via RHEED oscillations.

3.1.1. RHEED oscillations

One way to monitor the crystal growth in-situ ML by ML is through intensity analysis of the RHEED beam reflected from the surface of the substrate. Electrons are accelerated with high voltage (typically 15 kV) from the RHEED gun onto the substrate surface in a grazing angle, from which they are diffracted by arrangements of atoms on the surface and then impinge on a fluorescent detector screen on the opposite site. In an appropriate setup of the incidence angle and crystal direction, the de-Broglie wavelength of the accelerated electrons and the diffraction patterns allow to analyze the crystalline structure and the surface reconstruction of the substrate. A different setup allows to monitor the growth rate: On a smooth surface, typically when a ML is complete, the electron beam experiences minimal scattering and the reflected beam appears as a bright spot with high intensity on the fluorescent screen. Continuing the growth, more atoms adsorb on the surface, increasing the disorder on the surface and the scattering of the beam. As a consequence, the intensity of the reflected beam is decreased. When half a ML is grown, disorder on the surface and thus scattering of the beam is maximized. At this point, the intensity on the screen is minimal. With ongoing growth, disorder decreases to a minimum when the ML is completely closed. At the same time, the intensity on the screen increases, thus performing one oscillation during the growth of one ML, denoted as a RHEED oscillation. Knowing the thickness of a ML of the grown material, we can calculate the growth rate by measuring the time between two maxima or minima of the RHEED oscillations. In order to minimize the error margin, we aim to obtain multiple oscillations and take the mean of the ML duration. The oscillations will eventually dampen out, as the second ML starts already on wide islands before the first ML is completed. As this process continues successively, the system is moving towards an equilibrium surface roughness. As a consequence, scattering of the electron beam is maximized and oscillations are no longer visible. Annealing the substrate with reduced group V flux increases the surface mobility of adsorbed atoms and hence allows to decrease the roughness, thus opening up an oscillation window again.

Lattice-matched growth is mandatory for this calibration method as the surface roughness has to be kept minimal. The calibration of Ga or Al is thus straightforward as the lattice constant does not change for $\mathrm{Al}_x\mathrm{Ga}_{1-x}\mathrm{As}$ or $\mathrm{Al}_x\mathrm{Ga}_{1-x}\mathrm{Sb}$. However, the introduction of indium complicates the situation for a given substrate like e.g. GaAs, as the lattice constant increases with the indium concentration in $\mathrm{In}_x(\mathrm{Al,Ga})_{1-x}\mathrm{As}$ alloys.

3.1.2. Growth of In-based alloys

This section shortly motivates and illustrates the material choice and the applied growth parameters for the InAlAs-based structures presented in this thesis. A detailed layout description of the active layers is given in Ch. 4 to 7. All of the heterostructures presented over the course of this thesis are based on $\mathrm{In}_x\mathrm{Al}_{1-x}\mathrm{As}/\mathrm{In}_x\mathrm{Ga}_{1-x}\mathrm{As}/\mathrm{InAs}$ with $0.65 \geq x \geq 0.81$. This material system provides high intrinsic SOI, making it favorable for spin-orbitronic applications [37]. MBE growth of heterostructures with these alloys allows us to flexibly custom-tailor their bandstructure and thus actively influence the SOI. Although this material system generally lacks a lattice-matched substrate, several efforts over the last couple decades were made to create 2DESs with high electron mobility [23, 24, 26, 55–58]. As the InAlAs contains intrinsic crystal defects, which act as donors, an electron population in InAlAs-based QWs can be achieved without intentional doping [57]. All the heterostructures presented in this thesis were grown on a semi-insulating GaAs (100) substrate. The lattice mismatch of 7.2% between InAs and GaAs prevents epitaxial growth of high-indium-concentration layers directly onto the GaAs substrate. In order to overcome this lattice mismatch, a buffer layer is implemented in which the lattice constant is successively increased up to the aspired final concentration. This is done by successively increasing the indium concentration in $\mathrm{In}_x\mathrm{Al}_{1-x}\mathrm{As}$ layers. Sophisticated buffer designs were developed [23, 24, 26, 55, 56, 58–62] in which the strain-induced crystalline defects are confined in the buffer layers and thus providing a defect-free so-called virtual substrate (VS). This 'new' substrate (above the actual GaAs substrate) is characterized by the same lattice constant as the to-be-grown active layers and thus ensures their epitaxial growth. The key is to minimize (or ideally prevent) the amount of threading dislocations, which occur from the strain relaxation, penetrating through the buffer and the VS into the active layers. There they would significantly degrade the quality of the 2DES. Here, we follow the epitaxial growth study of Capotondi *et al.* [58], suggesting a step-wise increase of the indium concentration in $\mathrm{In}_x\mathrm{Al}_{1-x}\mathrm{As}$ layers. This for one ensures a build-up of strain at the start of each layer while also confining emerging dislocations within these layers (or guiding them towards the side of the heterostructure). The buffer is thus denoted as a step-graded buffer. We also employ a compositional overshoot of the Indium concentration above the aspired target concentration as it benefits the adaption of the lattice constant (and thus the quality of the active layers) by reducing residual compressive strain [58]. A detailed description of the step-graded buffer used in the heterostructures presented in this thesis is given within the discussion of each heterostructure and in App. C.

The growth process is initiated with a deoxidization of the GaAs substrate at a substrate temperature of $\approx 620°\mathrm{C}$ under As_4 beam equivalent pressure of 7×10^{-6} Torr. Subsequently 100 nm GaAs and fifteen periods which alternate 10 nm GaAs and pause layers are grown to smoothen the substrate. This also screens the following buffer from impurities at the substrate surface. The substrate temperature is then lowered to 335°C during a growth pause. With this reduced temperature, the $\mathrm{In}_x\mathrm{Al}_{1-x}\mathrm{As}$ step-graded buffer, as mentioned before, is grown. After the overshoot, a so-called recovery to the target concentration is grown, typically with a thickness of 110 nm. This is followed by the VS, typically a 120 nm $\mathrm{In}_x\mathrm{Al}_{1-x}\mathrm{As}$ constant composition layer. At the same time, during the growth of the VS, the substrate temperature is increased to 450°. Subsequently follows the QW structure embedded typically in $\mathrm{In}_x\mathrm{Al}_{1-x}\mathrm{As}$ barriers. Together with the VS, this is denoted as the active layers. Every heterostructure presented in this thesis is capped with 2 nm of $\mathrm{In}_x\mathrm{Ga}_{1-x}\mathrm{As}$ (with the indium concentration matching the underlying InAlAs barrier) in order to prevent oxidation damage of the underlying Al-containing layer.

3.2. Post-growth crystal characterization

After the MBE growth, several techniques for the characterization of the heterostructure and the crystalline structure were used. This section shortly presents three (commercially available) methods employed over the course of this thesis.

3.2.1. Transmission electron microscopy (TEM)

In transmission electron microscopy (TEM), the crystalline structure is imaged by electrons transmitted through a thinned cross-sectional specimen of the material. Electrons are accelerated by a high voltage (typically $100 - 300$ kV) and impinge on the specimen, where they are diffracted. After a series of electromagnetic lenses and plates, the transmitted electrons are visualized on a detector. Due to the small de-Broglie wavelength of the imaging electrons, resolution in the sub-Å range is achieved. This allows to image single atom columns as well as crystalline defects and even atomically sharp interfaces between different materials. We use this technique for one to visualize the occurrence of crystalline defects in our heterostructures, as depicted in Fig. C.1. For another, we exploit the contrast of different materials in order to measure the thickness of specific layers within the heterostructure in order to deduce the growth rate, as presented in Ch. 4.

3.2.2. Secondary ion mass spectrometry (SIMS)

The secondary ion mass spectrometry (SIMS) is a technique to analyze the elemental composition in a heterostructure sample. The sample surface is sputtered in a high vacuum chamber with a focused primary ion beam, thus ejecting atoms from the surface from which a fraction is ionized. These secondary ions are then analyzed with mass spectroscopy. Simultaneously, a reference sample with the same elements and ideally the same composition is processed. This allows to quantify the elemental composition of the sample. We use this technique over the course of this thesis as a way to calibrate the indium growth rate (see Ch. 4). SIMS data of our heterostructures presented in this thesis is provided by Probion Analysis. In these SIMS analysis runs, Cs^+ were the primary ions with an impact energy of 2 keV. Indium, gallium and aluminum were quantified in an area with 60 μm diameter by means of reference samples with $Al_{0.52}Ga_{0.48}As$, $In_{0.54}Ga_{0.46}As$ and $In_{0.54}Al_{0.46}As$.

3.2.3. Energy-dispersive X-ray spectroscopy (EDX)

A different approach to analyze the elemental composition of a heterostructure sample is via energy-dispersive X-ray spectroscopy (EDX). The sample is in focus of an electron beam, from which an electron excites an electron in an inner shell of the atom. In order to minimize the energy, the place of the excited electron in the inner shell is filled with an electron from an energetically higher (outer) shell. This transition emits a photon in the X-ray regime. The number and the energy of the emitted photons is then analyzed by an energy-dispersive spectrometer. As these parameters of the emission is characteristic for each atom, the elemental composition of the analyzed area can be determined. Typically EDX is combined with STEM as this allows to add the spatial resolution of the STEM to the EDX. We utilize this technique in order to calibrate the growth rate of our indium cell. EDX data of our heterostructures presented in this thesis is provided by Probion Analysis.

3.3. Magnetotransport

After the MBE growth of our heterostructures, we characterize and investigate them electrically via magnetotransport (MT). This section shortly presents the applied measurement design of the samples as well as the low-temperature measurement setup. We finish this section with a detailed description on how we extract the Rashba parameter α_{exp} from SOI-induced beating patterns in ρ_{xx} (see Sec. 2.3.3) via FFT analysis.

3.3.1. Measurement setup

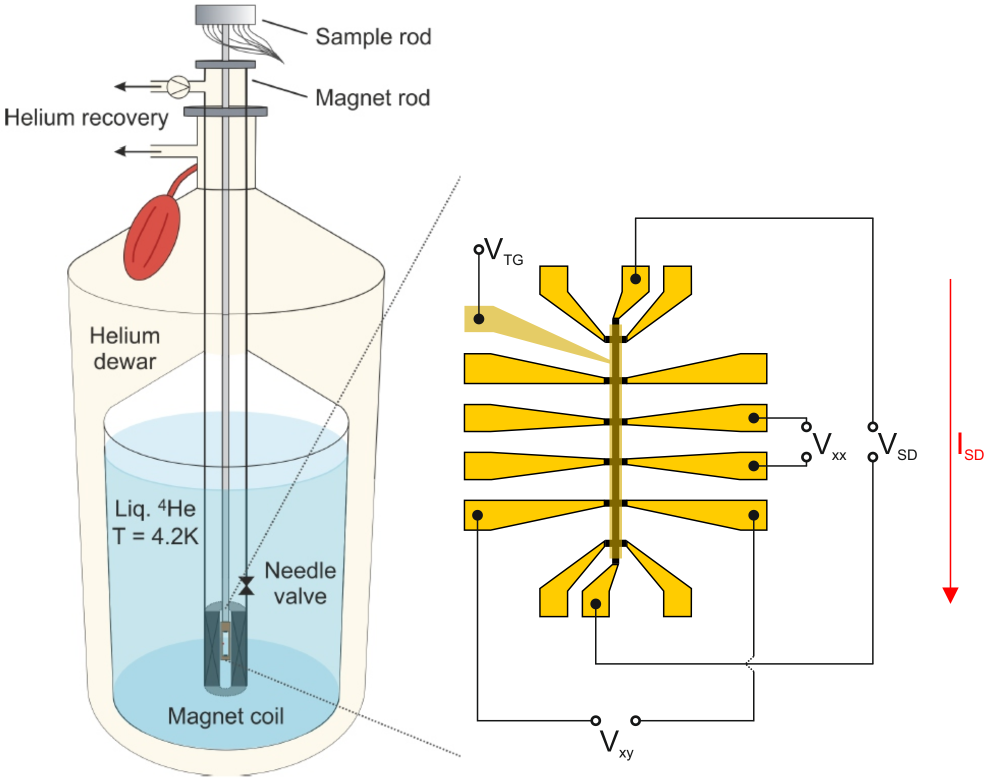

Fig. 3.1: *Schematic illustration of the low-temperature measurement setup with the Hall bar measurement geometry of the samples. The sample is submerged in the liquid* ^{4}*He, for which the temperature can be decreased down to* $T = 1.4$ *K exploiting the vapor pressure. The magnet coil allows to apply a magnetic field up to* 6 *T perpendicular to the sample. Adapted from [63].*

We use the Hall bar (HB) geometry as the sample design for our MT measurements. The HB structure, depicted in Fig. 3.1, is lithographically defined. The corresponding fabrication details are presented in the appendix in App. D. The HB channel has a width of $W = 20$ μm and each segment has a length of $L = 300$ μm. Contact pads are realized by AuGe (88%/12%) and Ni. Along the channel, we apply a source drain (SD) voltage V_{SD} resulting in a SD current I_{SD} as indicated in red in Fig. 3.1. Longitudinal voltage V_{xx} and transversal voltage V_{xy}, also denoted as Hall voltage, are obtained according to Fig. 3.1.

We determine the longitudinal and transversal resistivity ρ_{xx} and ρ_{xy} respectively via

$$\rho_{xx} = \frac{V_{xx}}{I_{SD}} \cdot \frac{W}{L}, \tag{3.1}$$

$$\rho_{xy} = \frac{V_{xy}}{I_{SD}}. \tag{3.2}$$

By applying a magnetic field **B** perpendicular to the sample, we obtain the characteristics of the 2DES, the electron sheet density n and the electron mobility μ according to Eq. 2.14 (Hall slope) and 2.15 respectively. We also determine the electron sheet density via SdH-oscillations (see Eq. 2.20), which is always in good agreement with the values determined via the Hall slope. When we refer to a electron density n over the course of the thesis, it is always the one determined from the Hall slope if not otherwise stated. In time-resolved measurements of the electron sheet density as a function of the gate voltage, we determine the density by applying a constant magnetic field of 500 mT while we sweep the gate voltage at rates of $1 - 5$ mV/s.

The MT measurements are performed using standard low-frequency lock-in techniques at 17 Hz. The SD current I_{SD} is set constant to 50 nA with a 100 MΩ pre-resistor.

The samples presented in this thesis are equipped with a global Ti/Au topgate (TG) above the HB channel (transparent gold in Fig. 3.1), separated by a dielectric from the semiconductor heterostructure. Specific samples also are equipped with a backgate (BG) electrode via a n-type doped substrate. According to the field effect (see Sec. 2.2) we can tune the electron sheet density by varying the specific gate voltage, V_{TG} and/or V_{BG}. A detailed description of the gates and their fabrication is given in App. D.

If not otherwise stated, the MT experiments regarding the electron density were performed at $T = 4.2$ K, whereas evaluation of beating patterns and extraction of the Rashba parameter were performed at $T = 1.7$ K. These experiments were performed in a ^{4}He dewar, illustrated in Fig. 3.1. The sample sits in a liquid ^{4}He bath, for which the temperature can be decreased according to the vapor pressure of the ^{4}He by pumping on the bath. A magnetic field up to 6 T can be applied perpendicular to the sample.

3.3.2. Analysis of beating pattern

Over the course of this thesis, we observe beating patterns of the SdH oscillations in the longitudinal resistivity ρ_{xx}, which we assign to Rashba SOI (see Sec. 2.3.2 and 2.3.3). This section shortly describes the evaluation process, how we extract the Rashba parameter α_{exp} from the magnetotransport data. Exemplarily for a sample presented in Ch. 6, Fig. 3.2(a) displays ρ_{xx} as a function of the magnetic field B (black trace). Between $B = 0.5$ T and $B = 0.7$ T a clear beating pattern of SdH oscillations is visible. This is indicated by the increase and decrease of the amplitude, forming an envelope, which is followed for higher magnetic field by the opening of another envelope. This suggests two almost identical SdH frequencies, resulting in the beating pattern with an average sum (carrier frequency) and an average difference frequency (envelope), see Sec. 2.3.3. ρ_{xx} decreases, suggesting an underlying background which impacts the magnetotransport. For the majority of the samples analysed over the course of this thesis, we observe a background. However, the observed types of background are not consistent from sample to sample and even within one sample, the direction and type changes for different electron density regimes. The origin of these backgrounds is still under investigation in our group.

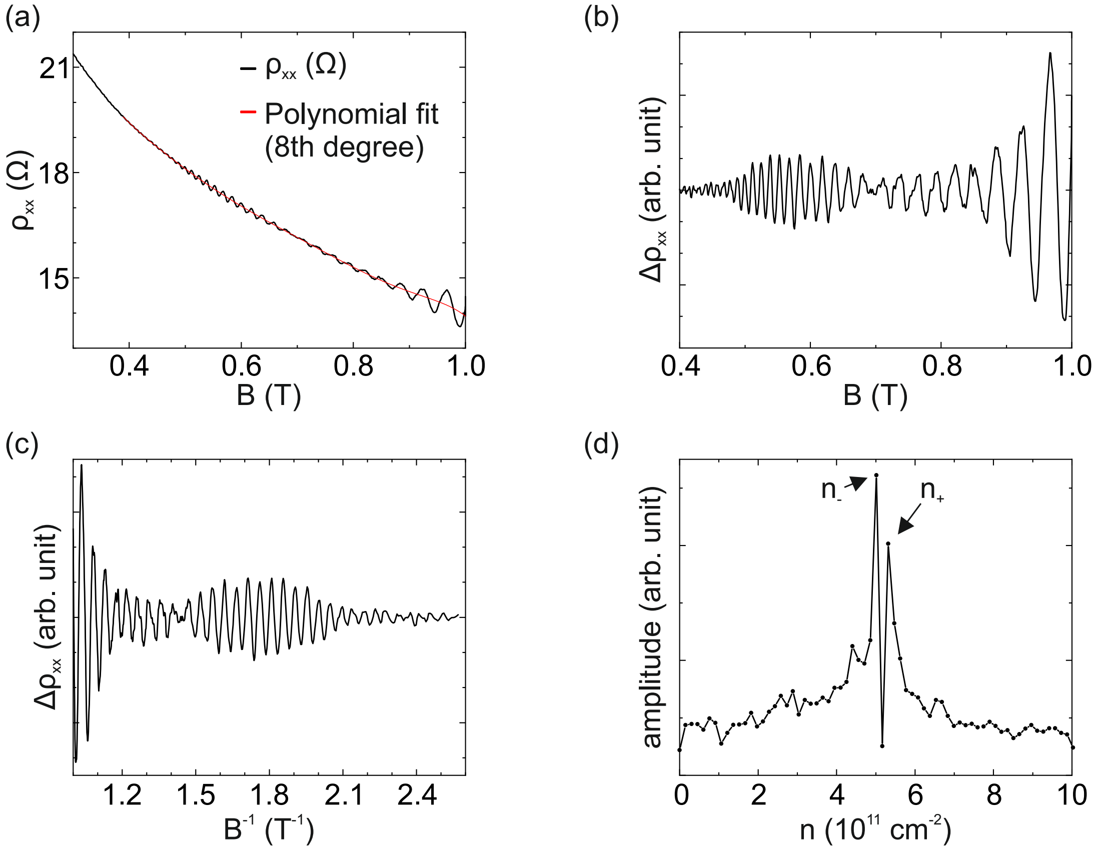

Fig. 3.2: *Data visualization of the FFT analysis. (a) Longitudinal resistivity* ρ_{xx} *(black) as a function the magnetic field* B *with occurring SOI-induced beating pattern. A polynomial fit of* 8*th degree (red) was applied to mimic the underlying background. (b) Residual longitudinal resistivity* $\Delta\rho_{xx}$ *after subtraction of the polynomial fit as a function of* B*. The beating pattern is significantly more pronounced due to the subtracted background. (c)* $\Delta\rho_{xx}$ *as a function of* $1/B$ *highlighting the SdH frequencies of the beating pattern. (d) FFT amplitude as a function of the electron density* n *exhibiting a pronounced double-peak structure. This indicates the lifted spin-degeneracy due to Rashba SOI. By extracting the two peak values of* n*, we calculate the Rashba parameter* α_{exp}*.*

In order to extract the pure beating signal from the ρ_{xx} data, we apply a polynomial fit to the underlying background. In Fig. 3.2(a), a polynomial fit of 8*th* degree was applied, indicated as the red trace. By subtracting this polynomial fit, we obtain the residual longitudinal resistivity $\Delta\rho_{xx}$, depicted as a function of B in Fig. 3.2(b). As a result, the beating pattern is significantly more pronounced. In order to extract the individual frequencies n_+ and n_-, which originate the beating pattern, we plot $\Delta\rho_{xx}$ as a function $1/B$ in Fig. 3.2(c), as the SdH oscillations are sinusodial over $1/B$ (see Sec. 2.1.3). Based on this dependence, we are able to perform a FFT analysis of this beating pattern, which yields a SdH frequency spectrum with the frequency f_{FFT}. Note, that we interpolate the $\Delta\rho_{xx}(B)$ data in order to ensure equally spaced data points. Also note, that we apply a rectangular window function for the FFT analysis. We did not observe enhancement by choosing different window functions. We calculate the electron density n from the SdH frequencies according to Eq. 2.20 in Sec. 2.1.3,

$$n = \frac{g_s \cdot e}{h} f_{FFT}, \tag{3.3}$$

with $g_s = 1$ because of the spin-splitting due to the SOI[1]. This spectrum, now as a function of n, is depicted in Fig. 3.2(d). As expected from the beating pattern, two density peaks $n_+ = 5.3 \times 10^{11}$ cm^{-2} and $n_- = 5.0 \times 10^{11}$ cm^{-2} appear closely together, separated only by $\Delta n = 0.3 \times 10^{11}$ cm^{-2}. According to Eq. 2.50,

$$\alpha_{exp} = \frac{n_+ - n_-}{\sqrt{n_-}} \cdot \frac{\sqrt{\pi}\hbar^2}{2m_e^*}. \tag{3.4}$$

we calculate the Rashba parameter α_{exp}, denoted with *exp* as it is the experimentally determined one[2]. For this presented configuration, this yields $\alpha_{exp} = 0.75 \times 10^{-11}$ eVm. Note that both frequencies n_+ and n_- add up to match exactly the electron sheet density determined via the Hall slope.

We assign the beating pattern to Rashba SOI. In our heterostructure we assume the Dresselhaus contribution to be negligible (see Sec. 2.3.2). We can exclude Zeeman splitting (see Sec. 2.1.3) as we perform the FFT analysis strictly for $B \leq |1|$ T and we observe SdH frequency modification due to Zeeman splitting in all of our samples only for $B > |2|$ T. We can also exclude the occupation of a second size-quantized subband in the QW and thus resulting MIS (see Sec. 2.1.3) originating a beating pattern because our bandstructure simulations suggest a second subband occupation for electron sheet densities $n > 9 \times 10^{11}\,$cm^{-2}. For the majority of samples we do not perform a beating pattern analysis in density regimes as high as this. However in the presented example in Fig. 3.2 we obtain $n = 10.3 \times 10^{11}$ cm^{-2}. We can still exclude MIS here due to two observations: First, we do not observe a third peak in the FFT spectra of any of the samples presented over the course in this thesis. This third peak would be indicative of MIS (see Sec. 2.1.3). Second, the population of the second subband would increase successively with increasing gate voltage, thus a density peak in the FFT spectrum would emerge from small densities and develop to higher densities with the increasing gate voltage. We do not observe this in any of the samples presented over the course of this thesis.

---

[1] As long as there is no beating pattern, a FFT analysis of the SdH oscillations yields one peak. The density is then calculated obeying $g_s = 2$ as the LLs are spin-degenerate (before the onset of Zeeman splitting).

[2] We use for the calculation of α_{exp} the effective mass $m_e^* = 0.0383 \cdot m_e$. We determined this in similarly designed heterostructures by temperature-dependent analysis of the SdH oscillation amplitude [64].

4. Control of the indium concentration

Over the course of this thesis, we custom-tailor the bandstructure by specifically choosing heterostructure layout designs including variation of the indium concentration. This requires a precise calibration of the indium growth rate, for which this chapter briefly covers several calibration techniques

4.1. Electron mobility for varying indium concentration

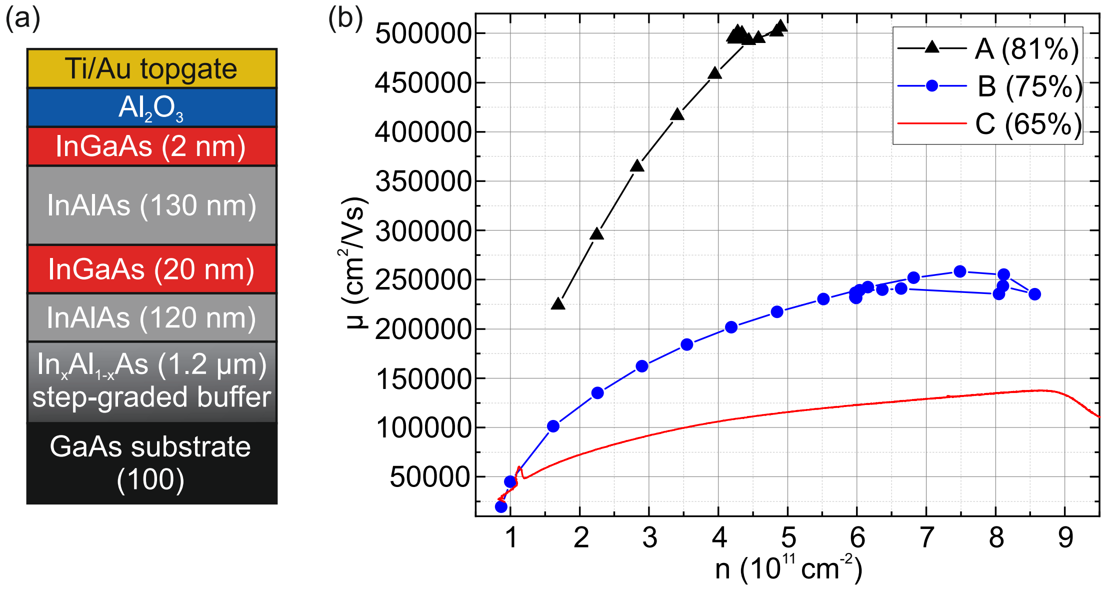

Fig. 4.1: *(a) Heterostructure layout of sample A, B and C, where the indium concentration in the active layers varies, i.e. 81% indium in sample A, 75% in sample B and 65% in sample C. (b) Electron mobility μ as a function of the electron density n at $T = 4.2$ K in samples A, B and C, representing different indium contents.*

We present an undoped heterostructure consisting of a 20 nm InGaAs QW embedded in 120 nm InAlAs below the QW (towards the substrate) and 130 nm InAlAs above the QW (towards the surface), capped by 2 nm InGaAs to prevent oxidation damage. The heterostructure layout is shown in Fig. 4.1(a). Three wafers with identical layer thicknesses were grown - only the indium concentration in the active layers was varied: 81% indium in sample A, 75% in sample B and 65% in sample C. Their In$_x$Al$_{1-x}$As step-graded buffer was designed as follows: $x = 0.1 - 0.87$ in 19 steps followed by a single step back to 0.81 in sample A, $x = 0.1 - 0.82$ in 17 steps followed by a single step back to 0.75 in sample B and $x = 0.1 - 0.75$ in 18 steps followed by a single step back to 0.65 in sample C (see also Sec. 3.1.2 and App. C). Fig. 4.1(b) summarizes the comparison of these three samples regarding their electron mobility μ as a function of the electron density n at $T = 4.2$ K. The maximum mobility $\mu = 506\,000$ cm^2/Vs at $n = 4.9 \times 10^{11}$ cm^2 was obtained for sample A (81% indium), followed by $\mu = 258\,000$ cm^2/Vs at $n = 7.5 \times 10^{11}$ cm^2 for sample B (75% indium) and $\mu = 137\,000$ cm^2/Vs at $n = 8.7 \times 10^{11}$ cm^2 for sample C (65% indium). Since a comparison of the maximum mobility is difficult as they are obtained for different densities, Fig. 4.1(b) depicts this strong deviation also for comparable densities in the range of $n = 2 - 5 \times 10^{11}$ cm^2. Note, a rather small difference of only 6% of the indium concentration between sample A and B results in a more than doubled mobility. This comparison shows that a small variation of the indium concentration in such heterostructures has a significant impact on the magnetotransport properties of the heterostructure. In a growth-based design study of such heterostructures, the ability to trace back differences to growth-related changes and not due to variations, e.g. of the indium concentration, hence a reliable growth rate calibration of the indium cell is a necessity.

4.2. Indium growth rate calibration

The indium cell in our III/V growth chamber is a Knudsen-type evaporation cell (see Sec. 3.1), featuring an exponential dependence of the growth rate as a function of the temperature. When accessing a large range from low to high rates, this cell type requests a large number of measurement points to map the exponential dependence with sufficient precision. The necessity to cover large ranges applies to all of the structures in this thesis: all heterostructures are grown on a GaAs substrate, for which a step-graded buffer is implemented to overcome the large lattice mismatch of the GaAs and the InAlAs-based active layers (see Sec. 3.1.2). Within the growth concept of this step-graded buffer, indium growth rates in the range of $0.1 - 4$ Å/s are required to achieve a indium concentration range of $x = 0.05 - 0.9$ in the $\mathrm{In}_x\mathrm{Al}_{1-x}\mathrm{As}$ buffer[3].

4.2.1. RHEED on GaAs

The most commonly used in-situ rate calibration method is the observation of monolayer (ML) growth via reflection high-energy electron diffraction (RHEED), see Sec. 3.1.1. For this, we use a GaAs (100) substrate. The lattice mismatch between pure InAs and GaAs requires the growth of $\mathrm{In}_x\mathrm{Al}_{1-x}\mathrm{As}$ on prior-grown AlAs while exploiting the ability to grow a certain thickness of the lattice-mismatched $\mathrm{In}_x\mathrm{Al}_{1-x}\mathrm{As}$ until the critical thickness is reached where the built-up strain relaxes as crystal defects, i.e. damaging the substrate. To increase the critical thickness the substrate temperature is lowered significantly (from 540°C to 450°C). The critical thickness depends on the indium concentration, where low indium concentration (smaller lattice mismatch) allows a higher critical thickness and vice versa, typically on the scale of a few nanometers (the ML thickness of $\mathrm{In}_x\mathrm{Al}_{1-x}\mathrm{As}$ is 2.83 – 3.02 Å). Adding to the limited growth thickness is the fact, that after each $\mathrm{In}_x\mathrm{Al}_{1-x}\mathrm{As}$ growth (while strain is built up), the strain has to be degraded again by growing a few tens of superlattice periods with AlGaAs/GaAs (for which one also has to wait to get the temperature up to 540°C again). Ideally, the strain is lowered to zero again in order to exploit the full critical thickness of another following $\mathrm{In}_x\mathrm{Al}_{1-x}\mathrm{As}$ layer. This can be quite time-consuming, especially when a 'full' calibration of the indium cell for a step-graded buffer is required.

We use a growth mode, were the growth rate is determined by the group III rate while offering As overpressure. By this, the growth rates of two group III materials (here In and

---

[3] with a constant aluminum rate typically at 0.6 Å/s

Al), simply add up. The Al rate can be determined quite easily, as it is lattice-matched to the GaAs substrate. Then, while the Al cell is still open, the indium cell is opened, resulting in an increased growth rate corresponding to both materials. A simple subtraction of the prior determined Al rate gives the indium rate.

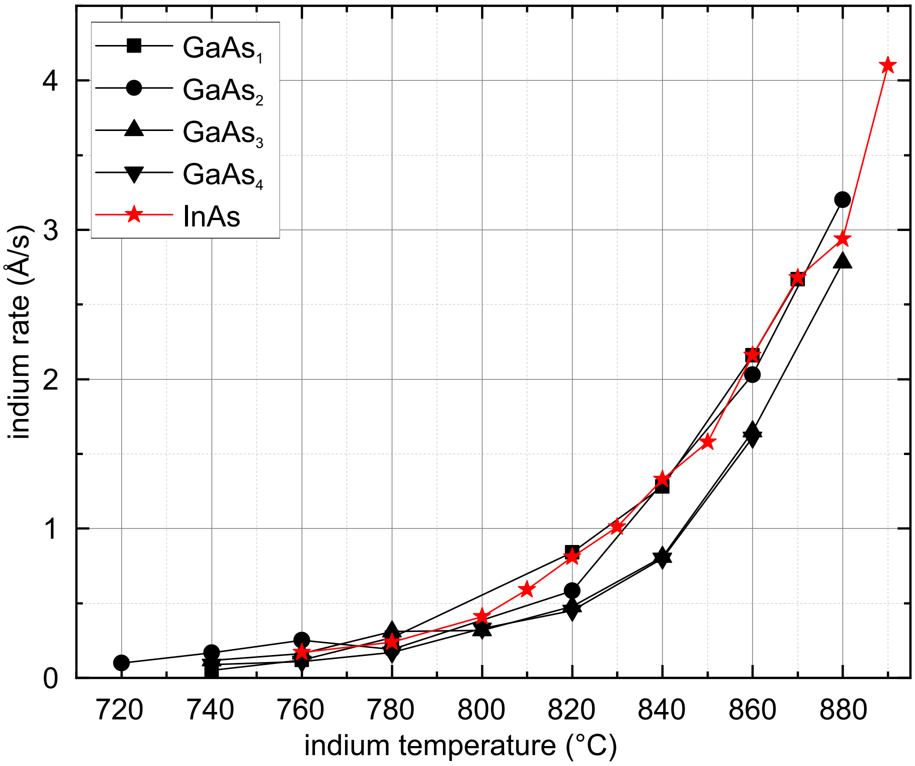

Fig. 4.2: *Indium growth rate as a function of the indium cell temperature via observation of RHEED oscillations on GaAs substrate (black) and on InAs substrate (red).*

The most prominent increase happens, when both single material rates are equal, leading to a doubling of the measured effective growth rate. Thus, the limits of indium rates are rather restricted: low rates are limited e.g. by the weakening of the RHEED signal due to increasing roughness on the substrate surface[4]), making the evaluation of a few ML peaks in the RHEED signal rather difficult. High rates are limited by the rather small critical thickness due to the high indium concentration in the $\mathrm{In}_x\mathrm{Al}_{1-x}\mathrm{As}$, hence a large lattice mismatch, leading to only a few MLs which can be evaluated.
Fig. 4.2 depicts four different calibration runs of the indium cell on a GaAs substrate (black traces). Between those four runs, a deviation of the rates for comparable temperatures over the complete temperature regime can be seen. Especially for critical parts of the step-graded buffer, such as the beginning phases with very small rates and the overshoot

---

[4] This is due to the beginning of the growth of the second ML although the first ML is not completed, as they second ML starts on the larger islands of the first ML. This continues similarly for the third and fourth ML and so on, resulting ultimately in an equilibrium surface roughness which significantly dampens the RHEED signal. This effect is stronger the smaller the growth rate.

part, where the highest rates are required, this deviation brings along an uncertainty of the real indium concentration within the structure. The constant composition part after the buffer (typically with rates at approx. 2 − 3 Å/s) comprising also the active layers of the structure are affected significantly by this variation, leading to unintentional differences in the indium concentration (and thus also thickness variations of critical parts in the active layers). This complicates stable repetition of the heterostructure design regarding sizes and indium concentration, hence making studies and discussions based on these parameters (like Fig. 4.1(b)) difficult. Note, that the highest calibrated rate we achieved on a GaAs substrate (run 2) is 3.2 Å/s at 880°C, for which run 3 suggests only 2.7 Å/s, resulting in an indium concentration difference of 2.4%[5]. This indium concentration range is used in the overshoot, where 84% is almost sufficient for active layers up to 75% indium. However, when growing heterostructures with higher indium concentration in the active layers, also the overshoot concentration has to increase. For this, only an extrapolation of the rates above these temperatures yields the necessary parameters.

4.2.2. RHEED on InAs

An alternative approach to the analysis of RHEED oscillations on lattice-mismatched GaAs is the utilization of a lattice-matched substrate. Indeed, InAs substrates are commercially available, eliminating completely the drawbacks of the induced strain during the calibration on GaAs. In Fig. 4.2, we included a calibration run on a InAs substrate, coloured in red. Although this method allows a significantly faster calibration and first sight is the ideal basis for such a calibration, still certain rate regimes have to be discussed: For small rates below 0.3 Å/s (below 760°C), no data points on the InAs substrates can be obtained. This is due to the increase of surface roughness during the ML growth with which the RHEED signal is continuously dampened. As a consequence, small rates do not yield a sufficient amount of oscillations before they vanish due to the dampening. The evaluation in this range was thus easier on the GaAs substrate, as the Al rate added up with the indium rate, allowing to obtain a rather small indium rate due to a higher effective observed rate of In and added Al. However, the InAs substrate allows the calibration of higher indium rates compared to GaAs, because the Al does not have to be added up. For this, enough oscillations can be observed for significantly higher rates before the signal is dampened, here up to 4.1 Å/s at 890°C in Fig. 4.2.

Comparing both calibrations, the InAs substrate-based calibration lies within the maximum deviations of the four GaAs-based calibrations, thus we cannot decrease the error margin of the rate calibration by using InAs substrates for a RHEED-based rate calibration.

4.2.3. TEM of InAs-QWs in AlSb

A completely different ex-situ approach for rate calibration compared to the evaluation of RHEED oscillations is the analysis of layer thickness of InAs-QWs embedded in lattice-matched AlSb via transmission electron microscopy (TEM). Such calibrations could be conducted in-house with the group of Prof. Zweck, until recently. On a GaAs substrate,

---

[5] for a given Al rate 0.6 Å/s

a buffer layer comprising GaSb, AlSb and AlGaSb was grown to overcome the lattice mismatch. Onto this buffer several InAs QWs were grown, embedded in AlSb barriers.

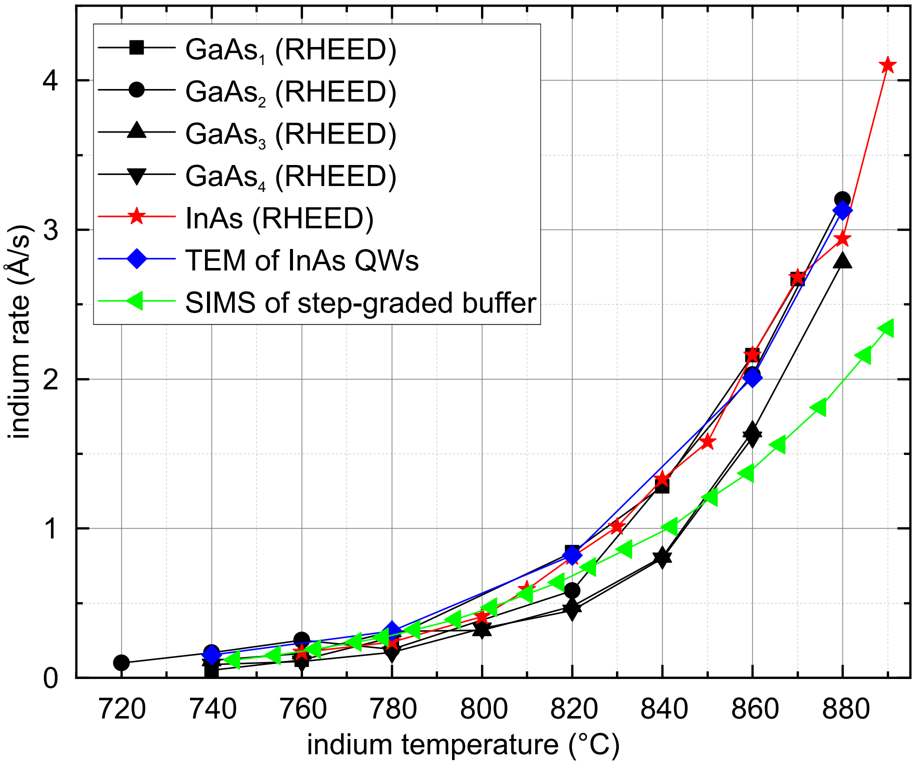

Fig. 4.3: *Indium growth rate as a function of the indium cell temperature via observation of RHEED oscillations on GaAs substrate (black) and on InAs substrate (red), from TEM layers thickness analysis of InAs QWs embedded in AlSb (blue) and from indium concentration analysis via SIMS (green).*

InAs, AlSb and GaSb are lattice-matched III/V materials, while InAs provides a good contrast to AlSb in a TEM analysis. Each InAs QW is grown with a different indium cell temperature (thus a different rate) for a given time. From the TEM images, we were able to determine the thickness of each QW. From the thickness and the growth time, we are able to determine a growth rate. In Fig. 4.3, the blue trace depicts the rate calibration for such a QW-based heterostructure as well as the calibration traces of the RHEED based measurements. In this measurement, only 5 data points represent the QW-based calibration. Note, that small rates are rather difficult to obtain, as the QW growth with such small rates offers the risk of an increased amount of crystal defects which would decrease the contrast to the neighbouring AlSb. Thus, a full calibration for a complete step-graded buffer cannot be obtained. With only this calibration, too much extrapolation and interpolation would have to be done.
In comparison to the RHEED-based measurements, this calibration fits the InAs-RHEED-based one as well as the first of the GaAs-based one.

4.2.4. SIMS on step-graded buffer samples

Another ex-situ approach is the use of secondary ion mass spectrometry (SIMS) on ternary alloys such as $In_xAl_{1-x}As$ and $In_xGa_{1-x}As$. Determining the concentration x, we can determine the indium rate. We do not have this technique in-house, but it is commercially available. In order to get a sufficient amount of measurement points, we analyzed heterostructure samples with a complete 2DES structure, i.e. with a step-graded buffer and a QW in the active layers. This has two reasons: For one, we do not need to grow additional calibration heterostructures and for another, the complete step-graded buffer yields a high amount of data points, as each layer in the buffer (between 15 and 20 layers) contains a different indium concentration, provided by a different indium rate.

The outcome of this indium rate calibration via SIMS of a heterostructure is depicted in green in Fig. 4.3. As mentioned before, we obtain many data points due to the step-graded buffer. However what stands out is that for temperatures above 820°C, the rates are significantly smaller than the ones from the other methods, even increasing the difference with increasing temperature. Conversely, this means that the indium concentration, which was measured via SIMS, is significantly smaller than the intentional concentration in layers which were grown with cell temperatures above 820°C, leaving a maximum concentration deviation at the maximum indium concentration in the overshoot of 7%. This cell temperature coincides with $In_xAl_{1-x}As/In_xGa_{1-x}As$ layers, where $x > 0.51$. Note here, that the reference sample in a SIMS measurement, which is simultaneously analyzed with the main sample, is a $In_{0.51}Al_{0.49}As$ bulk structure. This suggests, that the conversion calculation of the SIMS data does not fit high indium contents. This was discussed with the staff responsible for this measurements, but there was no solution found for this problem. We had several different heterostructure samples analyzed, also in different measurement runs, and all of them suggested smaller indium contents than intentionally adjusted.

4.2.5. EDX on step-graded buffer samples

In order to overcome the problem of the SIMS analysis with higher indium contents, we chose to determine the material contents in a step-graded buffer structure via energy-dispersive X-ray spectroscopy (EDX) combined with a scanning TEM (STEM) to optimize the spatial resolution. For this analysis, the same heterostructure sample presented with the SIMS anlaysis was used. From the measured indium concentration, we are able to determine the indium rate at a given cell temperature. Fig. 4.4 shows the previously presented calibration runs, now added with the results of the EDX-based measurements in magenta. Here, the trace is in good agreement with the previous calibration methods, consisting (like the SIMS analysis) of a large amount of data points. This helps, to sufficiently map the exponential dependence of the rate. The large difference to the SIMS-based measurement (green) is another strong indication, that the concentration calculation of the SIMS analysis does not model well enough results from high-indium-concentration layers.

Note, that we do not have a long-term study of the rate stability and reproducibility based on this method, however the good matching with the several other calibration methods (despite SIMS) allows us to confidently extrapolate and interpolate the indium rates in the range of 720°C to 900°C.

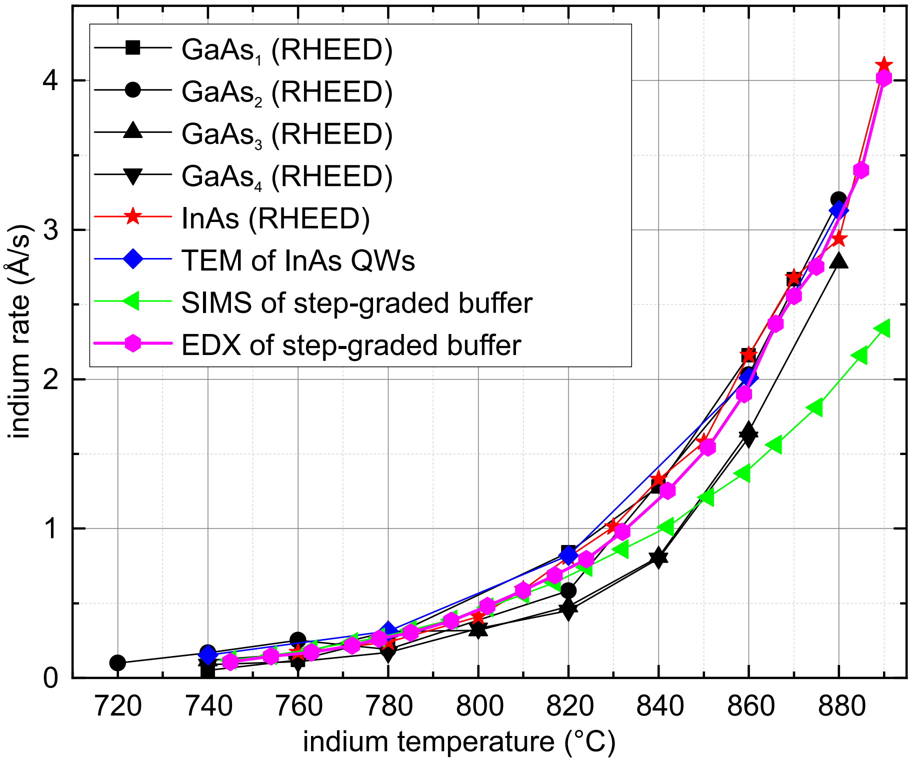

Fig. 4.4: *Indium growth rate as a function of the indium cell temperature via observation of RHEED oscillations on GaAs substrate (black) and on InAs substrate (red), from TEM size analysis of InAs QWs embedded in AlSb (blue), from indium concentration analysis via SIMS (green) and via EDX (magenta).*

The used rate calibration based on this method produces indium-based heterostructures for different requirements, for which experiment (optics and transport) and simulation are in very good agreement, also allowing a stable reproducibility across many heterostructures. With this, we are now also confident, that tangible experimental differences of results can be traced back to the intentional changes and differences during the growth and not due to unintentional fluctuations and/or uncertainty due to insufficient cell calibration.

5. Gating of InAlAs-based 2DESs: The role of intrinsic InAlAs deep donor defects

Over the course of this thesis, one of the most important tools to gain overview information of a heterostructure is to measure the gate response of a sample, i.e. the electron density as a function of the topgate (TG) voltage. This gives an insight into the electrostatics within the system. We have found reproducible peculiarities in the gate responses across many samples, which we can link to heterostructure materials properties. Here, in Ch. 5, we discuss two exemplary samples A and B in detail. They are similar to samples A and B presented in Ch. 4 (see layout in Fig. 4.1(a)). Both samples have the same heterostructure layout, consisting of a 20 nm InGaAs QW embedded in InAlAs: 120 nm of InAlAs the InGaAs QW (towards the substrate) and 130 nm above the QW (towards the surface). Each heterostructure is capped with 2 nm InGaAs to prevent oxidation damage via Al suboxides. A and B only differ in their indium concentration: 81% for sample A and 75% for sample B. The heterostructures were grown on a semi-insulating GaAs (100) substrate, where a $In_xAl_{1-x}As$ step-graded buffer is used to overcome the lattice mismatch from GaAs to the high-indium-concentration active layers (see Sec. 3.1.2).
Parts of the data and the discussion in this chapter have recently been published in *Physical Review Applied*, [65].

5.1. Gate response

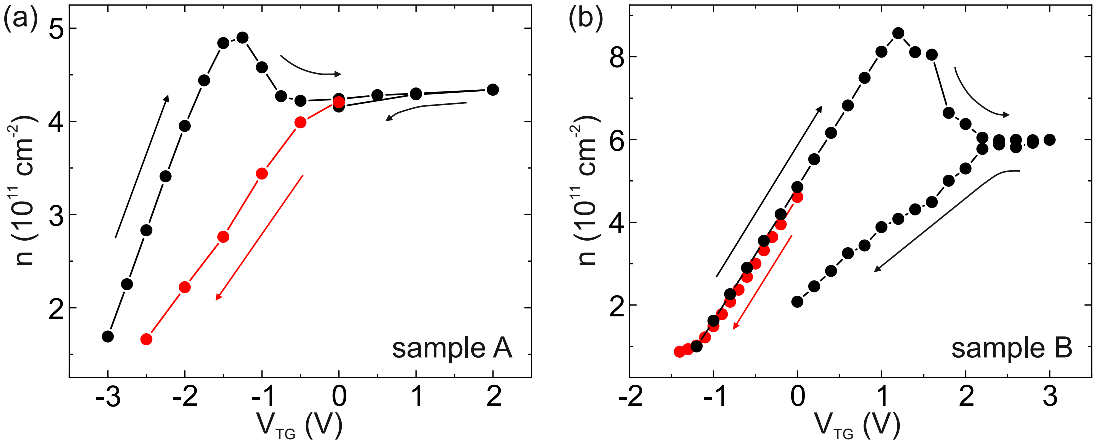

Fig. 5.1: *Electron density n as a function of TG voltage V_{TG} for sample A (a) and sample B (b). The 2DES is depleted below metal-insulator transition (red) after the cooldown to 4.2 K, followed by a TG upsweep and a downsweep back to $V_{TG} = 0$ V subsequently.*

The gate response, i.e. the electron density n as a function of the TG voltage V_{TG}, of sample A (81% indium) is presented in Fig. 5.1(a). At room temperature (RT), $V_{TG} = 0\,V$ was applied and then the sample was cooled down to $T = 4.2\,K$, yielding $n = 4.2 \times 10^{11}\,cm^{-2}$. Then, the system was depleted by applying $V_{TG} < 0$ V (red trace in Fig. 5.1(a)) below the metal-insulator transition (MIT), occurring at $V_{TG} < -2.5$ V with $n < 1.8 \times 10^{11}\,\mathrm{cm}^{-2}$ (last point of the red trace in Fig. 5.1(a)). After going to $\mathrm{V_{TG}} = -4\,\mathrm{V}$, we start a $\mathrm{V_{TG}}$ upsweep (black trace in Fig. 5.1(a)), resulting in electron accumulation for $\mathrm{V_{TG}} > -3$ V onwards. The black trace differs from the red trace, indicating a clear hysteresis in the gate response. Although both branches exhibit a linear dependence, indicating a classical field-effect gate response, the black trace features a steeper slope than the red trace. This suggests a stronger capacitive coupling of the TG to the 2DES in the QW. The linear part of the black trace ends at $\mathrm{V_{TG}} = -1.4$ V with a maximum density $n_{\mathrm{peak}} = 4.9 \times 10^{11}$ cm^{-2}. When $\mathrm{V_{TG}}$ is increased even further, i.e. more electrons are accumulated in the QW, the density starts to decrease, forming a characteristic peak in the density. By increasing $\mathrm{V_{TG}}$ even further, the decrease of the density eventually saturates at $\mathrm{V_{TG}} = -0.5$ V with $n_{\mathrm{sat}} = 4.3 \times 10^{11}$ cm^{-2}. Up to $\mathrm{V_{TG}} = +2$ V, the density then does not significantly increase or decrease anymore. Now, by decreasing $\mathrm{V_{TG}}$, the density does not react down to $\mathrm{V_{TG}} = +1$ V. This indicates a loss of the capacitive coupling of the TG to the 2DES. Only when $\mathrm{V_{TG}} < +1$ V, the density decreases, for which the density at $\mathrm{V_{TG}} = 0$ V coincides precisely with the density value directly after the cooldown at $\mathrm{V_{TG}} = 0$ V, visualized by the merging of the black trace coming from $\mathrm{V_{TG}} > 0$ V and the red trace. When the downsweep is continued, the density exactly matches the red trace again down to the MIT, suggesting a closed hysteresis loop. This loop remains stable for several TG voltage cycles.

We can derive two major observations from the gate response in Fig. 5.1(a): First, the sample allows a linear gate control of the density in two distinctive gate voltage intervals (red and black trace), but with different slopes of the linear dependence. Second, the maximum achievable electron density in the system is smaller in the regime with the smaller capacitive coupling (red trace). These observations suggest, that the gate controllability of the system strongly depends on the electrostatic configuration before the cooldown as well as on the gate action history applied to the sample. Most interestingly, these observations seem to be in line with state of the art in the literature for similarly designed heterostructures, although it is rarely commented on: the gating behavior of such samples vary significantly [23–29]. This suggests, that there is a correlation between the exact heterostructure layout and the gating properties of these kind of samples. As most of the previously mentioned reports are based on heterostructures with 75% indium, and to further illustrate the correlation of the design the gate behavior, we show the gate response of sample B in Fig. 5.1(b). As outlined before, sample B is identical to sample A despite the indium concentration (75% instead of 81%) in the active layers. The heterostructure layout is displayed in Fig. 4.1(a). The gate response of this sample B in Fig. 5.1(b) qualitatively displays the same distinctive hysteretic features as sample A in Fig. 5.1(a) does. However, three striking differences appear when taking a closer look. First, after the cooldown from RT to $T = 4.2\,\mathrm{K}$ at $\mathrm{V_{TG}} = 0$ V, the sample is initialized in the branch with the steeper linear gate-control regime (red race in Fig. 5.1(b)), while sample A was initialized in the regime with the smaller slope. Second, when the system in sample B is depleted into the MIT by applying $\mathrm{V_{TG}} < 0$ V, a subsequent upsweep of the TG voltage results in electron accumulation equivalent to the prior depletion, i.e. the black and the red trace in Fig. 5.1(b) are identical. Finally, and third, sample B yields a higher maximum density $n_{\mathrm{peak}} = 8.5 \times 10^{11}$ cm^{-2} as well as a higher saturation density $n_{\mathrm{sat}} = 6.0 \times 10^{11}\,\mathrm{cm}^{-2}$ compared to sample A.

According to these experiments, the properties of the 2DES strongly depend on the gate-sweep history applied to the sample. In order to get a more detailed understanding of the underlying mechanisms, we take a look at the gate properties, when we modify the electrostatics of the samples at RT.

5.2. Biased cooldown

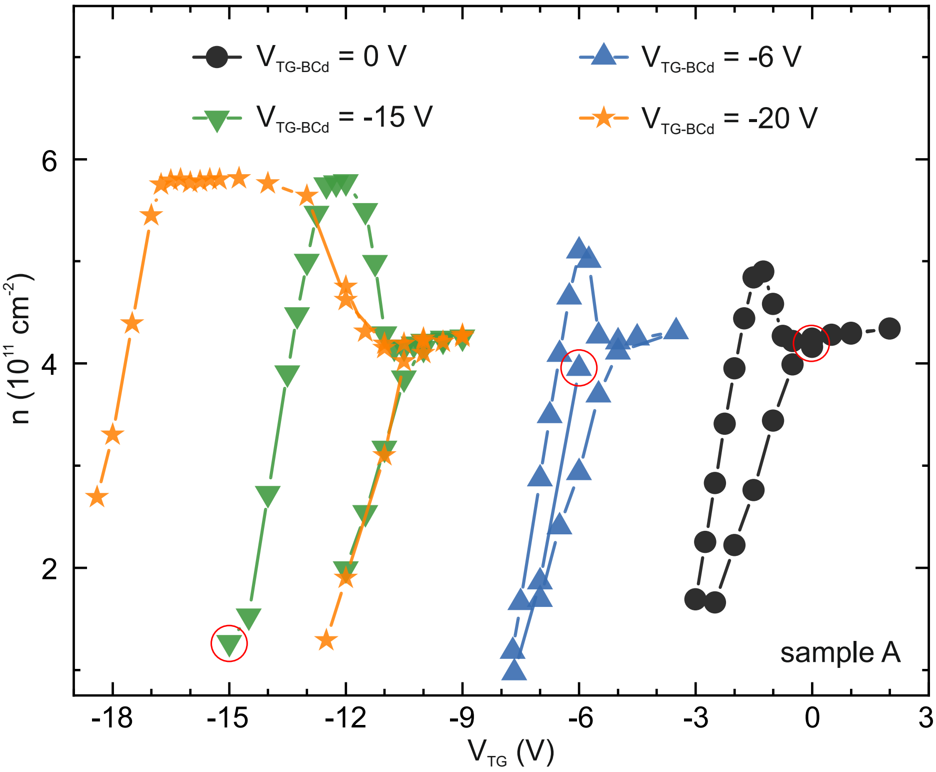

Fig. 5.2: *Electron density n as a function of V_{TG} of sample A for four representative biased-cooldown voltages V_{TG-BCd}. The red circle indicates the first measurement point after cooldown at each V_{TG-BCd}. For $V_{TG-BCd} = -20$ V, the system was already below the MIT, thus the first measurement point is with the first electron accumulation in the V_{TG} upsweep at $V_{TG} = -18.5$ V.*

We apply a specific voltage V_{TG-BCd} to the TG at RT, in the following termed as biased cooldown (BCd). Then, the sample is cooled down to $T = 4.2$K with this applied TG voltage, followed by a gate voltage cycle similar to the cycles in 5.1(a) and (b). The corresponding gate responses of the 2DES, exemplarily for sample A, for four different biased cooldown runs are displayed in Fig. 5.2. The starting point of each BCd run is cycled in red, corresponding to the applied V_{TG-BCd}. The run at $V_{TG-BCd} = 0$ V (black trace) is identical to Fig. 5.1(a), which starts in the linear regime with the smaller slope. Applying now a small negative voltage $V_{TG-BCd} = -6$ V (blue trace), two important changes occur: First, the initializing depletion beyond MIT builds a branch with an intermediate slope, where a subsequent upsweep exhibits a steeper slope and a following depletion leads to a smaller slope. Second, the maximum electron density is higher in comparison to the run at $V_{TG-BCd} = 0$ V (black trace). We can confirm this trend by applying reducing the voltage even more to $V_{TG-BCd} = -15$ V (green trace), for which the first measurement point now lies on the branch with the steepest slope while the maximum density is again higher compared to the black and the blue trace. Note, that the peak structure of the green trace is widened compared the the blue and the black trace. Going even further to $V_{TG-BCd} = -20$ V (orange trace in Fig. 5.2), the system is already below the MIT at RT. Thus, we have to accumulate with a V_{TG} upsweep at 4.2 K, leading to the first measurement point at $V_{TG} = -18.5$ V. Note here, that the accumulation is also on the branch with the steepest slope, similar to the green trace. Additionally, the peak structure is now widened into a plateau with a only slightly increased maximum density.

From these biased-cooldown experiments, which are reproducible over several samples, we can draw two conclusions: For an application-oriented use, we demonstrate here that proper adjusted biased cooling of such samples allows to initiate the system in a reproducible and well-defined state, e.g. here into the branch with the steepest slope. Secondly, and most strikingly, the green trace in Fig. 5.2 very much resembles the gate response of sample B (75% indium) with $V_{TG-BCd} = 0$ V in Fig. 5.1(b). The fact that proper biased cooling allows us to make a sample with 81% indium behave like a zero-biased sample with 75% indium thus strongly suggests the gate response of such 2DESs to be closely linked to the intrinsic microscopic electrostatics of the heterostructure. With this, we are able to identify specific reproducible regimes within the gate response across the samples presented in Fig. 5.1, which we discuss and analyze in the following.

5.3. Charge-transfer model for the gate response

The hysteresis pattern of the gate response can be divided into several reproducible regimes, characteristic for the electrostatics within the heterostructure. These regimes are numbered with Roman numerals as displayed in Fig. 5.3 and do not necessarily coincide with the chronology of the applied TG voltage after the cooldown to 4.2 K. Incidentally, this is the case for the displayed gate response of sample B in Fig. 5.3, but the V_{TG} chronology of the gate response of sample A in Fig. 5.1(a) proves this wrong. Based on these regimes, we are able to develop a phenomenological model what we denote as a charge-transfer-model (CTM), which is supported by experimental results from many heterostructures with different indium contents and different QW depths beyond 50 nm below the heterostructure surface. As an example, we illustrate this model and the discussion based on the results of sample B.

5.3.1. Regime I

The linear segment of the gate response with the steeper slope, suggesting a capacitive coupling described by the classical field effect, is defined as regime I. This regime is experimentally characterized by two observations: First, V_{TG} upsweeps and downsweeps within this regime coincide precisely along this branch and only along this branch. Note, that this is not true for all other regimes. Second, the electron density reaches its equilibrium value instantly when $\mathrm{V_{TG}}$ is swept to the next measurement value, regardless of $\mathrm{V_{TG}}$ up- or downsweep. This instant reaction is valid again only in this regime I. In all the other following regimes, the experimental determination of the electron density requires a settling time after each $\mathrm{V_{TG}}$ action, before the equilibrium density value can be obtained. We will also see in the following, that this settling can vary from several tens of seconds to several tens of minutes.

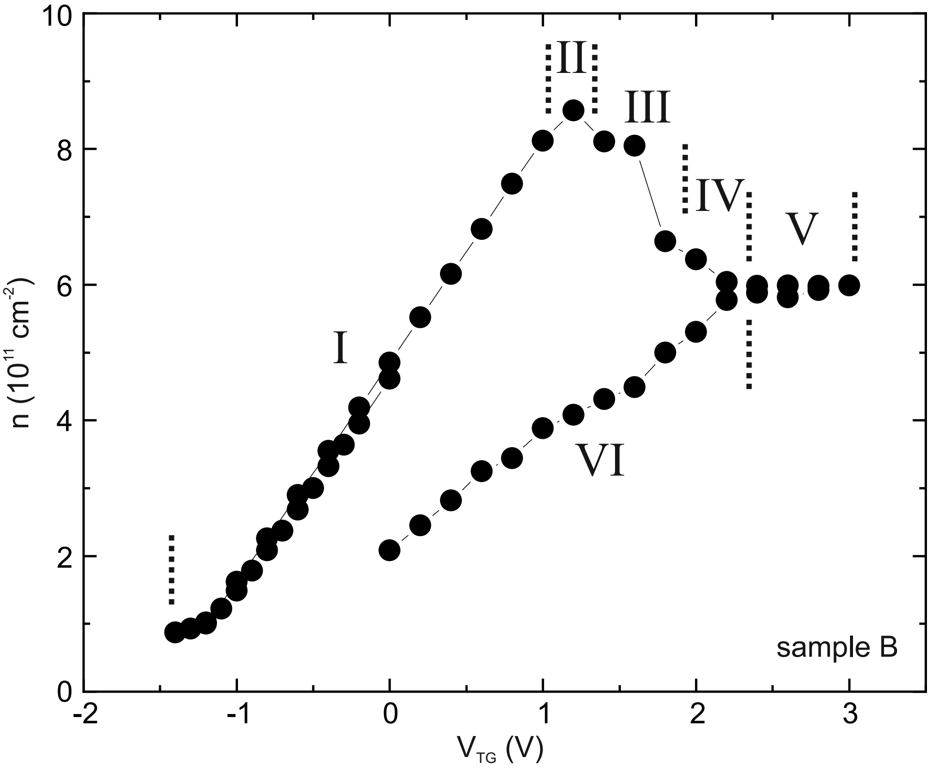

Fig. 5.3: *Electron density n of sample B as a function of the TG voltage* V_{TG} *at* $V_{\mathrm{TG-BCd}} = 0$ *V. The Roman numerals indicate the different electrostatic regions of the gate response, which are discussed in the text.*

5.3.2. Regime II

Regime I has an upper limit, defined as regime II, which appears either as a sharp peak (see Fig. 5.3), or a more elongated peak which even transforms into a plateau (for $\mathrm{V_{TG-BCd}} = -20$ V in Fig. 5.2). In this regime II, the density saturates even when $\mathrm{V_{TG}}$ is increased. This could either be the result of a loss of the capacitive coupling between the TG and the 2DES in the QW or a loss of electrons out of the QW. We can exclude the loss of capacitive coupling, as the electron density still continues to react to a reduction of $\mathrm{V_{TG}}$ immediately for all voltages within regime II. Although a loss of electrons out of the QW seems to be counterintuitive at first sight, a look at the band-edge sketches of the gated heterostructure in Fig. 5.4(a) and (b) makes it more plausible. Note, that these illustrations are schematics and are inspired by self-consistent Schrödinger-Poisson calculations, for which we use parameters from [66] and [57]. During the MBE growth of the InAlAs, intrinsic crystal defects sites, i.e. arsenic antisites, are formed. These arsenic antisites induce two deep-donor-level (DDL) states, lying 0.12 eV and 0.17 eV below the conduction band (CB) edge of the InAlAs [57]. As they act quite effectively as donor states InGaAs and/or InAs QWs embedded in InAlAs, 2DESs with significant electron densities can be formed through this intrinsic doping, although the structure itself is nominally undoped.

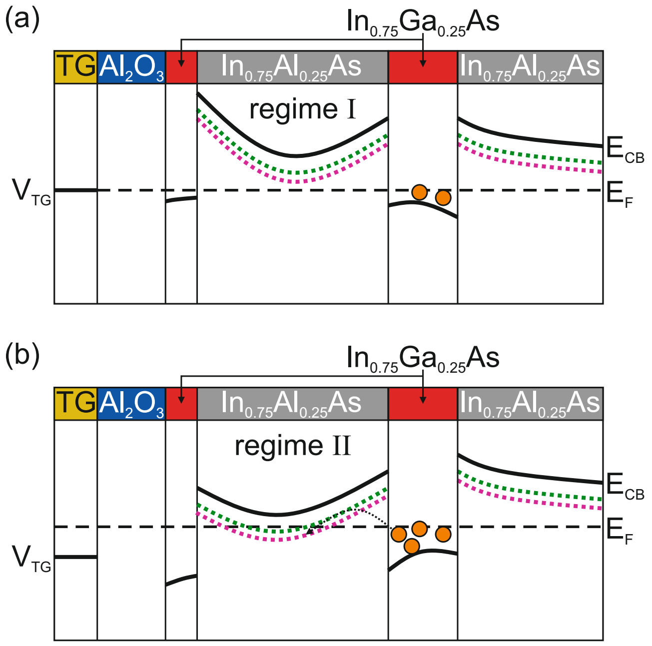

Fig. 5.4: *(a) & (b) Conduction band (CB)-edge sketches of sample B for* $V_{TG} = 0$ *V (a) and* $V_{TG} > 0$ *V (b), each representative for regime I (a) and regime II (b). The colored dotted lines indicate the energetic position of the deep-donor-levels (DDLs) within the InAlAs, lying at* 0.12 *eV (green) and* 0.17 *eV (pink) the below the InAlAs CB edge. By increasing* V_{TG} *(going from regime I to II), electron tunneling from the QW into the InAlAs DDLs sets in.*

Fig. 5.4(a) displays the electrostatic situation for $V_{TG} = 0$ V of sample B, with the CB edge (black lines) as well as the evolution of the two energy levels induced by the DDLs (colored dotted lines) along the growth direction of the heterostructure. The electron population is schematically represented by the orange dots. The evolution of the InAlAs CB edge along the growth direction appears curved due to the ionization of the DDLs. The CB edge even forms a trough-like shape between the heterostructure surface and the InGaAs QW. Note, that this is still for $V_{TG} = 0$ V, i.e. in the regime I, which is characterized in the experiments as a stable configuration.

Now, by applying $V_{TG} > 0$ V, the band edges between the TG and the QW bend downwards. From a certain V_{TG} onwards (start of regime II), a situation like in Fig. 5.4(b) is reached. Note, how the electrons now face an increasingly transparent triangular-shaped potential barrier between the QW and the DDLs in the InAlAs compared to the situation in Fig. 5.4(a). Simultaneously, as the apex of the trough bends downwards, the minimum energy point of the DDLs shifts down to eventually be equal or even below the lowest subband of the QW. Thus, one can expect an increased tunneling probability of electrons from the QW into the DDLs in the InAlAs. These tunneled electrons are then trapped in the DDLs, do not contribute to the transport anymore and thus appear as lost 2DES electrons in our experiments.

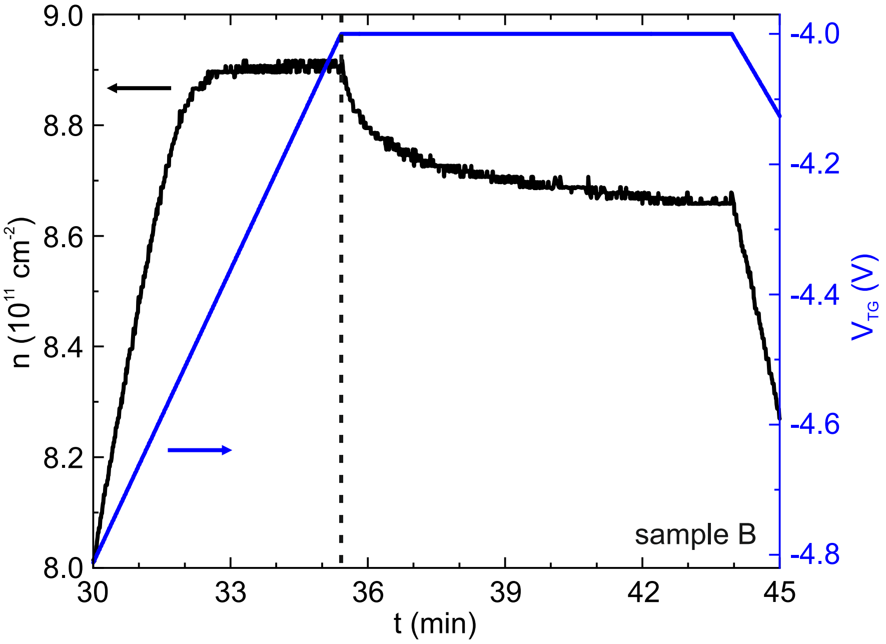

Fig. 5.5: *Electron density n (black) and V_{TG} sweep (blue) as a function of the measurement time t for sample B at $V_{TG-BCd} = -6$ V. Initialized in regime I, the sample evolves into regime II at $t = 32$ min by increasing V_{TG} to $V_{TG} = -4.6$ V. After the gate sweep is stopped in regime II (at $t = 35.3$ min), the density decreases over t.*

The dynamics explained with Fig. 5.4(a) & (b) can be experimentally verified by the measurement displayed in Fig. 5.5. Here, sample B is cooled down at $V_{TG-BCd} = -6$ V and is set to regime I at $V_{TG} = -4.8$ V. From there, we sweep the TG up to $V_{TG} = -4.0$ V and thus the sample into regime II while simultaneously measuring the electron density n over time t. Regime I is characterized by the instant reaction of the electron density to the classical field effect, i.e. increasing linearly with V_{TG}. At $V_{TG} = -4.6$ V, the increase of the density begins to flatten (onset of regime II) which evolves by a further increase of V_{TG} into a density saturation, even though V_{TG} is still increased. In the exact moment when the V_{TG} sweep is stopped, here in Fig. 5.5 at $V_{TG} = -4.0$ V (at $t = 35.3$ min) as an example, the density immediately begins to decrease over a period of several minutes. This clearly illustrates the onset as well as the ongoing of a loss of electrons out of the QW. Additionally, Fig. 5.5 serves as evidence, that the capacitive coupling of the TG to the 2DES in the QW is not lost within regime II. This can be seen by the immediate reaction of the electron density to a V_{TG} downsweep, started at $t = 44$ min, according to the classical field effect. This experiment shows also the need of a settling time for the density to reach its equilibrium value after a specific V_{TG} value in regime II is set. As mentioned previously, only regime I does not require this settling time.

5.3.3. Regime III

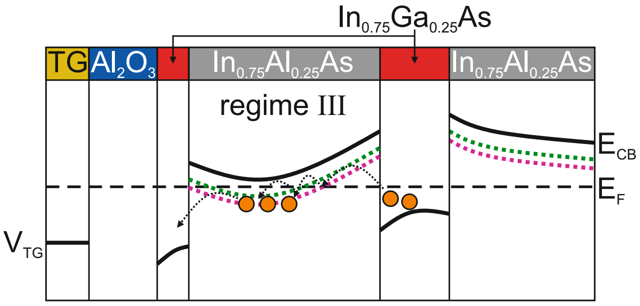

Fig. 5.6: *Conduction band (CB)-edge sketches of sample B for increasing* V_{TG}*, representing regime III. Due to the increasing* V_{TG}*, the triangular-shaped potential barrier between the QW and the InAlAs DDLs becomes more transparent, resulting in a significant loss of electrons out of the QW. Simultaneously, the apex of the trough shifts towards the interface between the semiconductor and the dielectric, facilitating hopping tunneling of electrons from the trough towards the interface.*

When we apply a higher $\mathrm{V_{TG}}$ at the peak structure within regime II, the band tilting becomes even stronger. With this, the triangular-shaped potential barrier between the QW and the DDLs in the InAlAs becomes even more transparent, hence leading to an effectively increased tunneling probability from electrons out of the QW into the DDLs sites in the InAlAs. We can extract from the experiments, that the loss of electrons out of the QW due to this increased tunneling probability outweighs the simultaneous increase of the electron density driven by the classical field effect due to the increasing $\mathrm{V_{TG}}$. Hence, we observe a significant decrease of the electron density although $\mathrm{V_{TG}}$ is increased, which we characterize as regime III.

In the literature, we find values for the defect density of the two types of the DDLs to be $N_D \approx 3 \times 10^{16}$ cm^{-3}, with which we can calculate the average distance between two adjacent DDLs defect sites of the same type in the InAlAs, yielding $d \approx 32$ nm. With the experimental determination of the dielectric constant of InAlAs ($\epsilon_{sc} \approx 13.7$) as well as of the effective mass ($m_e^* = 0.041 \cdot m_e$) of a similarly structured QW [67], we are able to calculate the effective Bohr radius of an electron bound to such a defect site[6], yielding $a_0^* \approx 18$ nm. Comparing the radius resp. the diameter with the distance between the sites suggests a field-assisted charge transfer through the InAlAs via multistep tunneling (hopping), i.e. electron can tunnel via the DDLs defect sites through the InAlAs. We can observe this tunnelling process in the experiments by the rather long settling time of the electron density after a each adjustment of $\mathrm{V_{TG}}$. At the same time, when $\mathrm{V_{TG}}$ is increased, the apex of the trough (caused by the DDLs) shifts towards the interface between the semiconductor and the dielectric. Thus, the $\mathrm{V_{TG}}$ increase facilitates the electron multistep (hopping) tunneling via DDL defect sites from the apex of the trough towards the interface, sketched in Fig. 5.6. Note that in our understanding, when an electron arrives at this interface, it gets trapped. We have indeed good experimental indications for this picture,

---

[6] $a_0^* = (\epsilon_{sc}/m_e^*)/(4\pi\epsilon_0\hbar^2/e^2)$

displayed exemplarily by the gate responses in Fig. 5.7: A V_{TG} variation within regime I (red trace) does not lead to a hysteresis, hence the V_{TG} downsweep to $V_{TG} = -7.5$ V matches the branch of subsequent V_{TG} upsweep (red trace on red trace). When regime I is left however, regime II and onwards, a V_{TG} downsweep immediately opens up a hysteresis, i.e. the downsweep branch differs from the previous upsweep branch. This opening of a hysteresis reflects the loss of electrons from the 2DES in the QW, which we interpret as a charge transfer via the InAlAs DDL sites towards resp. into the interface, where trapping occurs.

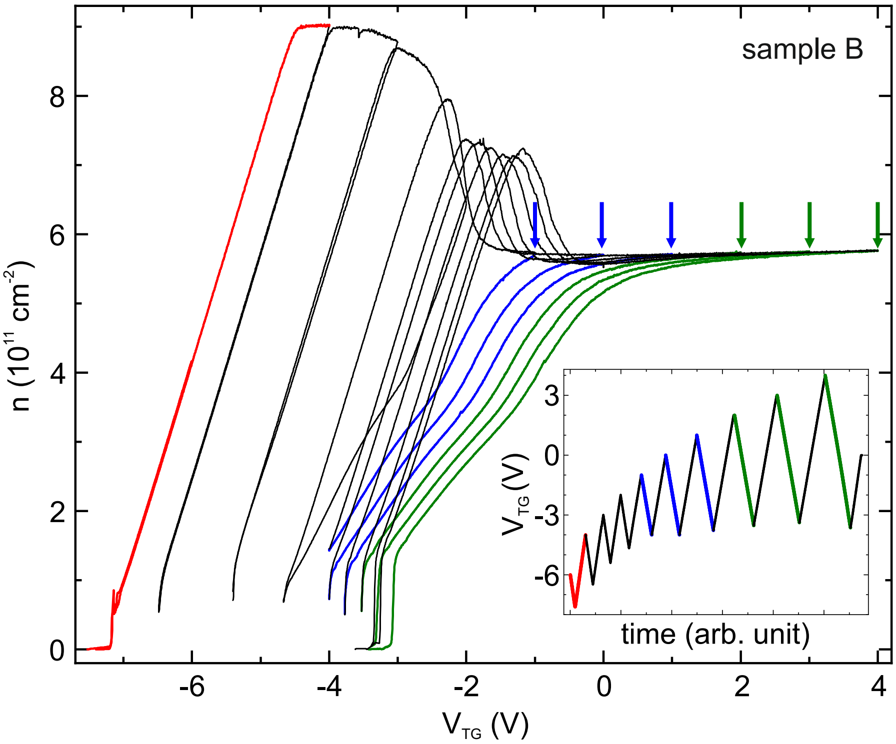

Fig. 5.7: *Electron density n of sample B at $V_{TG-BCd} = -6$ V as a function of V_{TG}. The inset depicts the V_{TG} sweeps, indicating with the colors the different regions within the gate response. The red line indicates the initialization and the first downsweep of the sample, here representative of regime I. Blue indicates V_{TG} downsweeps within regime VI and green within regime V.*

What our experiments also show is, that from regime II onwards, the trapping at the interface is rather stable. We observe, that once an electron is trapped in this interface, i.e. the hysteresis in the gate response opens up, a large negative V_{TG} can not reset the system resp. bring the electron back. This is visualized in the experiment in Fig. 5.8, where sample B at $V_{TG-BCd} = -6$ V is set to regime I (red trace). When regime II is reached, here with a V_{TG} upsweep to $V_{TG} = -4$ V (and a subsequent downsweep opens up a hysteresis), neither a downsweep to $V_{TG} = -7.5$ V nor to $V_{TG} = -9$ V resets the system so that a subsequent upsweep matches the initial branch of regime I (red trace). Only by heating up the sample to RT, the system undergoes a full reset.

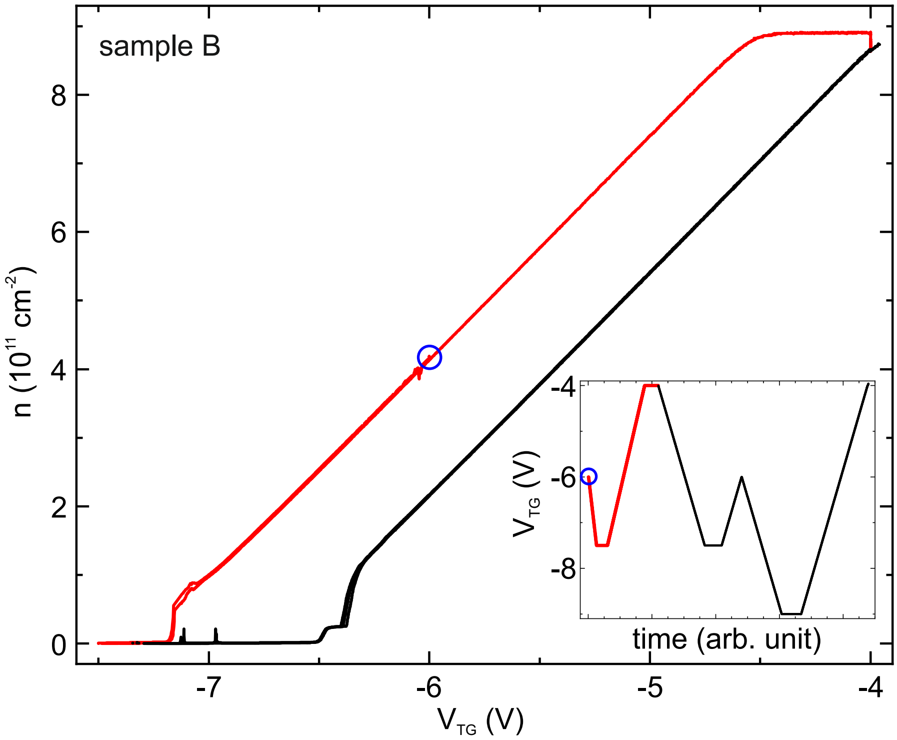

Fig. 5.8: *Electron density n of sample B at $V_{\mathrm{TG-BCd}} = -6$ V as a function of V_{TG}. A 2DES depletion is initiated from regime I (red) and from regime II (black). Once the system is brought from regime I to II and a depletion is permored, a large negative V_{TG} (down to $V_{\mathrm{TG}} = -9$ V) cannot restore the system to be in the initial branch (red). The inset depicts the corresponding V_{TG} sweeps.*

5.3.4. Role of the semiconductor-dielectric interface

In our understanding, the observed stable trapping occurs most plausible at the interface between the semiconductor and the dielectric, where it results from the rather complex morphology at this interface: For one, this interface represents the sharp transition between the single-crystalline semiconductor heterostructure and the amorphous Al_2O_3 deposited via atomic layer deposition (ALD). Thus, this interface hosts a significant concentration of point defects, which provide an energetically broad distribution of states [68–74], covering shallow defects inducing instabilities due to multiple trap and release processes as well as deep defects contributing to a (meta-)stable trapping. For another, this interface has been shaped several times by various environmental influences and sample-processing steps, e.g. post-MBE-growth oxidation of the InGaAs cap layer at air as well as (possibly partial) self-cleaning of the oxidized surface with the deposition steps within the Al_2O_3 deposition via ALD [75–82]. Ultimately, the result is a spatially inhomogeneous hummocky potential landscape at this interface.

5.3.5. Regime IV

The density drop in regime ends in the experiments with a smooth transition into a density saturation, where then the electron density stays constant even when V_{TG} is increased further. This is defined as regime IV. This density saturation indicates the occurence of a partial screening of the topgate electric field, resulting from a sufficient population of trapped negative charges at the interface (transferred during regimes II and onwards). As a consequence of this partial screening, the band-edge profile of the InAlAs should be flattened as depicted in Fig. 5.9 compared with the unscreened situation. Due to this flattening, the triangular-shaped barrier between the QW and the InAlAs becomes less transparent again, thus effectively decreasing the electron tunneling rate from the QW into the InAlAs defect sites. At the same time, we believe this described process to be self-limiting, thus explaining the saturation of the 2DES density: each incremental increase of V_{TG} is directly compensated by an equivalent tunneling-assisted screening.

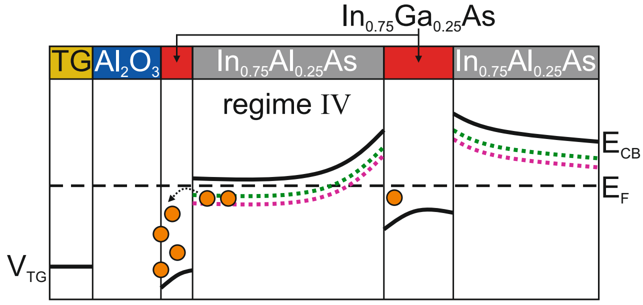

Fig. 5.9: *Conduction band (CB)-edge sketches of sample B for increasing (large)* V_{TG}*, representing regime IV. Due to the further increasing* V_{TG}*, a sufficient amount of electrons at the interface between the semiconductor and the dielectric is trapped, resulting in a partial screening of the TG electric field and thus to a flattening of the bandstructure.*

From our measurements we obtain good experimental evidence, that the mentioned screening of the TG electric field in regime IV is only partial. In order to visualize this, we take a look at Fig. 5.7 again, which already allowed us to iollustrate the loss of 2DES electrons in regimes II and III. Now, we consider V_{TG} downsweeps starting from IV (indicated in blue with blue arrows marking the starting point of each downsweep). For any given V_{TG} value within -1 V and $+1$ V, the 2DES density always immediately reacts to a V_{TG} downsweep, indicated by the three blue traces. This immediate reaction to a V_{TG} downsweep during the density saturation demonstrates, that the screening is only partial.

Note here, that over the whole regime IV, the system always immediately reacts to a gate action (at least for V_{TG} downsweeps, as the most part of regime IV is characterized by a density saturation during an upsweep). With Fig. 5.7, this is valid up to $V_{\mathrm{TG}} = +1$ V. Increasing V_{TG} even further, a point occurs where the access of the TG to the 2DES, i.e. the capacitive coupling, is completely lost. This can be seen by the downsweeps in Fig. 5.7 indicated in green, from $V_{\mathrm{TG}} = +1$ V up to $+4$ V. In these three downsweeps (starting point indicated with green arrows), the density does not immediately react to a V_{TG} action, i.e. remains constant. Only after a certain voltage, the 2DES density begins to decrease with the decreasing V_{TG}. This suggests, that a regime V exists, which is characterized by a full screening of the TG electric field to the 2DES.

5.3.6. Regime V

The translation of this experimental observation, in our understanding, is that when the interface between the semiconductor and the dielectric reaches a critical trapped electron population with increasing V_{TG}, the partial screening from regime IV evolves into a full screening, i.e. regime V. Thus, one cannot obtain adjustments of the 2DES density via a variation of V_{TG} anymore. This full screening was observed by Shabani *et al.* [29] for comparable gated heterostructures but with thicker (10 nm) InGaAs cap layers.

Note here a peculiar detail in our experiments: although the electron density, which is trapped at the interface between the semiconductor and the dielectric is large enough to fully screen the electric field resp. the action of the TG to the 2DES, it does not contribute to the transport of the measured system. Even in this regime V, we do not detect experimental signatures of parallel conduction over the whole range of samples investigated during this thesis. In our understanding, this is likely due to the previously mentioned hummocky potential landscape, which has formed at the interface: such a potential landscape plausibly hosts puddle-like potential minima, where charges can be locally trapped. From there, these charges at best can only hop between puddles and therefore only negligibly contribute to the measured transport.

5.3.7. Regime VI

After going through the up to here mentioned regimes I to V, a TG downsweep completes the largest observable gate hysteresis, characterized by a branch denoted as regime VI. We have defined this branch as the one with a smaller linear slope in Figs. 5.1, 5.2 and 5.3. In the latter, the linear branch denoted as regime VI has a significantly smaller slope than the slope in regime I. Additionally, we observe a rather long settling of several tens of minutes for the 2DES density to reach an equilibrium value after a variation of V_{TG} within the regime VI branch, contrary to regime I. This behavior is similar to the dynamics in regimes II, III and IV, indicating again here a substantial charge transfer during this regime VI. This motivates a closer look at this branch, depicted in Fig. 5.10: For sample B at $V_{TG-BCd} = -6$ V, a V_{TG} downsweep from $V_{TG} = -1$ V to -1.2 V, results in a decrease of the 2DES density, indicating that the capacitive coupling of the TG to the 2DES after regime V is restored again. Stopping the V_{TG} downsweep at $V_{TG} = -1.2$ V and waiting for a given duration (represented by the horizontal line in the inset in Fig. 5.10), a significant increase of the 2DES density over several minutes can be observed, although V_{TG} is kept constant (visualized by the vertical evolution of the density at $V_{TG} = -1.2$ V in Fig. 5.10). By now sweeping V_{TG} up again, three striking details are revealed: First, the slope of this upsweep branch is higher than the slope of the previous downsweep. Second, the 2DES density settles instantly within this upsweep compared to the rather long settling time during the previous downsweep. And third, a subsequent downsweep after this downsweep does not open up a hysteresis.

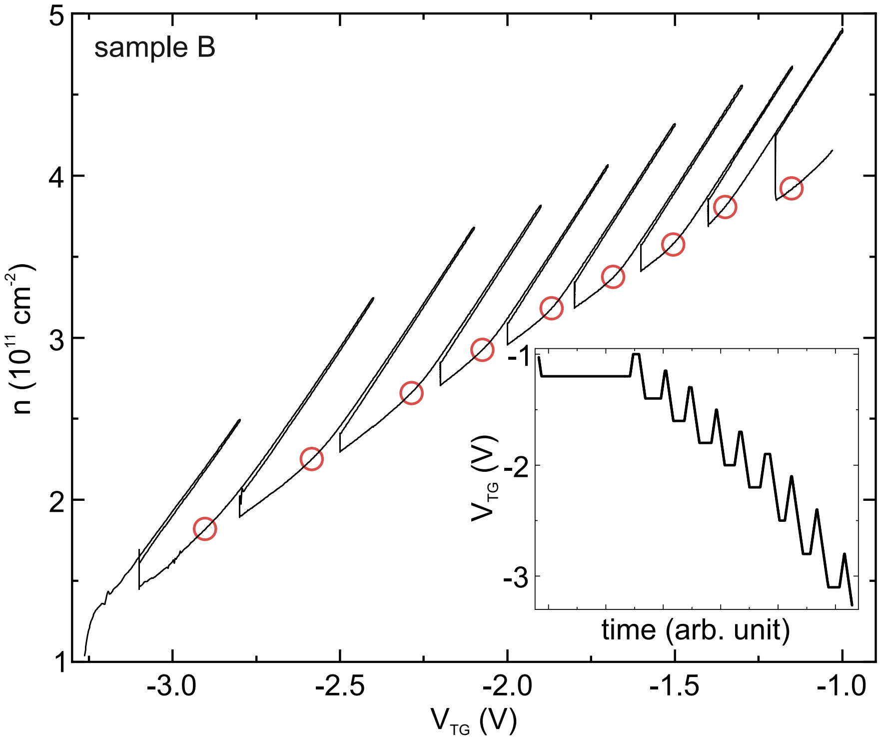

Fig. 5.10: *Electron density n of sample B at* $V_{\mathrm{TG-BCd}} = -6$ *V as a function of* V_{TG} *within regime VI. Several* V_{TG} *downsweeps are performed, each specifically interrupted by a waiting period and a subsequent up- and downsweep again. The red circles indicate the transition point of the slope in each downsweep branch due to the onset of a charge transfer. The inset depicts the corresponding* V_{TG} *sweeps.*

This described complex behavior can be explained as follows: During a V_{TG} downsweep, the depletion caused by the TG is counteracted by a re-transfer of electrons, which were previously transferred from the QW towards the interface during regimes II - V. We cannot distinguish, where this re-transferred electrons had previously been trapped, either at the interface or in DDLs. This re-transfer is not a complete restoration of all the electrons which appeared as lost electrons from the QW, as some of them are irreversibly trapped and cannot be brought back by a large negative V_{TG} (see Fig. 5.8). Hence, they are not participating in this re-transfer. Due to the V_{TG} downsweep, the QW becomes energetically favorable for the electrons, thus they are accumulating in the QW again, which manifests itself in the experiment in two ways: First, the slope of the branch is smaller due to the counteraction and second, the density increases during the waiting time (e.g. at $V_{\mathrm{TG}} = -1.2$ V). This re-transfer however does not operate in the V_{TG} range of a following upsweep and a subsequent downsweep, as the slope of the upsweep branch is steeper and the subsequent downsweep does not open up a hysteresis. Even more, as long as a specific V_{TG} in the subsequent downsweep is not reached (red circles), hysteresis does not appear. This clearly indicates, that the system is, within a certain ΔV_{TG}, in an electrostatic metastable state. A better visualization of this can be obtained when we zoom in on a part of Fig. 5.10, depicted in Fig. 5.11: within a downsweep, the slope transitions from a steeper one (red dotted line) to a smaller one (blue dotted line) when a specific V_{TG} is reached (red circle). This transition point marks the recommencement of the electron transfor back into the QW. Note here, that the V_{TG}-position of the transition depends on the length of previous waiting time. In Fig. 5.11, the waiting time at $V_{\mathrm{TG}} = -1.2$ V (vertical line in the main graph and horizontal line in the inset) is significantly longer than the waiting time at $V_{\mathrm{TG}} = -1.4$ V: this results in a larger ΔV_{TG} between the waiting time at $V_{\mathrm{TG}} = -1.2$ V and the subsequent transition point (red circle) at $V_{\mathrm{TG}} \approx -1.35$ V compared with the ΔV_{TG} to the left of the waiting time at $V_{\mathrm{TG}} = -1.4$ V. This shows, that the abovementioned electrostatic metastable state significantly depends on the dynamics in the measurement sequence, i.e. downsweep, waiting time, upsweep, downsweep. Since this electron re-transfer can be observed over the nine processes in Fig. 5.10 throughout the whole branch of regime VI down to the MIT at $V_{\mathrm{TG}} = -3.25$ V, we show here that the complete regime VI represents an unstable gating regime, where the TG-conducted depletion of the 2DES is constantly counteracted by an electron re-transfer from the heterostructure into the QW.

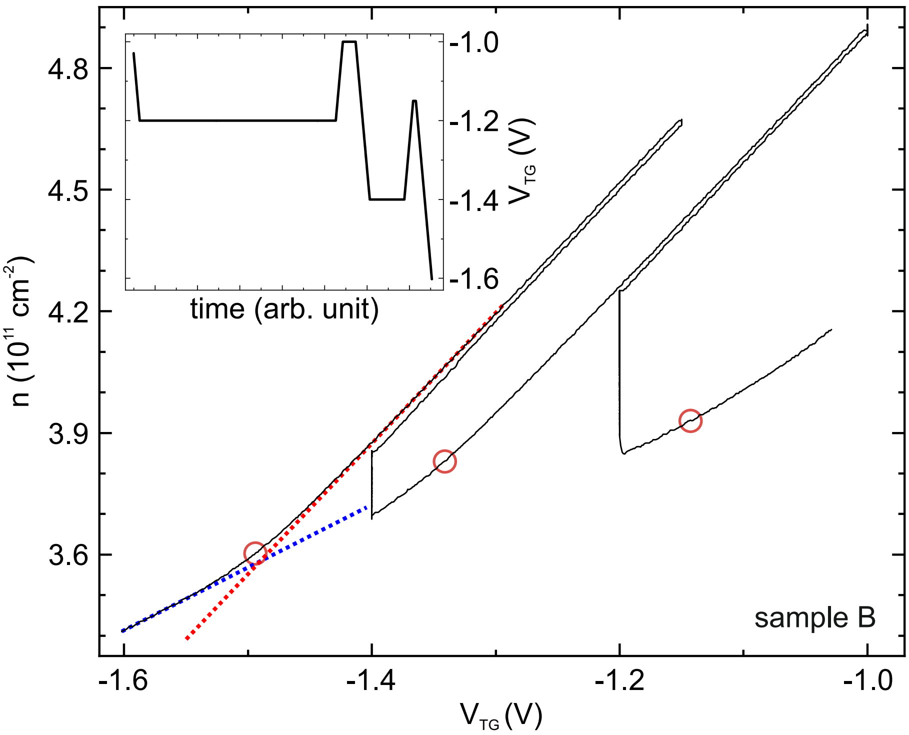

Fig. 5.11: *Electron density n of sample B at $V_{\mathrm{TG-BCd}} = -6$ V as a function of V_{TG} within regime VI, enlarged part of Fig. 5.10. At the point of the red circle, the slope transitions from a steeper one (red dotted line) to a smaller one (blue dotted line). The inset depicts the corresponding V_{TG} sweeps.*

5.4. Temperature dependence

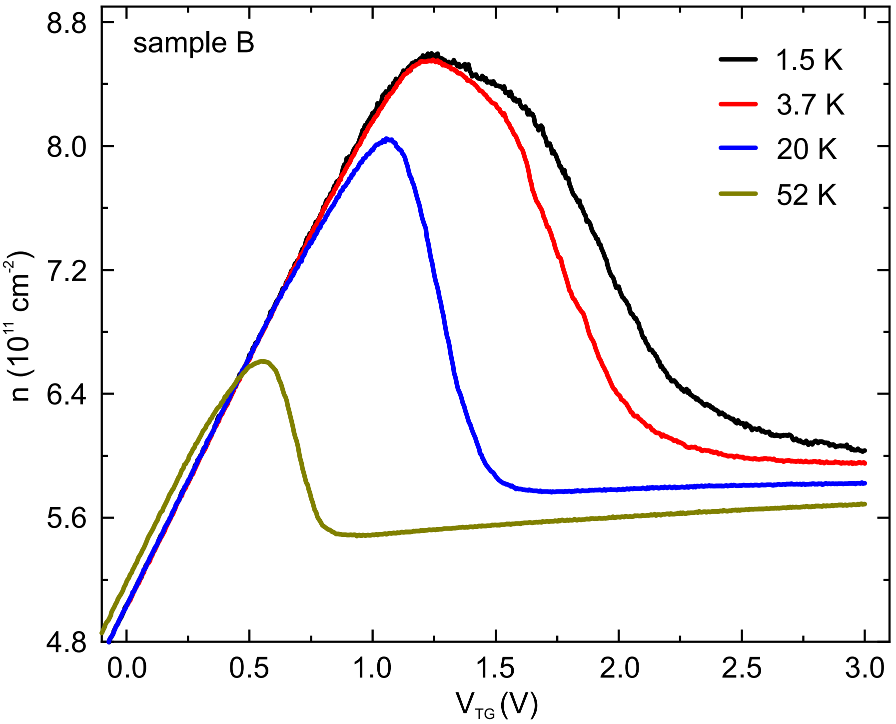

Fig. 5.12: *Electron density* n *of sample B at* $V_{\mathrm{TG-BCd}} = 0$ *V as a function of* V_{TG} *for four different temperatures. Starting in regime I, a* V_{TG} *upsweep covers regimes I to IV. By increasing the thermal energy, charge-transfer processes from the QW towards the interface are enhanced.*

In our understanding, the charge-transfer processes dominating the gating behavior in regimes II, III and IV are based on electron tunneling from the QW into the DDLs, and via them towards and into the interface. Hence, thermal energy should lead to an enhancement of these processes. Fig. 5.12 shows the temperature dependence of the gate response of sample B at $\mathrm{V_{TG-BCd}} = 0$ V for four different temperatures. The system is initialized in regime I, a $\mathrm{V_{TG}}$ upsweep then covers regimes I to IV. Between each measurement, the sample is brought to RT ensuring a fully reset system. When we take a look at the outcome of the temperature series, the temperature dependence exactly matches our picture discussed in Sec. 5.3: for the slightest thermal assistance, even from $T = 1.5$ K (black trace in Fig. 5.12) to $T = 3.7$ K (red trace), the peak narrows, i.e. the density decrease after the peak sets on earlier in terms of $\mathrm{V_{TG}}$, representing the transition from regime III to IV. This translates into a rather delicate enhancement of the multistep (hopping) tunneling from the QW via the InAlAs DDLs into the interface. Additionally we observe a reduction of the peak height, i.e. the onset of regime II. This can be traced back to a reduction of the triangular-shaped potential barrier between the QW and the DDLs in the InAlAs, leading to an increased tunneling probability of electrons out of the QW for increasing temperatures, clearly visible for $T = 20$ K (blue trace) and $T = 52$ K (olive trace).

5.5. Design parameters of the heterostructure

As our experiments and the accompanying discussions point out the importance of the intrinsically present DDLs in InAlAs on limitations of gate operations in the InAlAs-based heterostructures, they represent an important design parameter of such heterostructures regarding gated operation. Interestingly, the major impact of the DDLs has not been addressed in the literature. In this section, we discuss two examples of such design parameters, which, given the intrinsic nature of the DDLs, strongly determine the gate operation of the heterostructure: the indium concentration and the depth of the QW below the heterostructure surface.

5.5.1. Discussion of the indium concentration

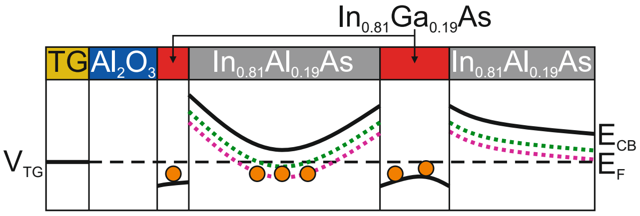

Fig. 5.13: *Conduction band (CB)-edge sketches of sample A (81% indium concentration) for* $V_{TG} = 0$ *V. Due to the increased indium concentration compared to sample B (75%), the DDLs lie below the Fermi energy already at* $V_{TG} = 0$ *V, resulting in an electrostatic situation similar to regime VI already at* $V_{TG} = 0$ *V.*

We begin with the discussion of the indium concentration in the active layers. As already outlined for Fig. 5.1 in Sec. 5.1, we have consistently observed strong limitations in the gate operation for heterostructures with 81% indium compared to ones with 75%. This can be explained within our model and be tracked down to the DDLs in the InAlAs. Fig. 5.13 depicts a schematic band-edge illustration of sample A (81% indium), which should be compared with Fig. 5.4(a) of sample B (75%). We assume here the energy difference between the DDLs (dotted colored lines) and the InAlAs CB edge to be independent of the indium concentration in the InAlAs. The band offsets between InAlAs, InGaAs and InAs however decrease with increasing indium concentration. As a result, the tunneling of electrons out of the QW into DDLs is enhanced (see Fig. 5.13) while it is forbidden for lower indium concentrations (see Fig. 5.4(a). This manifests itself directly in two observations which we have reported in our comparison of samples A and B with Fig. 5.1. First, the maximum accessible electron density as well as the saturation density are both smaller in sample A (higher indium concentration). These quantities represent the onset of regimes II and IV. The onset of multistep tunneling of electrons out of the QW into DDLs - and via them towards the interface - requires less gate action compared to a heterostructure with lower indium concentration. Due to this earlier onset of tunneling, the transition from regime I to regime II occurs for smaller V_{TG} (and thus smaller electron densities), hence the smaller maximum density for sample A (81%) compared to sample B (75%). The same is true for the transition from regime III to IV, resulting in the smaller saturation density

for sample A compared to sample B.
Second, as observed in Fig. 5.1(a), sample A is in an unstable electrostatic situation similar to regime VI directly after cooldown. This is the consequence of an electron population at the apex of the trough in the InAlAs as well as at the interface between the semiconductor and the dielectric already directly after cooldown at $V_{TG} = 0$ V, indicated by the orange dots in Fig. 5.13. The reduced band offsets due to the higher indium concentration promote this peculiar bandstructure already after cooldown. We have shown within the CTM, that sample A can be brought into an electrostatically stable regime I by applying a (large) negative V_{TG} in order to sufficiently depopulate trapped electron within DDLs and the interface. This has to be seen in comparison to sample B with smaller indium concentration, which offers negligible multistep tunneling at $V_{TG} = 0$ V (see Fig. 5.4(a) and is thus initialized in the electrostatically stable gating regime I.
We have shown in Fig. 5.2 a procedure to initialize (i.e. directly after cooldown) sample A in the stable gating regime I by applying a negative biased cooldown voltage V_{TG-BCd} at RT (see orange and green traces in Fig. 5.2). Fully compatible with our CTM, this large negative topgate voltage applied at RT enables an efficient depopulation of electrons trapped in DDLs and the interface, allowing stable gate operation in regime I right after cooldown. Additionally, as a direct consequence of this depopulation, the biased cooldown brings the advantage of accessing higher maximum electron density compared to a zero-biased cooldown, as seen from a comparison of the orange and black traces in Fig. 5.2.

The CTM also covers differences observed in experiments with indium concentrations below 75%. A sample C, structurally similar to samples A and B, has 65% indium concentration. This sample C should, according to the CTM, lead to significantly higher maximum accessible electron density as well as higher saturation density compared to sample B (75%). At the same time, the initialization should still lie within the stable regime I, similar to sample B. Indeed, the corresponding gate response of sample C for $V_{TG-BCd} = 0\,\text{V}$ at $T = 4.2\,\text{K}$ in Fig. 5.14 verifies our predition experimentally. After the cooldown, a V_{TG} downsweep (red trace) and the subsequent upsweep coincide precisely. Also, no equilibration time for the density to settle is required. Both observations characterize a stable gating regime I. At $V_{TG} = 1.85$ V, the density begins to saturate, indicating the onset of regime II. Going further from thereon however was not feasible for this particular sample, as the dielectric was leaking for $V_{TG} > 2.1$ V. Note that a short waiting time at $V_{TG} = 2.0$ V reveals a loss of electrons although V_{TG} is kept constant. A subsequent downsweep opens up a small hysteresis. We have shown both these observations to result from the occurrence of a charge transfer (see Fig. 5.5).

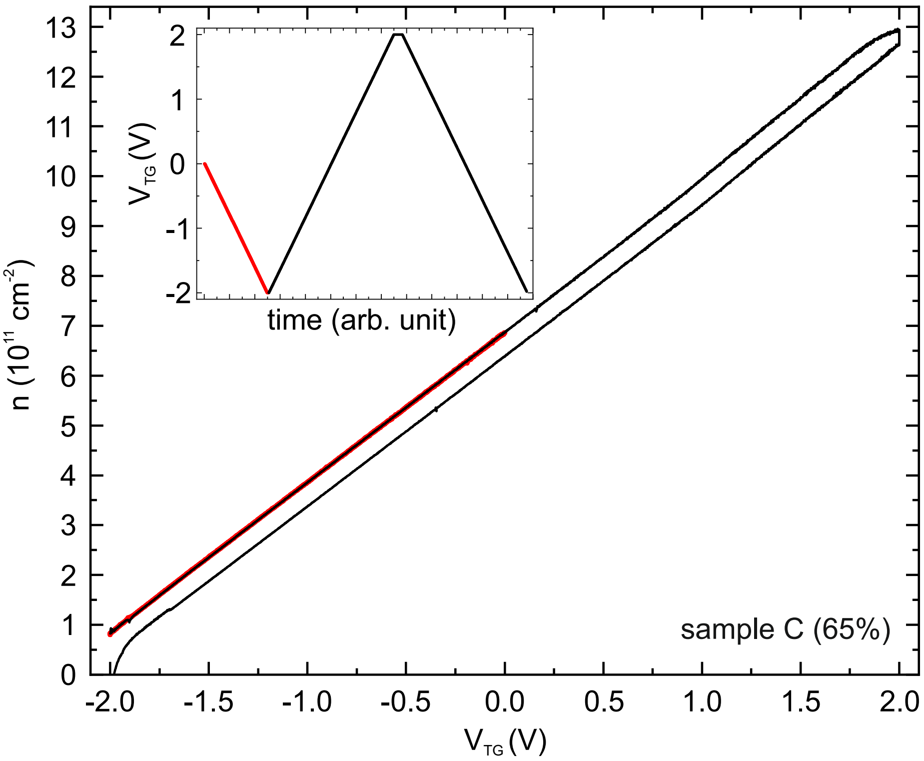

Fig. 5.14: *Electron density* n *of sample C (*65% *indium concentration) at* $V_{\mathrm{TG-BCd}} = 0$ *V as a function of* V_{TG}*. Initialized in regime I, the maximum electron density is increased significantly due the lower indium concentration. The inset depicts the corresponding* V_{TG} *sweeps.*

In order to overcome the leakage problem for this sample and thus to get a further insight into the gate cycle, sample C was cooled down with bias $\mathrm{V_{TG-BCd}} = -6$ V. With this, we are able to exploit the $\mathrm{V_{TG}}$ range from -6 V up to the limit $+2$ V. The corresponding gate response is displayed in Fig. 5.15, where a downsweep below the MIT (red trace) and a subsequent upsweep coincide similar to the situation for $\mathrm{V_{TG-BCd}} = 0$ V (see Fig. 5.15), indicating the initialization again in regime I. For $\mathrm{V_{TG}} > -4$ V, the density begins to saturate: the onset of regime II. Going further however reveals, that the density does not drop from a certain $\mathrm{V_{TG}}$, as expected for the onset of regime III. Over the whole voltage range up to $\mathrm{V_{TG}} = +2$ V, the density stays constant although $\mathrm{V_{TG}}$ is increased. This would suggest rather regime IV or V. A subsequent downsweep at $\mathrm{V_{TG}} = +2$ V leads to an instant decrease of the density, indicating that the capacitive coupling is not lost, thus exlcuding regime V for this situation. During the final downsweep, the adjustment of the density according to $\mathrm{V_{TG}}$ requires a settling time, similar to regime VI. This experiment suggests that this sample C with 65% indium concentration transitions from the linear regime I directly into a regime similar to regime IV and with a downsweep in regime VI. The missing of regimes II and III can be explained when we consider the CB profile of this heterostructure in hindsight to the trend for 75% and 81% (see Figs. 5.4a and 5.13): For the previous discussion of the indium concentration we have assumed that the energetic distance of the DDLs from the InAlAs CB is constant. For higher indium concentration, the band-offsets between InAlAs, InGaAs and InAs decrease, leading to enhanced multistep tunneling and the effects on the CTM described previously. For lower indium contents, here 65%, the band-offsets increase compared to 75%. Hence, even at V_{TG} = 0 V the DDLs and thus also the apex of the trough in the InAlAs lie energetically significantly higher than the first subband of the QW and the Fermi energy compared to the situation in sample B 75% (see Fig. 5.4(a). As a consequence, by increasing V_{TG}, significantly higher voltages are required to enable tunneling out of the QW into the DDLs (onset of regime II). Even higher voltages are needed to get a more transparent triangular-shaped potential barrier to induce the significant loss of electrons (regime III).

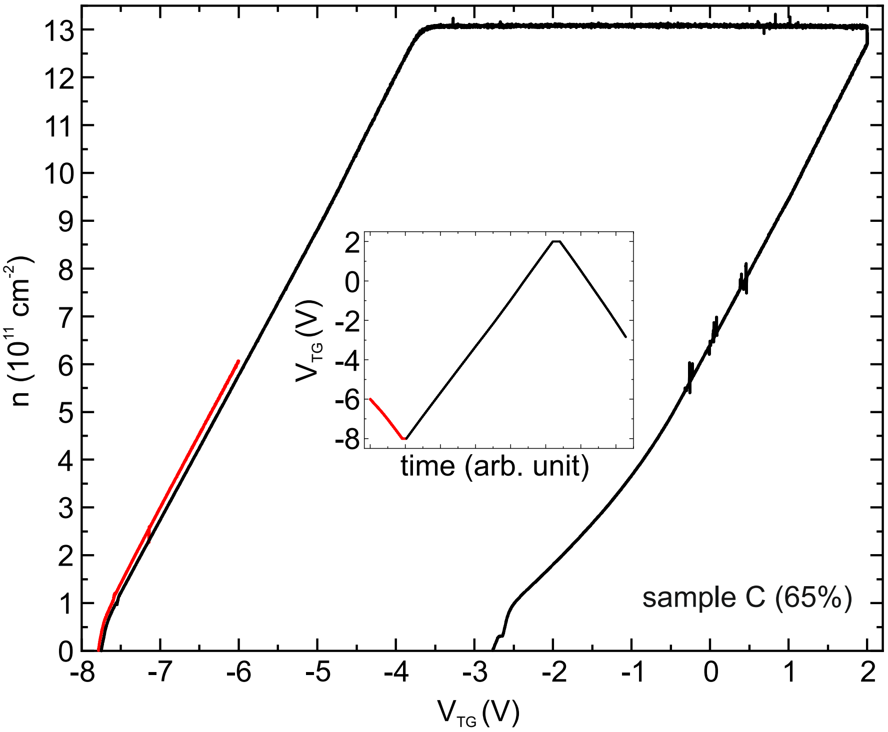

Fig. 5.15: *Electron density n of sample C (65% indium concentration) at* $V_{TG-BCd} = -6$ *V as a function of* V_{TG}. *The negative biased-cooldown allows a further* V_{TG} *sweep in positive direction compared to the* $V_{TG-BCd} = 0$ *V configuration. The density saturation for* $V_{TG} > -4$ *V stays constant for up to* $V_{TG} = +2$ *V, where a subsequent downsweep displays instant reaction of the density. The inset depicts the corresponding* V_{TG} *sweeps.*

Simultaneously, due to the band bending (before electrons can tunnel out of the QW into the DDLs), the apex of the trough in the InAlAs is shifted towards the interface. Due to the higher gate voltages needed to enable tunneling, these processes occur more simultaneously compared to the rather successive sequence of both in heterostructures with higher indium concentration, the transfer of electrons into DDLs (regimes II and III) is almost instantly followed by the efficient transfer into the interface (regime III to IV).

Hence, once the electron tunneling into DDLs begins, they are immediately transferred into the interface. This is in contrast to heterostructures with higher indium concentration, where electrons tunnel into DDLs from which they are transferred into the interface not until $\mathrm{V_{TG}}$ is increased further.
The transfer marks the onset of the density saturation, experimentally observed in Figs. 5.14 and 5.15. As these electrons significantly populate the interface, partial screening of the TG electric field is enabled, leading to the same effects described for regime IV, where each adjustment of $\mathrm{V_{TG}}$ is counteracted by transfer of electrons and thus a screening. The instant reaction of the density by a downsweep performed within this saturation, indicates that the screening is only partial. As we are not able to go any further than $\mathrm{V_{TG}} > +2$ V for this sample, we cannot answer the question whether a regime V with full screening can be obtained. The downsweep started at $\mathrm{V_{TG}} = +2$ V is a clear regime V, however not as pronounced as in samples A and B, i.e. settling times are on smaller scales and the slope of this branch is almost as steep as the slope in regime I. The lower indium concentration results in less electrons trapped in DDLs sites compared to higher indium concentration. As a consequence, the interface hosts comparatively more electrons. Since we attribute the electrons trapped in DDLs sites to dominantly cause the re-transfer during regime VI, it is consistent for heterostructures with lower indium concentration to exhibit a less pronounced re-transfer.

5.5.2. Reducing the QW depth

To discuss the influence of a reduced depth of the QW with regard to the heterostructure surface on the gate response, we present the gate response of sample D in Fig. 5.16. Sample D is a heterostructure with 75% indium concentrationwith only 50 nm InAlAs barrier between the QW and the heterostructure surface (instead of 130 nm in previous heterostructures). Note that the QW additionally includes an asymmetrically-placed InAs layer, resulting in a 19 nm wide two-step QW compared to the 20 nm wide single-step InGaAs QW from the previously discussed samples A, B and C. The gate response in Fig. 5.16 was obtained with a biased-cooldown at $\mathrm{V_{TG-BCd}} = -5$ V because the dielectric was leaking for $\mathrm{V_{TG}} > +0.6$ V. Due to the biased-cooldown here, the sample is already below MIT right after cooldown. The gate cycle thus begins with a $\mathrm{V_{TG}}$ upsweep and the first measurement point is at $\mathrm{V_{TG}} = -5.6$ V. In this upsweep up to $\mathrm{V_{TG}} = -3.8$ V, the density increases linearly with $\mathrm{V_{TG}}$ without the requirement of a settling time, indicating regime I. Above $\mathrm{V_{TG}} > -3.8$ V, the density begins to saturate and remains constant although $\mathrm{V_{TG}}$ is increased up to +0.5 V. A subsequent downsweep leads to an instant decrease of the density, opening up a hysteresis. The MIT occurs already at $\mathrm{V_{TG}} < -3$ V. Note, that the slope of the downsweep is slightly smaller than the the slope in regime I and also note, that within the saturation as well as during the downsweep, the density requires a settling time to reach its equilibrium value after each adjustment of $\mathrm{V_{TG}}$. This suggests, that the sample is in regime IV in the saturation and in regime VI during the downsweep. Most interestingly, this gate response for sample D looks almost identical to the one of sample C, a structure with only 65% indium but 130 nm InAlAs barrier (see Fig. 5.15).
Now the question arises, why samples D and C exhibit similar behavior although they are significantly different from each other. For this, we take a look at the CB edge profile

of sample D (for visualization purposes the QW is sketched as a single-step QW) in Fig. 5.17(a), representing a configuration for $V_{TG} = 0$ V, which should be compared to Fig. 5.4(a) of sample B (which also has 75% indium). Due to the reduced InAlAs thickness between the QW and the interface (from 130 nm to 50 nm), the trough in the InAlAs caused by the DDLs is significantly weaker.

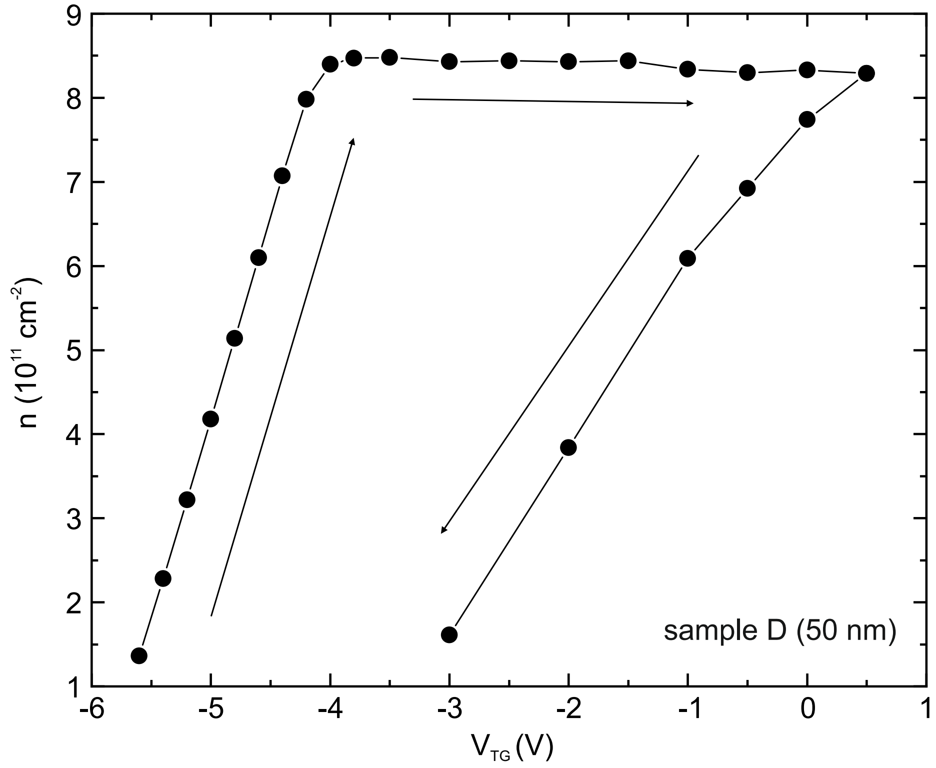

Fig. 5.16: *Electron density n as a function of V_{TG} of a sample D with only 50 nm InAlAs barrier to the surface and 75% indium concentration at $V_{TG-BCd} = -5$ V. Similar to sample C (130 nm barrier but 65%), the gate response offers a regime I right after cooldown which transitions directly into a saturation regime IV, subsequently followed by regime VI.*

With a positive V_{TG} applied, depicted in Fig. 5.17(b), tunneling of electrons out of the QW and into DDLs is enabled. Due to the reduced InAlAs thickness, the trough in the InAlAs is not as pronounced as in heterostructures with thicker InAlAs. Hence, the electrons are directly transferred into the interface. Here, they can be trapped robustly and cause a partial screening. This creates the observed density saturation in Fig. 5.16. This behavior is similar to regime IV (see Sec. 5.3.5) and interestingly identical to the interpretation of the experiments with sample C (65% indium). The discussed gate response behavior for heterostructures with 50 nm InAlAs barriers compared to 130 nm does also comply with the discussion of the higher indium concentration (see Sec. 5.5.1). Indeed, experiments with samples of similar heterostructure layout as sample D, but with 81% indium, exhibit gate responses, which are expected by the CTM: Due to the smaller band offsets, these samples offer a smaller maximum electron density and, depending on the

exact heterostructure layout, a initialization outside of regime I right after cooldown while the overall gate cycle contains only regimes I, IV and VI.
A more detailed view and discussion of the indium concentration as well as further experiments can be found in the master thesis by J. Schmidt [83].

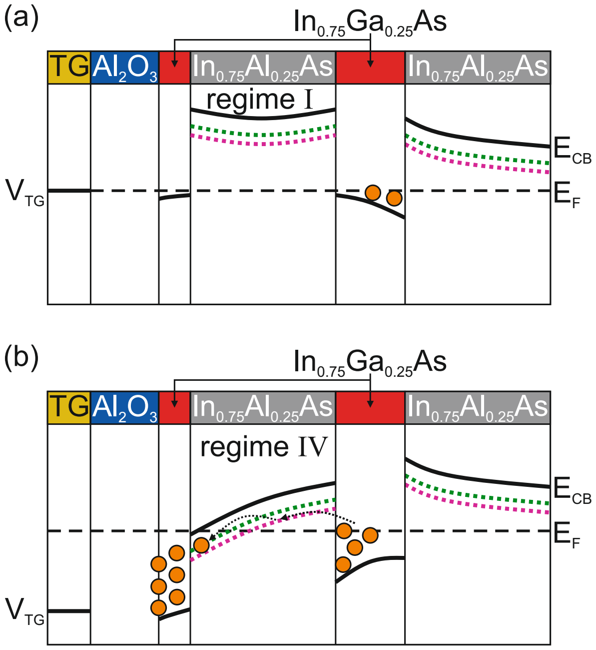

Fig. 5.17: *CB-edge sketches of sample D (75% indium and only 50 nm InAlAs barrier) for* $V_{\mathrm{TG}} = 0$ *V (a) and* $V_{\mathrm{TG}} >> 0$ *V (b). Due to the reduced InAlAs thickness, the trough caused by the DDLs in the InAlAs is not as pronounced. Thus, a large positive* V_{TG} *results in electron tunneling via the DDLs directly into the interface, skipping regimes II and III.*

5.6. Conclusion

In conclusion, we are able to identify the deep donor levels induced by defects intrinsically present in InAlAs to be a crucial factor in the design process of indium-based QWs embedded in InAlAs for indium concentrations between 65% and 81%, e.g. for spin-orbitronic applications. Although these intrinsic defects provide a native n-type doping to leverage the spin-orbit interaction in 2DESs in such heterostructures, they substantially determine the electrostatics of the heterostructure due to charge trapping and unintentional tunneling. They thus impose limitations on the gate operations in such heterostructures and as a consequence, a stable and linear gate operation is only feasible in a limited gate-voltage range. The most part of the voltage range then is characterized by a reduced-to-vanishing capacitive coupling of the topgate to the 2DES induced by unstable or metastable electrostatic configurations caused by charge-transfer processes on rather long time scales. Our study shows that the design of the heterostructure govern the electrostatic configuration of the system. Most importantly, the indium concentration crucially impacts in which electrostatic configuration (i.e. regime I or VI) a sample is initialized right after cooldown. By reducing the distance of the QW to the heterostructure surface, gate operation limitations can be enhanced. Our model also allows us to qualitatively predict how these InAlAs-based heterostructures will react to gate operations. It also provides methods to reach the stable gating regime I during a gate cycle and explains the observed favorable action of negative biased cooling to initialize a sample already in regime I right

after cooldown.
From these findings here and our very general experimental experience across many samples with different heterostructures, the presence of these deep donor levels in the InAlAs should be accounted for in the design of heterostructures, especially for spin-orbitronics. Although maximizing the spin-orbit interaction through an increase of the indium concentration also enhances strongly the electron mobility (see Sec. 4.1), it will at the same time minimize the accessible electron density as well as limit stable gate operation intervals.

6. Spin-orbit interaction in InAs/InGaAs QWs

We have presented in Sec. 2.3.2 the structure of the Rashba parameter α as a composition of a contribution from the distribution of the electric field in the QW, α_{el}, and from the overlap of the electron wavefunction probability density with material interfaces within the QW, α_{int}. To our knowledge there is no systematic study in the literature which specifically tunes the interface contribution α_{int} by selective placing and setting of interfaces in InAs/InGaAs/InAlAs-based QWs with 75% indium concentration. This is where we set our focus in this chapter.

A challenge here is the fact, that we quantify the total α via analysis of beating patterns in longitudinal magnetotransport of the sample while a separation into the two contributions α_{el} and α_{int} is experimentally not feasible. But utilizing simulations of the bandstructure and the wavefunction (via a self-consistent Poisson-Schrödinger solver), enables us to quantify the two contributions separately. However, α_{el} is a representation of the electrostatics within the sample and from our findings on the peculiarities of gate operation in InAlAs-based samples (see Sec. 5), the electrostatics in these heterostructures are not trivial. Thus, a quantitative prediction of α_{el} purely from the simulation has to be considered with caution. A strong deviation of α values based on simulations (similar to our theoretical approach) and experimentally determined values was reported by Trottmann [67], where simulations yielded values more than ten times smaller than those from experiments. All this motivated our experimental approach on the interface contribution to the Rashba SOI, where we utilize the simulations as a qualitative support for the interpretation of the experimental findings.

6.1. (A)symmetrical two-step InAs/InGaAs QWs

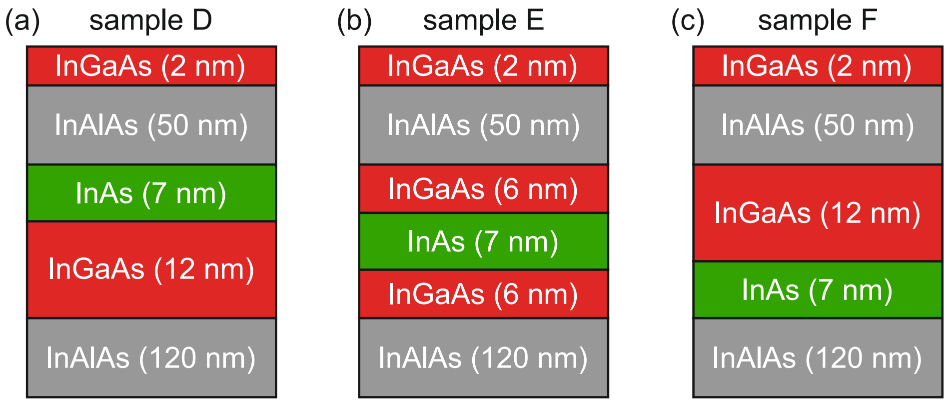

Fig. 6.1: *Heterostructure layout of samples D (a), E (b) and F (c), where a* 7 *nm wide InAs inset (green) is placed within a (in total)* 12 *nm wide InGaAs QW in three different positions. The QW is embedded in* 50 *nm InAlAs and the indium concentration in the active layers is set to* 75%.

As a simple approach for the tuning of the interface contribution α_{int}, we first consider the overlap of the electron wavefunction probability density with the interfaces in a QW.

For this, we use a two-step QW design embedded in InAlAs, comprising InGaAs with an InAs inset, which is placed either asymmetrically on one side of the QW or symmetrically within the QW. This allows us to study the influence of the asymmetry within the InGaAs, i.e. the overlap on different interfaces. Due to the complexity of the total α and the contribution of the electrostatics via α_{el}, we add a third structure to the study, which has the inset asymmetrically on the opposite side. This set of three heterostructure samples is presented in Fig. 6.1: samples D (a), E (b) and F (c). The complete width of the QW was kept constant at 19 nm, in which a 7 nm InAs inset was placed on either side of the QW or in the center. The depth of the QW embedded in InAlAs is 50 nm and capped to the surface with 2 nm InGaAs. The indium concentration in the active layers is set to 75%. This allows for one a large topgate voltage range, in which we observe a linear gating regime I, i.e. a large electron density range, while for another maintaining an initialization after cooldown in this regime I and high electron mobility.[7]

All three samples were analyzed by magnetotransport measurements at a temperature of $T = 1.7$ K. The samples were cooled down at $\mathrm{V_{TG-BCd}} = 0$ V, a $\mathrm{V_{TG}}$ downsweep was applied to the system below metal-insulator-transition (MIT) and a subsequent $\mathrm{V_{TG}}$ upsweep was then used for the characterization. This ensures a gate operation in the linear gating regime I. The electron densities extracted by the slope of the Hall resistivity ρ_{xy} and by analysis of Shubnikov-de Haas (SdH) oscillations in the longitudinal resistivity ρ_{xx} are in good agreement in all samples. The minima in the SdH oscillations reach $\rho_{xx} = 0\ \Omega$ while ρ_{xy} exhibits a linear shape, validating a well-defined 2DES.

6.1.1. Measurement of α_{exp}

We extract the strength of Rashba-type SOI α_{exp} by analyzing the beating pattern in ρ_{xx} (see Sec. 2.3.3 with Eq. 2.50 and Sec. 3.3.2). The determined values from the experiment α_{exp} can then be compared to those extracted from the simulations of these structures (see Sec. 2.3.2 with Eq. 2.45), which we denote as α_{sim}. The calculation of α_{sim} is based on input parameters from bandstructure simulations. These latter simulations were performed as follows: A match of the simulated electron density with the experiment was achieved by adjusting the Fermi level pinning (FLP) on the semiconductor surface (without dielectric and metallic topgate) in the simulation [8]. This approach is used similarly in [53] and [84] and is justified by the fact that for both, gated structures and ones without topgate, the corresponding Dirichlet boundary value problem is defined via the energetic barrier height of a Schottky-type contact at the heterostructure surface. Thus both the interface either from semiconductor to air as well as semiconductor to a dielectric is approximated like a semiconductor-metal-interface, and thus by the height of the Schottky barrier.

Fig. 6.2(a) shows the electron density of sample D (InAs inset towards surface, see Fig. 6.1(a) as a function of $\mathrm{V_{TG}}$. SOI-induced beating due to spin-splitting occurred in the

---

[7] Although 81% indium would lead to higher SOI and higher electron mobility, the available maximum electron density would be considerably smaller and there would be a reasonable risk to initialize the sample in regime VI. With 65% indium however, the maximum density, linear regime I and initialization would be even enhanced compared to 75%, but electron mobility and SOI would be significantly smaller.

[8] A simulation structure with a dielectric and metallic topgate (like the real sample) yielded different capacitive coupling constants while also not matching the experimentally observed gate response.

V_{TG} range -0.4 V to $+0.2$ V (indicated by the red points n_{FFT}). The two density values n_{FFT} for each V_{TG} represent each spin-branch (up and down) with the average value for negative and positive magnetic fields. Adding up the two densities n_{FFT} yields n_{Hall}.

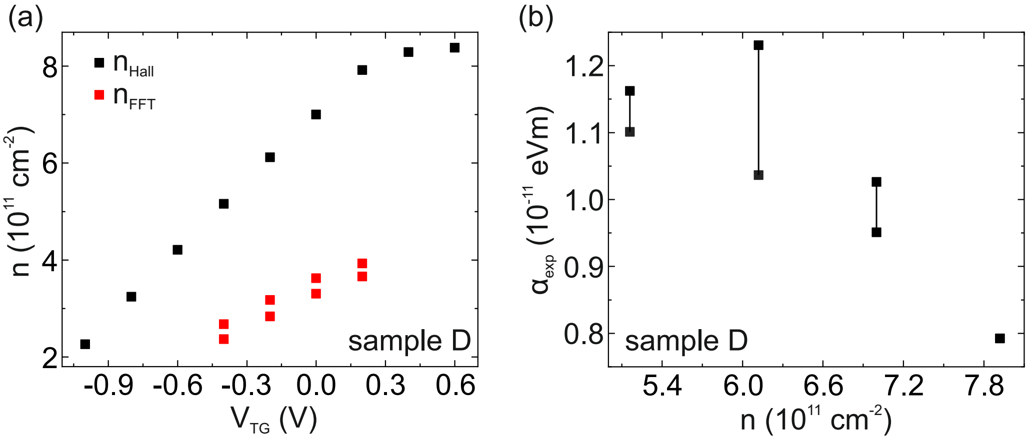

Fig. 6.2: *(a) Electron density* n *as a function of* V_{TG} *(upsweep) of sample D at* $V_{\mathrm{TG-BCd}} = 0V$. *For some* V_{TG} *values, SOI-induced beating patterns occurred in* ρ_{xx}*, for which the red dots represent the average density* n_{FFT} *of each spin branch extracted with FFT each from positive and negative magnetic field. (b) Rashba parameter* α_{exp} *as a function of electron density* n *extracted from the FFT density analysis of the SOI induced beating patterns for positive and negative magnetic field.*

The corresponding experimentally extracted values for the Rashba parameter α_{exp} are displayed as function of the electron density in Fig. 6.2(b), extracted for both positive and negative magnetic fields. With increasing density, α_{exp} decreases (linearly) from $\alpha_{exp} = 1.23 \times 10^{-11}$ eVm to $\alpha_{exp} = 0.79 \times 10^{-11}$ eVm. In contrast to this sample D, sample E with the InAs inset symmetrically placed within the InGaAs (see Fig. 6.1(b) does not show any signs of SOI-induced beating in ρ_{xx}, suggesting that α_{exp} is significantly smaller compared to sample D. This will be discussed separately at the end of this section. When we take a look at the gate response of sample F, which has the inset asymmetrically within the InGaAs but compared to sample D towards the substrate (see Fig. 6.1(c), SOI-induced beating patterns occurred again. For sample F, displayed in Fig. 6.3(a), the beating was visible for a larger density range ($n = 4 - 10 \times 10^{11}$ cm^{-2}) compared to sample D ($n = 5 - 8 \times 10^{11}$ cm^{-2}), but with a gap at $n = 6 - 7 \times 10^{11}$ cm^{-2}, where we observed no beating. Similar to sample D, sample F shows a decreasing α_{exp} for increasing electron density in Fig. 6.3(b), the observed values are also similar to sample D in the range $\alpha_{exp} = 1.17 \times 10^{-11}$ eVm to $\alpha_{exp} = 0.68 \times 10^{-11}$ eVm.

Concluding on these three heterostructures, we find that α_{exp} for the two asymmetric samples D and F is larger compared to the symmetric sample E. Both asymmetric samples D and F are similar regarding the SOI. The maximum values for α_{exp} from samples D and F meet the values reported in the majority of reports in the literature, also extracted from beating patterns [10, 26, 51, 53, 84–90]. Also, these reports also observe a decreasing α with increasing density, like we do. Note that, there are a few reports [9, 91, 92] which observe an increase of α with increasing electron density. Interestingly, these articles at the same time report significantly larger α values ($\alpha_{exp} = 3 - 7 \times 10^{-11}$ eVm) than the rest of the literature. This suggests, that they obtained these values in gate regimes outside the linear gating regime I (see Sec. 6.1.3).

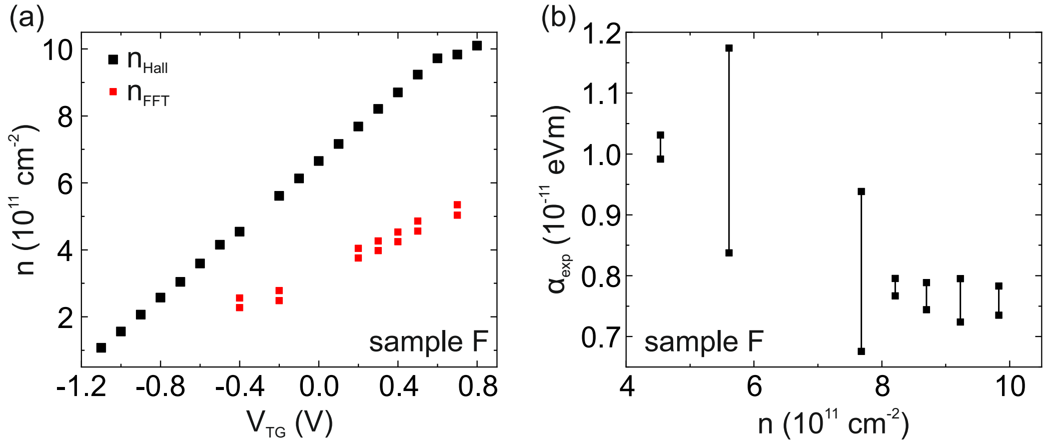

Fig. 6.3: *(a) Electron density n as a function of V_{TG} (upsweep) of sample F at $V_{\mathrm{TG-BCd}} = 0V$. For some V_{TG} values SOI-induced beating patterns occurred in ρ_{xx}, for which the red dots represent the average density n_{FFT} of each spin branch extracted with FFT each from positive and negative magnetic field. (b) Rashba parameter α_{exp} as a function of electron density n extracted from the FFT density analysis of the SOI induced beating patterns for positive and negative magnetic field.*

6.1.2. Separation of the Rashba parameter

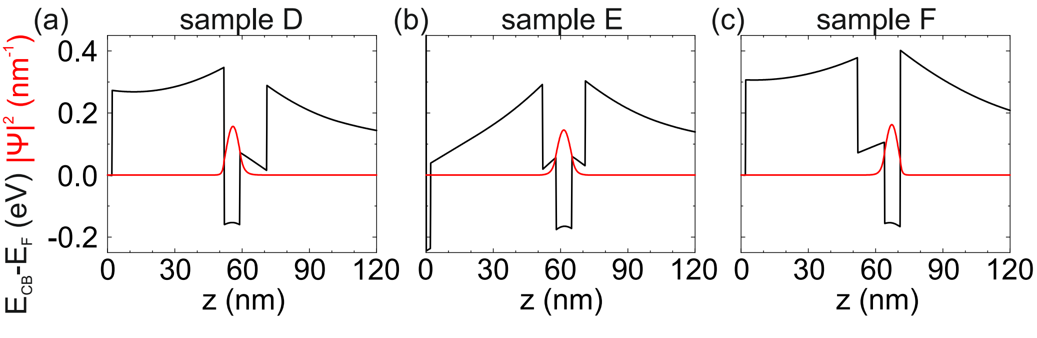

Fig. 6.4: *Conduction band (CB) edge $E_{CB} - E_F$ (black trace) and wavefunction probability density $|\Psi|^2$ (red trace) as a function of distance z from the semiconductor surface for samples D (a), E (b) and F (c). The calculations were performed for $T = 1.7$ K and $V_{\mathrm{TG}} = 0$ V.*

A breakdown of the total α into only α_{el} and α_{int} turned out to be too simple for the interpretation of the observed experimental results. Hence, we focus on a more detailed look into the interface contribution α_{int}. For a simple approach we link α_{int} with the amount of the overlap of the wavefunction probability density $|\Psi|^2$ and the adjacent interfaces within the QW. Fig. 6.4 shows the conduction band (CB) edge (black trace) together with the wavefunction probability density $|\Psi|^2$ (red trace) at $\mathrm{V_{TG}} = 0$ V for each sample D (a), E (b) and F (c), based on the bandstructure simulations. z denotes the inverse growth direction, i.e. from the semiconductor surface towards the substrate ($z = 0$ thus represents the semiconductor surface). For all three heterostructures, $|\Psi|^2$ has its maximum centered in the InAs inset with a similarly sharp decrease to both adjacent interfaces. Despite a InAlAs/InAs and a InGaAs/InAs interface in samples D and F compared to two InGaAs/InAs interfaces in sample E, the overlap of $|\Psi|^2$ with these interfaces is similar across the three heterostructures. Indeed, this is confirmed when the contribution from each individual interface within the QW is considered separately. For this, we use the expression for α_{int} (Eq. 2.45 in Sec. 2.3.2)

$$\alpha_{int} \propto \sum_n S_n \cdot A_{int} \cdot |\Psi(z_n)|^2. \tag{6.1}$$

S_n represents the sign of the contribution from each interface n within the QW.

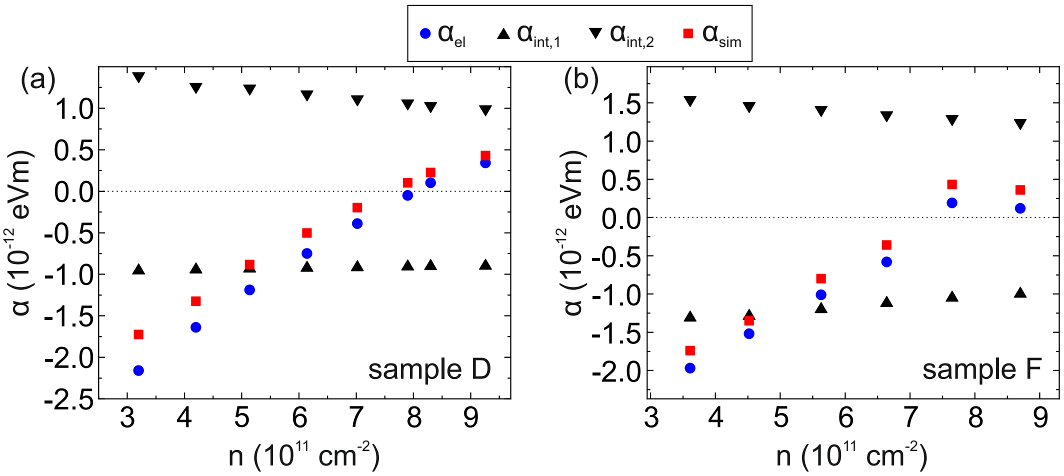

Fig. 6.5: *Calculation of the Rashba parameter for samples D (a) and F (b). The total value based on the simulations is denoted as α_{sim} (red), with contributions from the electric field α_{el} (blue) and the interfaces $\alpha_{int,n}$ (black) within the QW, i.e. InAs/InGaAs and InAs/InAlAs.*

Schäpers *et al.* [51] and Kunihashi *et al.* [93] reported, how the relation between the exact interface array (i.e. the bandgap relations of the interface materials) defines S_n. The direction z from which the interfaces are counted is inverse to the growth direction, i.e. starting from the heterostructure surface ($z = 0$) in direction towards the substrate. If the material with the higher bandgap is on the side with the larger z (towards substrate), $S_n = +1$ and -1 otherwise. In all three heterostructures, the InGaAs/InAlAs interface within the QW is negligible due to a vanishing $|\Psi|^2$ at the interface. Thus, the remaining interfaces in the QW add up with differing signs. In Fig. 6.5 we calculated and plotted the interface contribution $\alpha_{int,n}$ (black triangles) exemplarily for samples D (a) and F (b) while also calculating α_{el} (blue dots) as a function of the electron density n. The total amount of this simulation-based Rashba parameter is denoted α_{sim} (red squares).[9] For both heterostructures, the interface contributions $\alpha_{int,n}$ cancel each other out, while α_{el} decreases with increasing density. Thus, α_{sim} is dominated by α_{el} and matches the experimental observed α_{exp} for both heterostructures (see Fig. 6.2(b) and 6.3(b)). This behavior was found to be similar in the simulations for sample E, resulting in a situation where the interface contribution from all three samples D, E and F is identical while the total Rashba parameter α is dominated by the electric field contribution α_{el}.

6.1.3. Manipulating the Rashba parameter via charge transfer

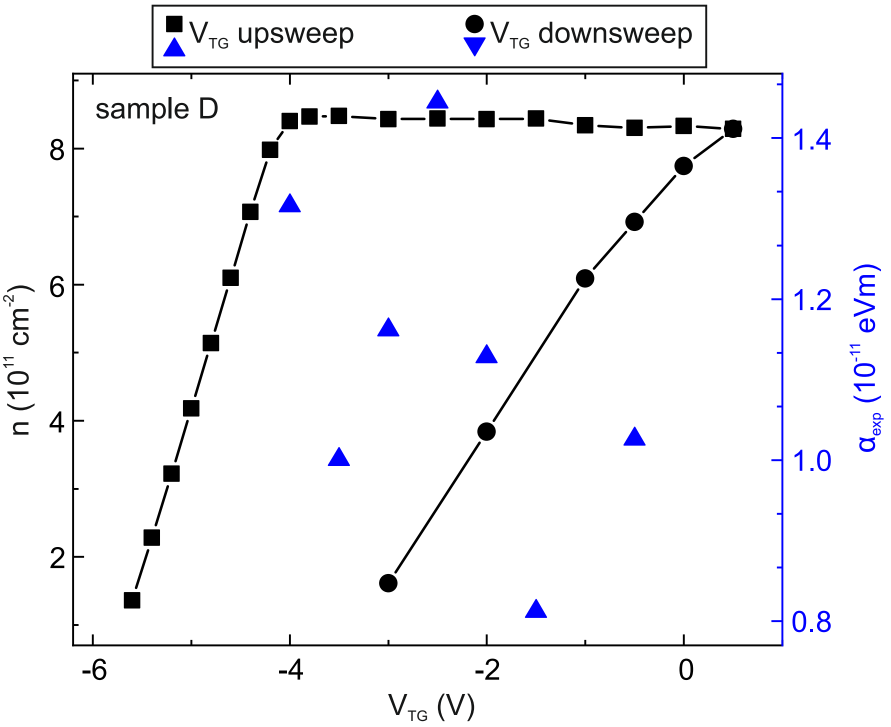

Fig. 6.6: *Electron density n of sample D as a function of V_{TG} at $T = 1.7$ K and $V_{\mathrm{TG-BCd}} = -5$ V. In the linear regime I, no SOI-induced beating is observed. With the onset of regime IV, i.e. charge transfer, beating patterns occur and α_{exp} (blue) can be extracted.*

As the experiments and the simulations suggest that α_{el} dominates α in these heterostructures, we utilize our findings from the charge transfer model and the influence

---

[9] Note, that the order of magnitude is more than ten times smaller compared to experimentally determined values. As mentioned before, this was also reported by Trottmann [67]. Although the values do not match the experiments, trends can still be extracted from the simulations. This highlights the complexity of the calculation of α for the given structures. Further improvements of the simulations is under ongoing investigation.

of DDLs in the InAlAs on the electrostatics in such heterostructures (see Sec. 5.3). By using a biased-cooldown procedure with $\mathrm{V_{TG-BCd}} < 0$ V, we specifically reduce charged traps and DDLs between the topgate and the QW (see Sec. 5.2) and thus manipulate the electrostatics within the sample, i.e. α_{el}. We performed a biased-cooldown on sample D with $\mathrm{V_{TG-BCd}} = -5$ V, for which the corresponding gate response is depicted in Fig. 6.6. After the cooldown, a $\mathrm{V_{TG}}$ downsweep depleted the 2DES below MIT, from which a subsequent $\mathrm{V_{TG}}$ upsweep (black squares) begins in regime I. Over the whole gating regime I, no SOI-induced beating patterns are observed. This is contrary to the configuration with $\mathrm{V_{TG-BCd}} = 0$ V, where beatings were visible over a large range of regime I (see Fig. 6.2). While this only suggests, that α_{exp} is now smaller compared to the unbiased situation, proceeding the $\mathrm{V_{TG}}$ upsweep further confirms our prediction: At $\mathrm{V_{TG}} = -4$ V, the system transitions from regime I into regime IV, marked by the saturation of the density. From here on beating patterns occur. Hence we extract α_{exp}, plotted as blue triangles in Fig. 6.6 as a function of $\mathrm{V_{TG}}$. This suggests, that the onset of a charge transfer, characterizing regime IV, strongly influences the electrostatics in the heterostructure which then directly enhances α_{el} and, as a result, beating patterns occur. Quite similarly to the findings here, Trottmann [67] also reported the occurrence of beating patterns with rather high α_{exp} values only in gating regime III, for heterostructures with deeper buried QWs (132.5 nm comared to 52 nm here). The extracted amount of α_{exp} from the beating in our experiments yields $\alpha_{exp} = 0.81 - 1.44 \times 10^{-11}$ eVm. This is, with its maximum only slightly higher, in the same order of magnitude compared to the unbiased configuration in regime I. Note the wide spread α_{exp} within regime IV, which we relate to significant charge fluctuation within the heterostructure during the charge transfer. Concluding the gate cycle with a subsequent $\mathrm{V_{TG}}$ downsweep starting from $\mathrm{V_{TG}} = +0.5$ V (black dots), representing regime VI, beating patterns vanished again. This suggests a decreased α_{el} due to the re-transfer of previously trapped electrons into the QW (cf. Sec. 5.3).

Similarly, the symmetrical sample E is investigated under a biased-cooldown. The corresponding measurement with $\mathrm{V_{TG-BCd}} = -6$ V is depcited in Fig. 6.7. With the onset of gating regime IV, sample E exhibits SOI-induced beating patterns, yielding $\alpha_{exp} = 0.52 - 1.61 \times 10^{-11}$ eVm (blue upwards triangles in Fig. 6.7). Over the course of regime IV, α_{exp} decreases with increasing $\mathrm{V_{TG}}$. We assign this to a reducing charge transfer in the ongoing regime IV: while $\mathrm{V_{TG}}$ is increased during regime IV, the partial screening transitions successively into a full screening, ultimately decreasing the charge transfer. In the subsequent downsweep starting from $\mathrm{V_{TG}} = -3$ V, representing regime VI, beating patterns are still visible. The corresponding extracted α_{exp} (blue downside triangles in Fig. 6.7) increase with decreasing density, matching the trend reported for samples D and F.

Compared to sample D, the range of sample E is in the same order of magnitude. At the same time, the maximum value is higher and compared to all samples up to here, the highest. Interestingly, Trottmann [67] reported values up to $\alpha = 3.0 \times 10^{-11}$ eVm in similar gating regimes. As mentioned before, some reports in the literature [9, 91, 92] observe similarly high α. Unfortunately, these articles do not show the electron density as a function of the gate voltage. Our and Trottmann´s [67] experimental results, seem to indicate that such unusually high Rashba parameters α may have been determined in gate structures initialized in a metastable electrostatic regime, i.e. outside regime I in our nomenclature. Hence, such values include strong and dominating electrostatic contributions to the SOI which result from the impact of DDLs on gated heterostructures. Given the metastability, such strong SOI parameters will be difficult to reproducibly use in devices.

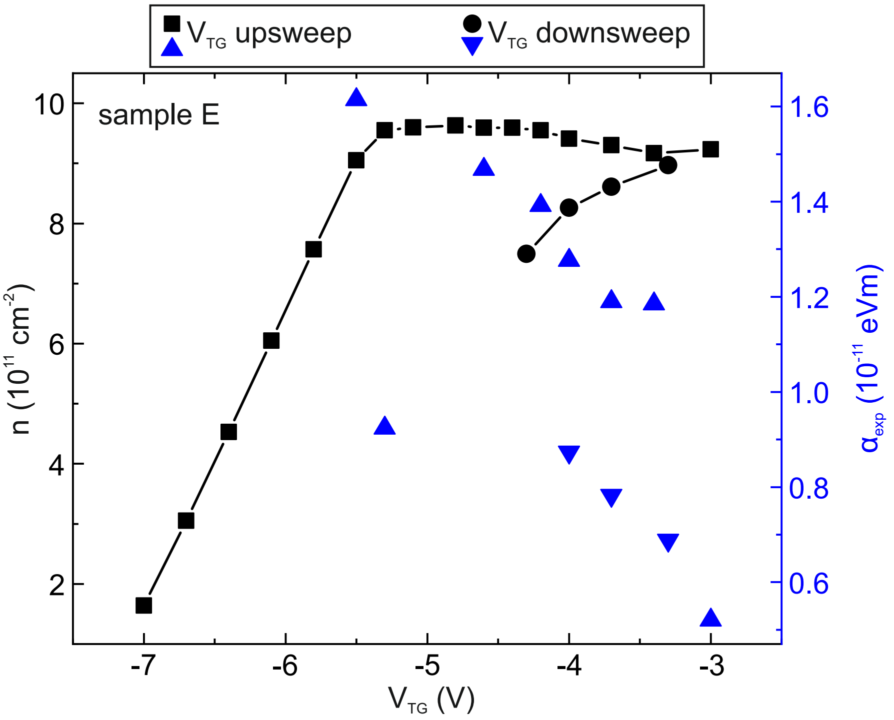

Fig. 6.7: *Electron density* n *of sample E as a function of* V_{TG} *at* $T = 1.7$ *K and* $V_{\mathrm{TG-BCd}} = -6$ *V. In the linear regime I, no SOI-induced beating is observed. With the onset of regime IV, i.e. charge transfer, beating patterns occur and* α_{exp} *(blue) can be extracted. In the subsequent downsweep (black dots), representing regime VI, beating patterns are still visible.*

These biased-cooldown experiments and the SOI analysis in regimes which are characterized by charge transfer highlight the role of DDLs in these InAlAs-based heterostructures. As the charge transfer and thus the modified electrostatics in the heterostructure originate solely from these DDLs in the InAlAs, they also play a crucial role in the built-in SOI in the heterostructure. This has to be taken into account in the design process of such heterostructures.

6.2. Comb-like InAs/InGaAs inset

From our experiments up here we have observed, that a specific modification of α_{int} by only placing the InAs inset (a)symmetrically within the QW comes along with a simultaneous modification of α_{el} while in the first considered, simple case α_{int} vanishes due to the specific choice of the QW design. We hence tried to explore whether α_{int} may be enhanced by purposefully introducing more interfaces within the QW. By carefully separating the InAs inset with thin InGaAs layers, the non-vanishing part of $|\Psi|^2$ experiences more interfaces.

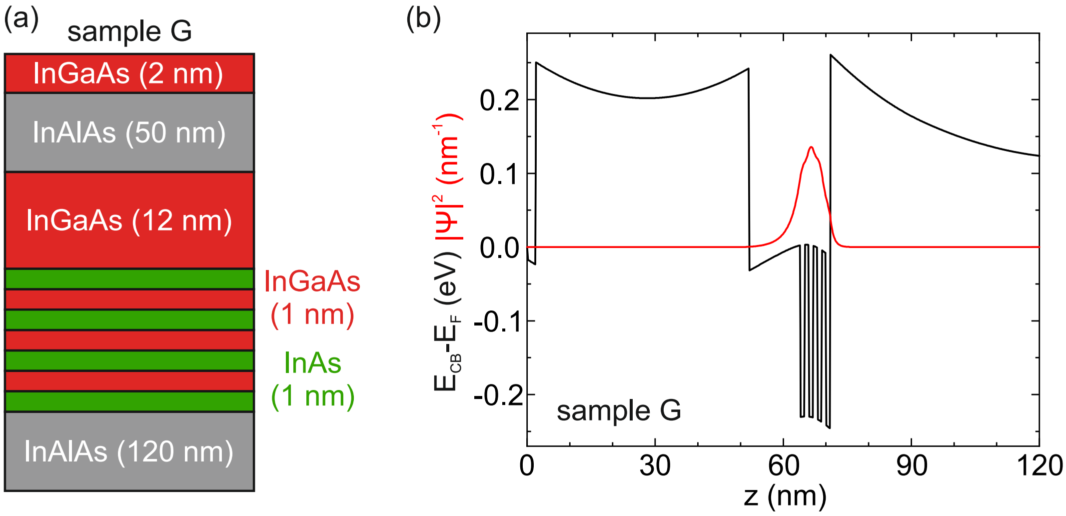

Fig. 6.8: *(a) Heterostructure layout of sample G. (b) CB edge (black) and wavefunction probability density of the first subband (red) of sample G. The InAs inset based off sample F was modified to a comb-like structure by introducing 3 layers of InGaAs, creating six additional interfaces within the QW.*

This should result in a situation, where the individual interface contributions do not cancel each other out in total. For this, we chose an approach to modify the InAs inset based on sample F (see Fig. 6.1(c)) forming a comb-like inset within the QW. This sample G is depicted in Fig. 6.8, where 6.8(a) illustrates the structural layout of the heterostructure and 6.8(b) depicts the CB edge (black) with the wavefunction probability density of the first subband (red). This comb-like design is realized by alternating 1 nm thick InAs and InGaAs layers, ultimately adding six InGaAs/InAs interfaces to the Inset within the QW. Thus, the total thickness of the QW is not changed compared to sample F.
The experimental outcome of sample G is depicted in Fig. 6.9: For $n > 4 \times 10^{11}$ cm^{-2}, SOI-induced beating patterns were visible (represented by the red points in Fig. 6.9(a)). The extracted Rashba parameter α_{exp} from this experiment as a function of the density n is plotted in Fig. 6.9(b). The range $\alpha_{exp} = 0.82 - 1.19 \times 10^{-11}$ eVm is almost identical to sample F as well as the decreasing trend of α_{exp} with increasing density. This suggests, that the introduction of the comb-like inset does not enhance the SOI in this sample G. When we take a look at the two contributions α_{el} and α_{int} to the total α_{sim} in our simulations, we find the following: the combined interface contributions $\alpha_{int,n}$ in sample G do not completely cancel each other out compared to sample F, yet they add up to be negative in total. However at the same time, in this specific design, the electric field contribution α_{el} for $V_{TG} = 0$ V is positive here, due to integration of this comb-like inset, whereas it was negative in sample F. As a consequence, both contributions α_{el} and α_{int} counteract each other. We believe this counteraction to be the reason for our experimental observation that α_{exp} is not enhanced in this sample G. This underlines the complexity of a heterostructure design to maximize α: a change in the interface contribution always brings a modification in the electric field contribution and we have seen that a quantitative simulation of the

intrinsic electric field in a heterostructure is strongly hampered by the complex role of the DDLs. In this particular heterostructures, the electrostatics quite probably cancelled the increase of α_{int}. This again highlights the complexity of α.

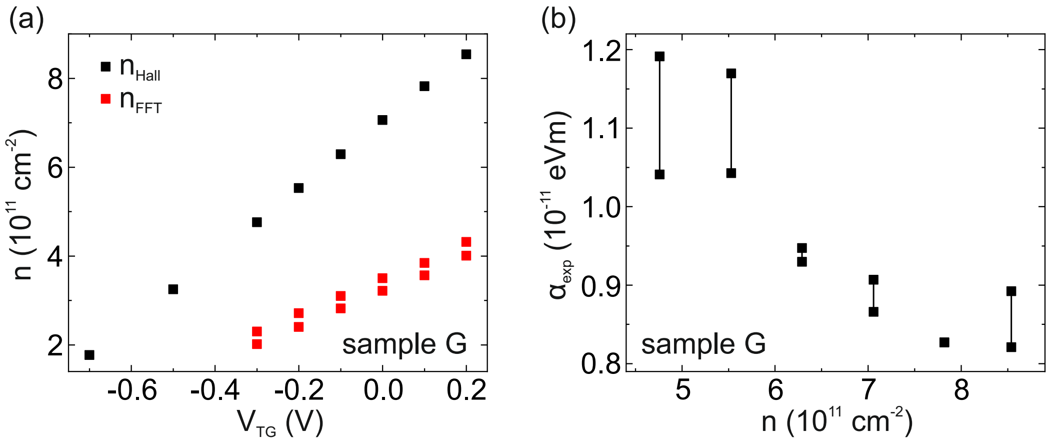

Fig. 6.9: *(a) Electron density n as a function of* V_{TG} *(upsweep) of sample G at* $V_{\mathrm{TG-BCd}} = 0$ *V. For some* V_{TG} *values SOI-induced beating patterns occurred in* ρ_{xx}*, for which the red dots represent the average density* n_{FFT} *of each spin branch extracted with FFT each from positive and negative magnetic field. (b) Rashba parameter* α_{exp} *as a function of electron density n extracted from the FFT density analysis of the SOI induced beating patterns for positive and negative magnetic field.*

6.3. Alternating interfaces in the QW

Based on the conclusions about sample G we considered an approach where α_{int} should be enhanced drastically, while yielding a negligible α_{el}. For this, we present sample H where we introduce interfaces with three different materials within the QW. We achieve this by dividing InGaAs/InAs sections with very thin InAlAs layers. The corresponding heterostructure layout is depicted in Fig. 6.10(a): The QW consists of four InGaAs/InAs transitions each divided by 1 nm thin InAlAs barriers. As the bandstructure calculations in Fig. 6.10(b) suggest, the thin InAlAs barriers do not completely separate $|\Psi|^2$ (red), keeping the nature of a singular QW. This design is inspired by Hao [94, 95], which reported a higher interface contribution to Rashba-SOI by the introduction of ultrathin but energetically high barriers within the QW. Due to our choice of the arrangement order, each InAlAs/InGaAs and InGaAs/InAs interface (in direction from the surface towards the substrate) offers a negative interface contribution $\alpha_{int,n}$ while only the InAs/InAlAs interfaces add a positive contribution. As a consequence, this should offer in total a significantly negative α_{int}. Due to the more symmetrical design of the QW compared to (the asymmetrical) samples D, F and G, the electric field contribution α_{el} for sample H is negligible, leaving α_{int} as the dominant contribution to the total α. Note, that this however is only valid for the situation at $\mathrm{V_{TG}} = 0$ V and further calculations would be necessary to describe situations with $\mathrm{V_{TG}} \neq 0$ V.

We have observed in the experiments with sample H, depicted in Fig. 6.11(a), that only for

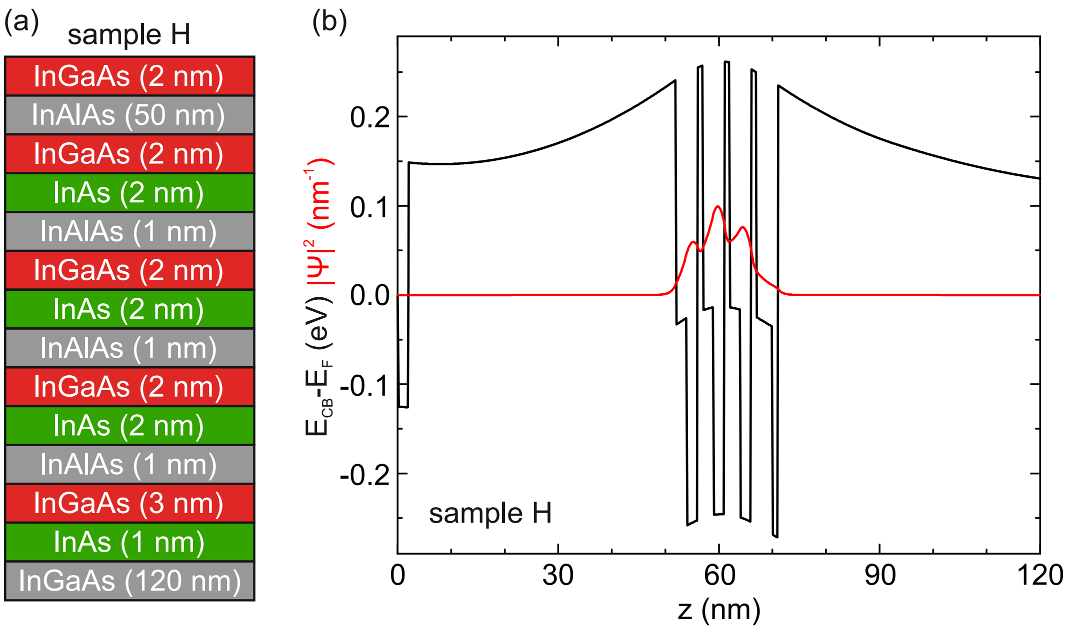

Fig. 6.10: *(a) Heterostructure layout of sample H. (b) CB edge (black) and wavefunction probability density of the first subband (red) of sample H. The QW consists of a sequence of InAs and InGaAs divided by very thin InAlAs barriers. As the InAlAs barriers are only* 1 *nm thin, the electric structure of a singular QW remains, i.e. the wavefunction probability density is not separated into multiple parts. This allows for a larger α_{int} as the individual interface suggest to not cancel each other out.*

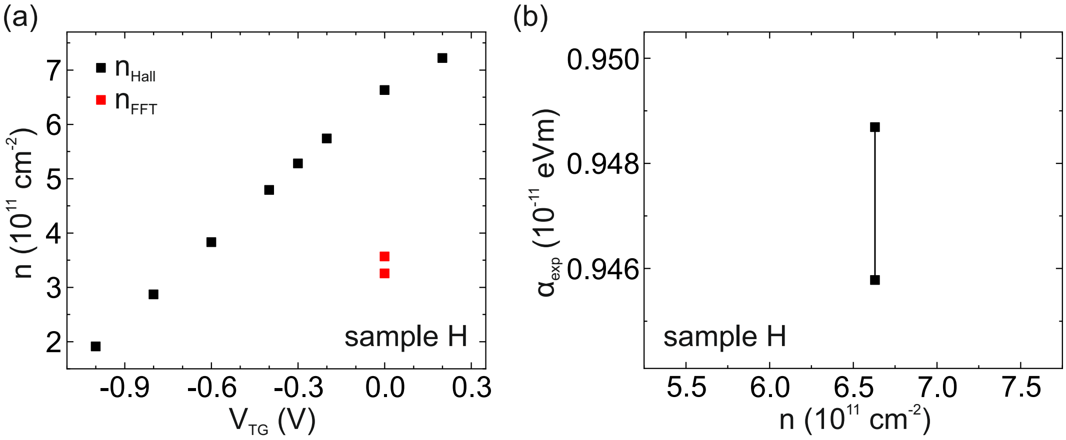

Fig. 6.11: *(a) Electron density n as a function of V_{TG} (upsweep) of sample H at $V_{TG-BCd} = 0V$. For only $V_{TG} = 0$ V SOI-induced beating patterns occurred in ρ_{xx}, for which the red dots represent the average density n_{FFT} of each spin branch extracted with FFT each from positive and negative magnetic field. (b) Rashba parameter α_{exp} for $n = 6.7 \times 10^{11}$ cm^2 ($\hat{=}$ $V_{TG} = 0$ V) extracted from the FFT density analysis of the SOI induced beating patterns for positive and negative magnetic field.*

$\mathrm{V_{TG}} = 0$ V SOI-incuded beating patterns occurred (red points), from which we extracted $\alpha_{exp} = 0.94 \times 10^{-11}$ eVm, see Fig. 6.11(b). This value is comparable to samples D, F and G, meaning that this QW design does not lead to an enhancement of α_{exp}.

6.4. Conclusion

In conclusion of this chapter, we have shown with samples D, E and F, that only an (a)symmetric placement of an InAs inset within the InGaAs QW does not enhances the interface contribution α_{int} to to the total Rashba parameter α. Instead, α in all three heterostructure designs is governed by the electric field contribution α_{el}. Although this can be modified by exploiting the gate operation characteristics of this heterostructure type, they bring the disadvantage of metastability. However, our previously presented CTM allows to partially predict the evolution of Rashba SOI during gate operation, ultimately leading to strongly enhanced α for gating regimes outside the linear regime. This however, is not addressed in the literature. We have shown an approach with sample G on how to increase α_{int} by separating the InAs-inset with thin InGaAs layers to create a comb-like structure. This modification of the QW design caused a siginficant impact on α_{el}, ultimately creating a situation where α_{int} and α_{el} cancel each other out. By further increasing α_{int} in sample H with the introduction of thin InAlAs barriers within the QW, the design of the QW simultaneously results in negligible α_{el}. This design should, based on the simulations, result in a high total α, which we could not confirm with our experiments.
Note here we observe in sample H for various $\mathrm{V_{TG}}$ a dip in ρ_{xx} for small magnetic fields $B \ll \pm 0.1$ T which we assign to weak anti-localization (WAL) (see Sec. 2.3.4). This is true for most of the samples investigated in this thesis, however only for configurations with rather low electron mobility, i.e. $\mu < 1 \times 10^5$ cm^{-2}. In all configurations where WAL is visible, we do not observe any SOI-induced beating patterns. Those are only visible for higher mobility. Although [30] suggests that WAL occurs only for small mobility, no limits are reported nor a justification for this statement. Interestingly, reports in the literature [16, 84, 89, 93, 96–99] which observed WAL in comparable heterostructures do not write about beating patterns. It seems, that either WAL or beating patterns are observed, but only each for itself and not both together for the same configuration. This raises the question, why only either one can be observed. To our knowledge, this is not addressed in the literature yet.

Prospects But, we can draw some new ideas and outline a few approaches towards further improving α for these heterostructures: Based on samples D, E and F, two parameters would both, according to theory and literature, lead to a significant impact on α: the thickness and the depth of the QW. Based on calculations from Hao [100], an increase of the QW thickness results in a (non-linear) decrease of α. This decrease was experimentally observed by Lee *et al.* [101]and Schäpers *et al.* [102] in InGaAs-based QWs where the thickness of an InAs inset within InGaAs was increased, $2-7$ nm in [101] and $2-8$ nm in [102]. Our samples D, E and F are on the upper limit compared to these studies, as they are designed with a 7 nm InAs inset. Thus, this suggests that a reduction of the inset thickness could result in higher SOI in our heterostructures. Along with the potentially higher SOI, a reduction of the inset thickness should enhance the electron mobility. This is due to less strain for thinner InAs, as the growth of InAs on $In_{0.75}Ga_{0.25}As$ is not fully lattice-matched. A higher mobility could then promote a better visibility of beating patterns in ρ_{xx}, improving the analysis. But, the reduced inset thickness will also impact the band bending of the structure, leading to a (either enhancing or degrading) modified electric field contribution α_{el}. This is an approach which should be tackled in future investigations.

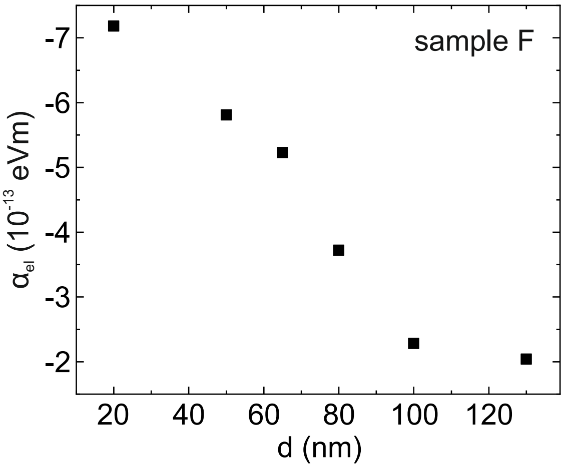

Fig. 6.12: *Calculation of the electric field contribution α_{el} for sample F as a function of the InAlAs barrier thickness d between the InGaAs cap and the QW. By reducing the depth of the QW below* 100 *nm, α_{el} increases linearly.*

Regarding the depth of the QW, we have performed some simulations and calculations based on sample F: we successively reduced the InAlAs barrier thickness d between the QW and the InGaAs cap from 130 nm to 20 nm. By reducing this thickness, the interface contributions $\alpha_{int,i}$ to the total α_{sim} remain constant while keeping their opposite contribution sign, i.e. they still cancel each other out regardless of the QW depth. The electric field contribution α_{el} however increases (linearly for $d < 100$ nm) while d is decreased, which can be seen in Fig. 6.12. This trend was observed for overall smaller distances in [84, 93]. We suggest from our experimental experience in [103, 104] to keep a minimum d of $15 - 20$ nm, otherwise the impact of surface and interface contributions significantly degrades the electron mobility of the 2DES in the QW.

While trying to improve the heterostructure design by adjustments based on the conduction band edge of the materials, a considerable contribution factor A_{int} within the interface contribution α_{int} (see Eq. 2.45 with Eq. 2.47 in Sec. 2.3.2) is calculated by the band offsets in the heavyhole (HH) / lighthole (LH) band and the split-off (SO) band:

$$\alpha_{int} \propto \sum_n S_n \cdot A_{int} \cdot |\Psi(z_n)|^2, \tag{6.2}$$

$$A_{int} = \frac{\Delta E_{\Gamma_7}}{\left(E_F - E_{\Gamma_7}^{M,1}\right)^2} + \frac{\Delta E_{\Gamma_7}}{\left(E_F - E_{\Gamma_7}^{M,2}\right)^2} - \frac{\Delta E_{\Gamma_8}}{\left(E_F - E_{\Gamma_8}^{M,1}\right)^2} - \frac{\Delta E_{\Gamma_8}}{\left(E_F - E_{\Gamma_8}^{M,2}\right)^2} \tag{6.3}$$

where ΔE_{Γ_i} denotes the band edge offset between two materials M, j (direction of order from the surface towards the substrate) at the transition and $\left(E_F - E_{\Gamma_i}^{M,j}\right)$ the absolute value of each material at the transition, while Γ_i denotes the band type with $\Gamma_8\widehat{=}$ HH/LH-band and $\Gamma_7\widehat{=}$ SO-band. A_{int} then suggests, that the band edge course of both valence bands (VBs) can have significant impact on the whole interface contribution apart from the CB course [98]. For the presented heterostructures up to here, this factor was rather negligible. This factor however can be significantly enhanced by the introduction of antimony (Sb) as a substitute for arsenic (As) in specific layers in the QW, as the course of the VBs e.g. for InSb and $\mathrm{In_{0.75}Ga_{0.25}Sb}$ in combination with InAs and InGaAs offers significantly high band offsets and thus, enhanced SOI. A first experimental approach with such a heterostructure design is presented in the appendix as sample I, see App. B.

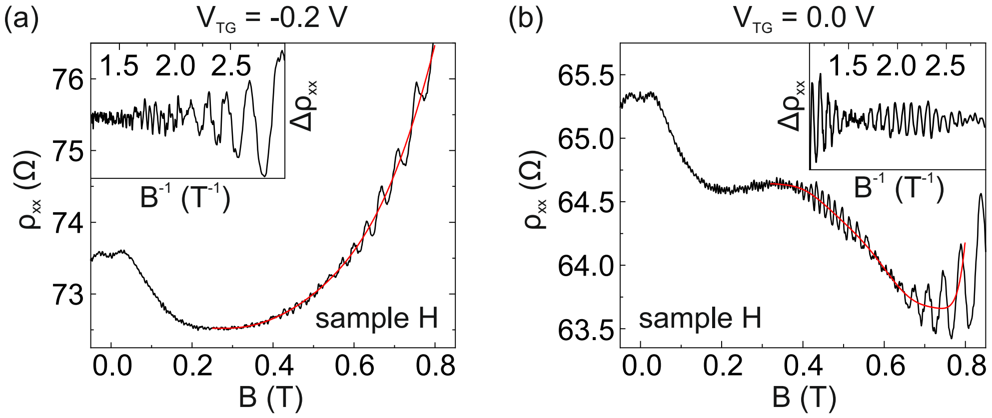

Fig. 6.13: *Longitudinal magnetotransport data ρ_{xx} of sample H at $T = 1.7\,K$ for $V_{\mathrm{TG}} = -0.2$ V (a) and $V_{\mathrm{TG}} = 0$ V (b). The red trace indicates the fitted polynomial background, which is then subtracted. The residual $\Delta\rho_{xx}$ is then plotted as a function of the inverse magnetic field, depicted in the inset. Clearly and pronounced beating patterns are only visible for $V_{\mathrm{TG}} = 0$ V.*

Although the simulations of sample H suggest a significantly enhanced SOI compared to the previous samples, we only observe SOI-induced features in the magnetotransport for one configuration ($\mathrm{V_{TG}} = 0\,\mathrm{V}$), yielding a α_{exp} value similar to the average of all previous samples presented in this thesis. Although the maximum electron mobility is not substantially degraded due to the introduction of the InAlAs barriers ($1.6 \times 10^5\,\mathrm{cm^2/Vs}$ compared to $1.8 - 6.0 \times 10^5$ $\mathrm{cm^2/Vs}$ in the previous samples), ρ_{xx} shows a strong background for all $\mathrm{V_{TG}}$ for $B < 1\,\mathrm{T}$ compared to the previous samples. This is also the magnetic field range, where beating patterns are most pronounced and thus analyzed, complicating the subtraction of this background. Additionally, the signal-to-noise ratio (SNR) in this sample H is significantly smaller compared to the previous samples, making the detection of beating patterns in the SdH oscillations more difficult. We have visualized this exemplarily in Fig. 6.13, where (a) shows ρ_{xx} at $\mathrm{V_{TG}} = -0.2\,\mathrm{V}$ and (b) at $\mathrm{V_{TG}} = 0\,\mathrm{V}$. The red trace indicates the background we subtracted in order to get a clear oscillation signal. The inset depicts then the subtracted signal $\Delta\rho_{xx}$ as a function of the inverse magnetic field. For $\mathrm{V_{TG}} = -0.2$ V in Fig. 6.13(a), ρ_{xx} shows signs of a beating pattern, but the high noise level prevents us to resolve nodes in the beating pattern. For $\mathrm{V_{TG}} = 0\,\mathrm{V}$ in Fig. 6.13(b) the noise level is sufficiently small in order to resolve nodes in the beating pattern. We observed a rather poor SNR with underlying signs of a beating pattern also for $\mathrm{V}_{\mathrm{TG}} = -0.4$ V which suggests, that this sample H would exhibit signatures of SOI, but our measurement setup does not allow us to detect and reliably analyze those patterns. Improvements in the measurement setup and technique were not feasible over the course of this thesis, however we would like to suggest a few improvements which should tackle the issues: First, the measurement temperature. By decreasing the temperature, the SdH oscillation amplitude increases and thus the SNR should be enhanced [30]. Our experiments were performed at $T = 1.7$ K. The literature suggests that the measurement temperature should be decreased to at least 300 mK or lower. Second, thermally-anchored filters within the measurement lines should reduce noise, thus enhancing the SNR. And third, utilizing statistics by repeating the measurements and thus enhancing again the SNR. These improvements may help also in the analysis of sample E (see Fig. 6.1(b), which suggests a smaller α_{exp}. A better resolution in ρ_{xx} would help to emerge beating patterns induced by smaller SOI.

7. InAlAs-based heterostructures with top- and backgate

Up to here, the topgate electric field was used as a tool to investigate the Rashba SOI over the course of the gate response of the heterostructure. We used bandstructure engineering as the main parameter to govern the SOI by specifically modifying the heterostructure. Here in Ch. 7 we specifically utilize the electric field as a parameter to tune the Rashba SOI. By adding a second gate electrode on the opposite side of the TG electrode (compared to the QW), the electric field is enhanced if the sign of the applied voltages on the two gate electrodes is different. With this, the electron density of the 2DES in the QW can be kept constant while the electric field in the QW is varied. Thus, we eliminate the influence of the electron density on α.

7.1. Characterization of a backgate in InAlAs-based heterostructures

We realize this second gate electrode with a heterostructure design, where we use a GaAs (100) substrate as backgate (BG) electrode, which is highly n-type doped with silicon (compared to an undoped and thus semi-insulating GaAs (100) substrate for all the heterostructures presented up to here)[10]. Fig. 7.1(a) shows this heterostructure layout of sample J. The QW design is similar to the one from sample G (see Sec. 6.2). To increase the dielectric constant of the semiconductor material between the BG and the QW, a 1μm thick GaAs layer (cyan in Fig. 7.1(a)), grown under low-temperature (LT) growth conditions with a subsequent high-temperature annealing step [105–110], is implemented before the InAlAs step-graded buffer. For the TG dielectric, 100 nm SiO_x is deposited via plasma-enhanced chemical vapor deposition. Note that, for all samples up to here Al_2O_3 was used as a gate dielectric. However, samples with a BG and Al_2O_3 as a TG dielectric have shown significant BG leakage current across several samples[11]. The equivalent circuit diagram of sample J is depicted schematically in Fig. 7.1(b). As the 2DES in the QW is grounded via the applied source-drain (SD) voltage V_{SD}, the system can be divided into two capacitive circuits, one with the TG and one with the BG via V_{TG} and V_{BG}, characterized by the capacitive coupling constants c_{TG} and c_{BG}.

This sample J is the first InAlAs-based heterostructure with a BG produced in our group. As the DDLs in InAlAs govern the gate response of top-gated samples as well as the SOI, we assume they also play a major role in the gate response of the BG. Note that back-gated structures in InAlAs-based systems with 75% indium were reported only by Grundler [9] without data about gate response and transport properties. Fig. 7.2(a) displays the electron density n of sample J as a function of V_{TG} (black squares) and V_{BG} (blue triangles). Each measurement represents a gate voltage upsweep after MIT. For each of the two traces, the system was cooled down unbiased ($V_{TG-BCd} = V_{BG-BCd} = 0$ V). While one gate sweep (e.g. V_{TG}) was performed, the other gate voltage (V_{BG}) was kept

---

[10] A simple approach by using the gold-plated base of the chip carrier as a backgate electrode turned out to be impractical. Due to the large distance of the base plate to the QW (worsened by the inhomogeneous distribution of mounting glue of the sample), voltages $\gg 300$ V were necessary to significantly manipulate the electron density in the 2DES.

[11] Such behavior was also implicitly reported by Shoajei *et al.* [111]: They had to etch windows into the Al_2O_3 before contacting the contact pads to prevent a short-circuit. However, they do not give any further details.

constant at 0 V. Between the two measurements, the system was brought to RT to fully reset the system.

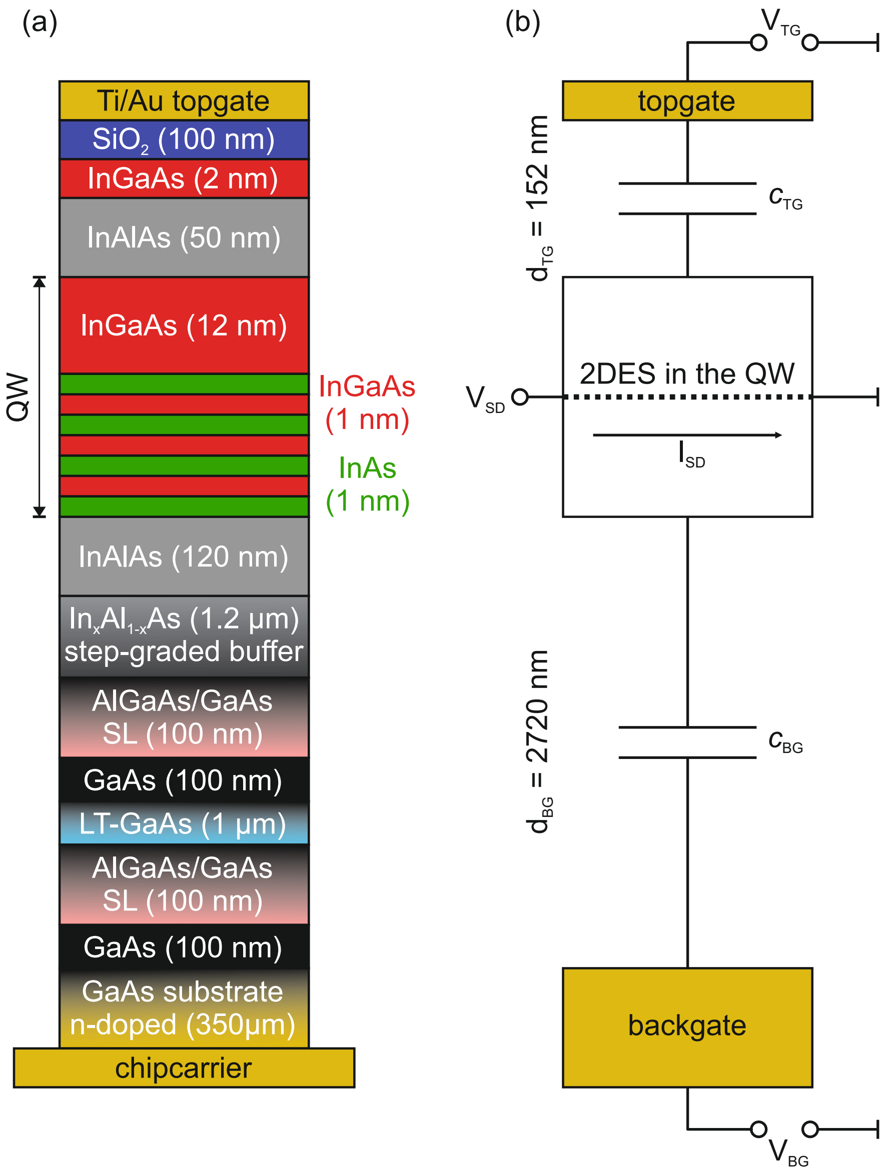

Fig. 7.1: *(a) Heterostructure layout of sample J. Based on the QW design of sample G, a backgate (BG) electrode was implemented by using a highly n-doped GaAs (100) substrate. A 1µm LT-GaAs layer (cyan) prevents excess leakage current. (b) Schematical equivalent circuit diagram of sample J, visualizing the two capacitive gate-electrode circuits. The 2DES in the QW is grounded via the laterally applied source-drain (SD) voltage* V_{SD}. *The BG circuit is characterized by the coupling constant* c_{BG}*, TG similarly by* c_{TG}.

Both gate responses exhibit a linear dependence for a specific V_{gate} range before the density saturates. Two striking differences appear: First, the saturation density achieved via V_{BG}, $n_{sat} = 6.3 \times 10^{11}$ cm^{-2}, is smaller compared to $n_{sat} = 8.6 \times 10^{11}$ cm^{-2} of the TG. Second, the density requires a equilibration time to settle for the adjustment of V_{BG} at each measurement point. For V_{TG}, it does not. This will be discussed in the following sections. We extract the capacitive coupling constant c, represented by the slope of the gate response from a linear fit, which is marked in red in Fig. 7.2(a). As expected from the larger distance of the BG to the QW $d_{BG} = 2720$ nm compared to $d_{TG} = 152$ nm from the TG to the QW, the capacitive coupling constant for the BG is significantly smaller compared to the TG ($c_{BG} = 0.40$ cm^{-2}V^{-1} vs. $c_{TG} = 3.25$ cm^{-2}V^{-1}). Fig. 7.2(b) depicts the electron mobility μ of sample J as a function of the electron density n adjusted via V_{TG} (black squares) and V_{BG} (blue triangles). For comparable densities, i.e. $n = 2 - 6 \times 10^{11}$ cm^{-2}, the electron mobility is in good agreement for V_{TG} and V_{BG}, thus characterizing similar transport properties within the two different gate responses.

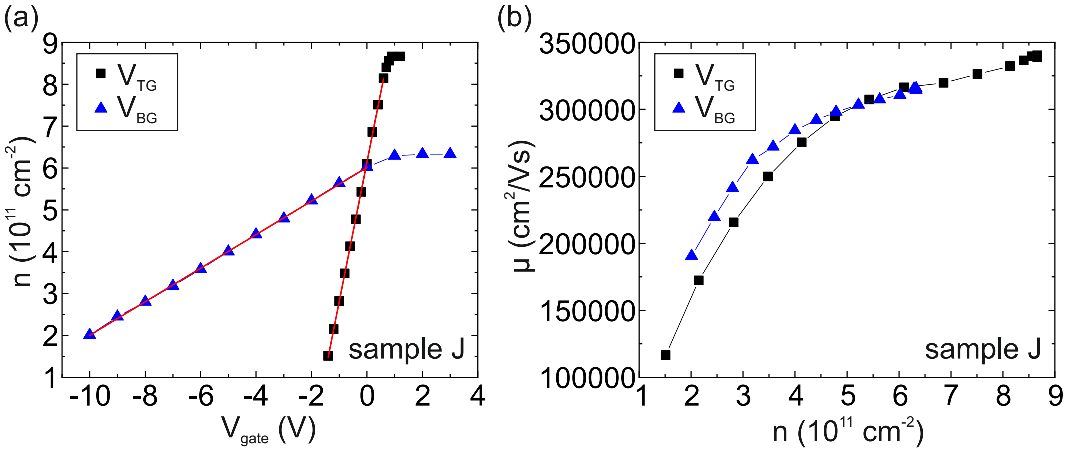

Fig. 7.2: *(a) Electron density n of sample J as a function of V_{TG} (black squares) and V_{BG} (blue triangles). The red lines indicate the linear fit from which we extract c_{TG} and c_{BG}. (b) Electron mobility μ of sample J as a function of the electron density n, adjusted via V_{TG} (black squares) and V_{BG} (blue triangles).*

7.1.1. Backgate downsweep

During the characterization of the gate response of the BG, two peculiarities appear. The saturation density in a BG sweep is smaller compared to a TG sweep and, most strikingly, the density requires a settling time to reach its equilibrium value. Most interestingly, the latter is true not only in an upsweep, but also in a downsweep. As this settling time indicates a charge transfer (see Ch. 5), the gate response of the BG is constantly governed by a charge transfer. The linearity of the gate response in Fig. 7.2(a) suggests similarities with the characteristics of a regime VI (see Sec. 5.3.7). This motivates a closer look at the gate response of the BG in sample J. Fig. 7.3 shows the electron density n of sample J as a function of a V_{BG} downsweep at $V_{TG} = 0$ V. Sweeping from $V_{BG} = 0$ V to $V_{BG} = -3$ V and stopping there for a given duration (horizontal line in the inset in Fig. 7.3) reveals a significant loss of electrons over several minutes although V_{BG} is kept constant (vertical evolution of the density at V$_{\text{BG}}$ = −3 V in Fig. 7.3). Sweeping the BG up after this waiting time reveals a smaller slope (in the linear density reaction) compared to the slope for the previous downsweep.

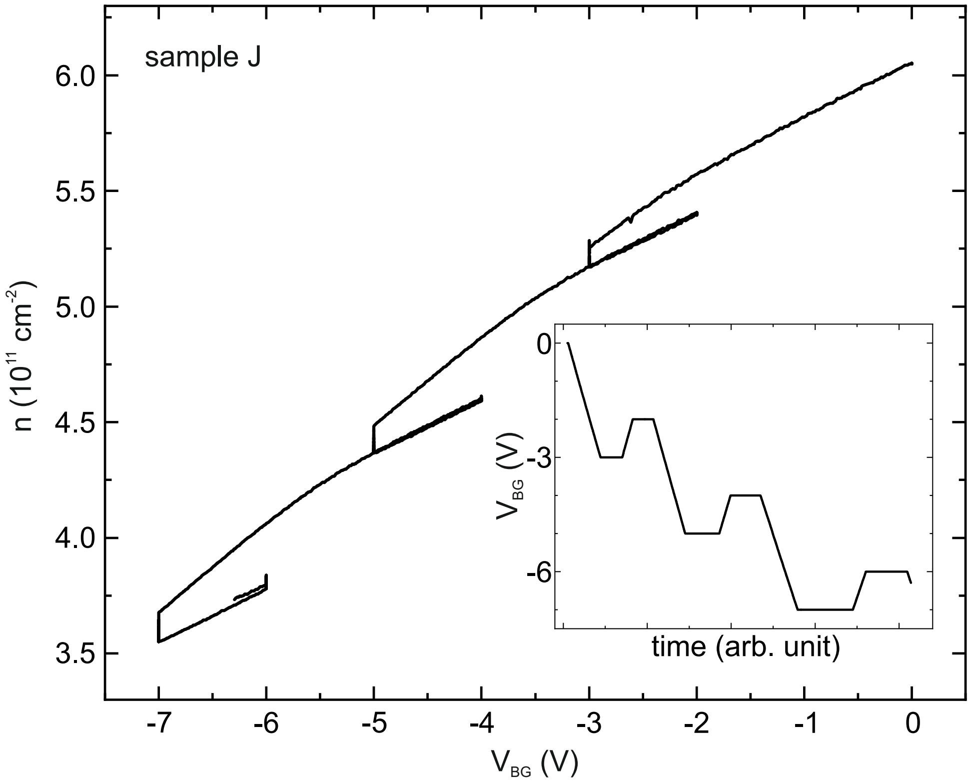

Fig. 7.3: *Electron density n of sample J as a function of a* V_{BG} *downsweep at* $V_{\text{TG}} = 0$ *V. During the* V_{BG} *downsweep, several stops are implemented during which the density decreases. From this stop, a upsweep with a subsequent downsweep leads to no hysteresis while exhibiting a smaller slope than the previous downsweep. The inset shows the* V_{BG} *routine applied.*

In our understanding this complex behavior is similar to regime VI discussed in the context of TG sweeps (see Sec. 5.3.7). Here, we observe an electron loss (compared to an electron increase in regime VI in Sec. 5.3.7). In order to explain this, we take a closer look at the bandstructure of sample J in Fig. 7.4: The CB edge (black) is depicted together with the DDLs in the InAlAs (green and magenta) as well as the wavefunction probability density $|\Psi|^2$ (red) as a function of the inverse growth direction z for V$_{\text{BG}}$ = 0 V (a), V$_{\text{BG}}$ = −3 V (b) and V$_{\text{BG}}$ = −6 V (c), while V$_{\text{TG}}$ is kept constant at V$_{\text{TG}}$ = 0 V. When V$_{\text{BG}}$ is decreased, the CB edge from the QW towards the BG is shifted upwards. Simultaneously however, the CB edge from the QW towards the TG is shifted downwards. As a consequence, the triangular-shaped potential barrier between the QW and the InAlAs towards the TG becomes smaller and narrower, i.e. more transparent. Thus, electrons can tunnel out of the QW via the DDLs into the interface between the semiconductor and the dielectric, although V$_{\text{TG}}$ is kept constant at V$_{\text{TG}}$ = 0 V. This explains the loss of electrons during the waiting time in the BG downsweep in Fig. 7.3. In a directly following upsweep, this loss is temporarily suspended. The slope is then smaller. It changes to a steeper one during a downsweep while at a certain V_{BG} the charge transfer (loss of electrons) sets on again. This loss of electrons enhances the depletion induced by the V_{BG} downsweep, hence the steeper slope.

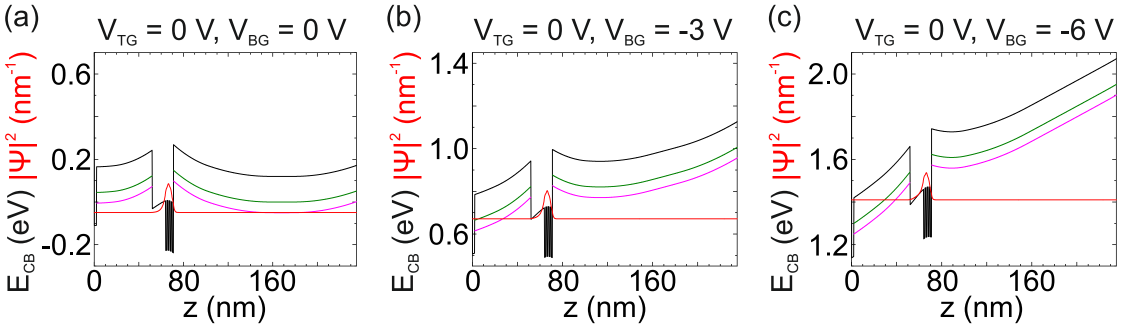

Fig. 7.4: *CB edge (black) and wavefunction probability density* $|\Psi|^2$ *(red) of sample J for* $V_{BG} = 0$ *V (a),* $V_{BG} = -3$ *V (b) and* $V_{BG} = -6$ *V (c). The DDLs are indicated in green and magenta. With decreasing* V_{BG}*, the triangular-shaped potential barrier between the QW and the InAlAs towards the TG becomes more transparent, although* $V_{TG} = 0$ *V is kept constant.*

We indeed have good experimental evidence for this complex behavior. Fig. 7.5 shows the TG-induced gate response of sample J for various fixed V_{BG}. The applied gate cycle is depicted in the inset in Fig. 7.5 and is identical for all V_{BG} values. Between each different V_{BG} value, the sample was brought to RT to fully reset the system. After the cooldown, V_{BG} is set and the gate cycle is initiated by a V_{TG} downsweep from $V_{TG} = 0$ V (indicated by the squares in Fig. 7.5) below MIT, followed by an upsweep to $V_{TG} = +1.1$ V where density saturation sets in. Subsequently, a V_{TG} downsweep is performed below MIT again, which opens up a hysteresis. For $V_{BG} = 0$ V (black trace in Fig. 7.5), the observed behavior is identical to what we would expect for the TG gate response of such a sample according to our CTM (see Sec. 5.5.2). When a negative V_{BG} is applied (red, blue and olive traces in Fig. 7.5), the saturation density decreases significantly. In our model, the transition from the increasing density into the density saturation is governed by the transparency of the triangular-shaped potential barrier between the QW and the InAlAs towards the TG. Thus, the negative V_{BG} leads to a more transparent potential barrier and thus to the observed decreased saturation density.

Note that a positive V_{BG} (green trace in Fig. 7.5) does not shift either the saturation density nor the overall gate response compared to $V_{BG} = 0$ V. This suggests, that the capacitive coupling of the BG to the QW is ineffective for $V_{BG} > 0$ V. Indeed, when we look at the V_{BG} gate response in Fig. 7.2(a), the system is in saturation for $V_{BG} > 0$ V, indicating a reduce-to-vanishing capacitive coupling of the BG to the QW. As we have shown in Fig. 7.4(a), the InAlAs from the QW towards the BG forms a trough due to the DDLs. Those DDLs at the apex of the trough are below the Fermi energy even at $V_{BG} = V_{TG} = 0$ V, similar to the situation with a TG described in Sec. 5.5.1. This can indeed result in the observed reduced to vanishing capacitive coupling from the BG to the QW as observed in Fig. 7.2(a) and Fig. 7.5. Additionally, this suggests that a charge transfer from the QW into the DDLs in the InAlAs towards the BG already happened at $\mathrm{V_{BG}} = \mathrm{V_{TG}} = 0$ V while at the same time, an increasing $\mathrm{V_{BG}}$ should enhance this transfer.

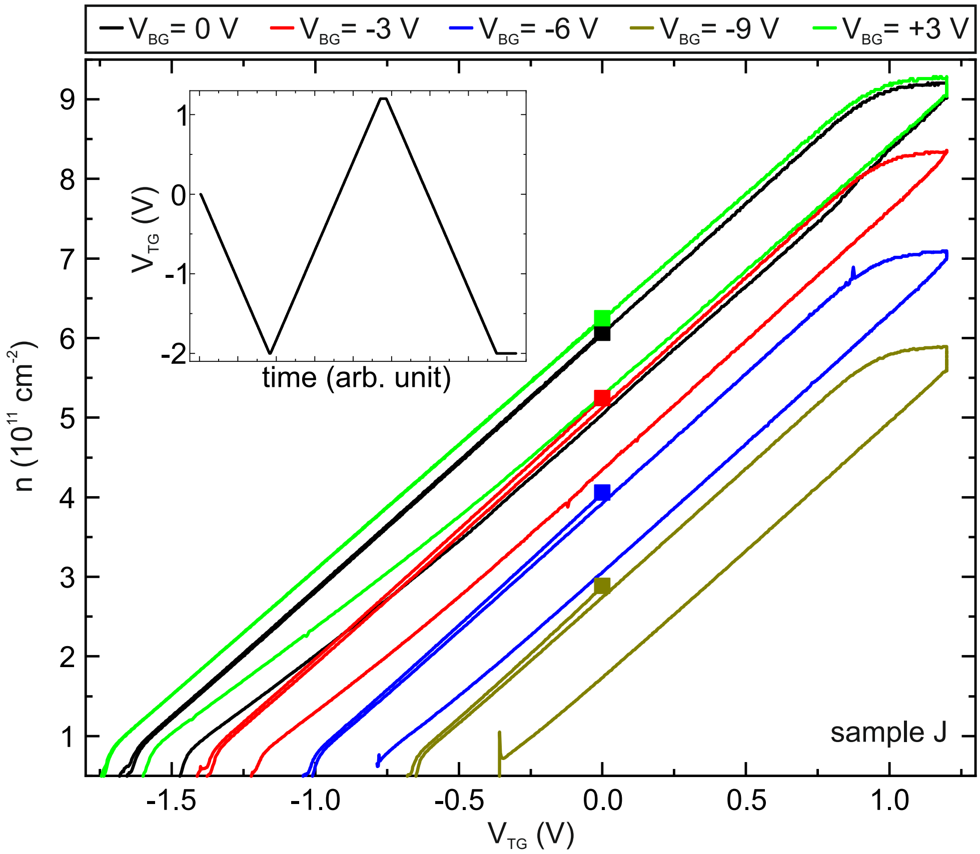

Fig. 7.5: *Electron density n of sample J as a function of* $\mathrm{V_{TG}}$ *at different fixed* $\mathrm{V_{BG}}$*. Between each* $\mathrm{V_{BG}}$*, the sample was brought to RT to fully reset the system. After each cooldown, the* $\mathrm{V_{TG}}$ *gate cycle was initiated by a downsweep below MIT. The starting point of the cycle is indicated by the squares. A subsequent upsweep to the onset of saturation is followed by a downsweep again below MIT. The inset shows the* $\mathrm{V_{BG}}$ *routine applied.*

7.1.2. Backgate upsweep

In this sample J, a charge transfer is not only observed in a $\mathrm{V_{BG}}$ downsweep but also in a $\mathrm{V_{BG}}$ upsweep, which is depicted in Fig. 7.6. This $\mathrm{V_{BG}}$ upsweep was performed at $\mathrm{V_{TG}} = 0\,\mathrm{V}$ after MIT from the downsweep presented previously in Fig. 7.3. By sweeping from $\mathrm{V_{BG}} = -4$ V to $\mathrm{V_{BG}} = -2$ V, the density increases linearly while the slope transitions at $\mathrm{V_{BG}} = -3$ V to a steeper slope. Stopping at $\mathrm{V_{BG}} = -2$ V for a given duration (horizontal line in the inset in Fig. 7.6) reveals a significant increase of the density (vertical evolution of the density at $\mathrm{V_{BG}} = -2$ V) although $\mathrm{V_{BG}}$ is kept constant.

A following $\mathrm{V_{BG}}$ downsweep with a subsequent upsweep does not open a hysteresis while at the same time the slope is smaller compared to the previous upsweep. For $\mathrm{V_{BG}} \geq +3$ V, the density saturates at $n_{sat} = 6.3 \times 10^{11}$ cm^{-2}.

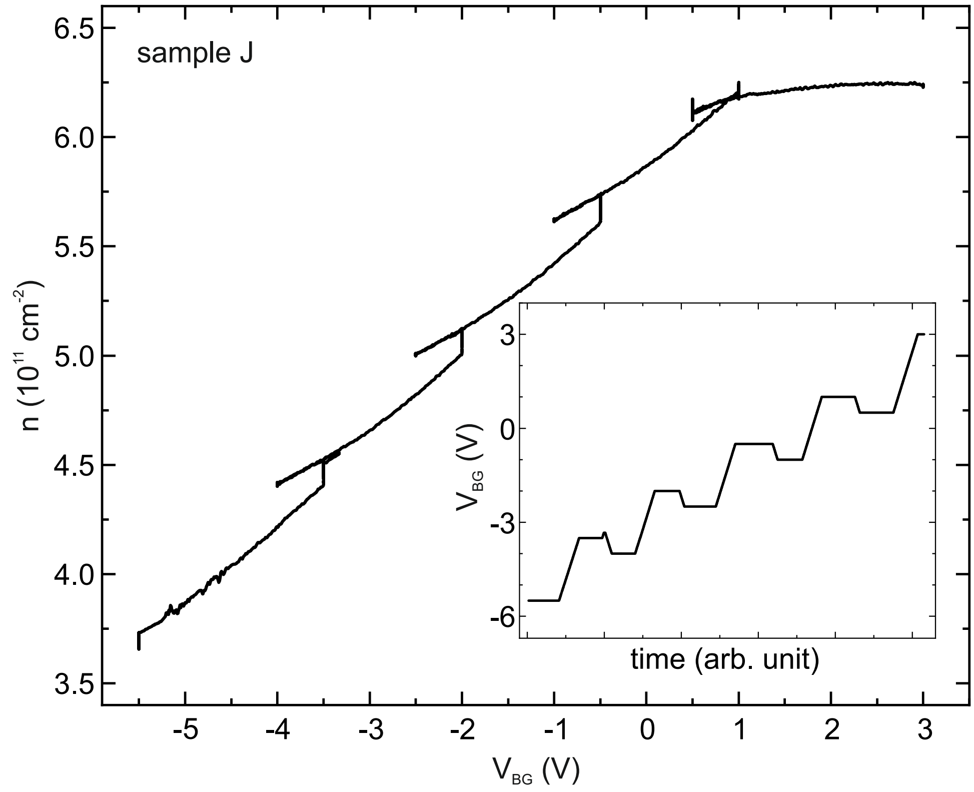

Fig. 7.6: *Electron density n of sample J as a function of a V_{BG} upsweep at $V_{\mathrm{TG}} = 0$ V. During the V_{BG} upsweep, several stops are implemented during which the density increases. From this stop, a downsweep with a subsequent upsweep leads to no hysteresis while exhibiting a steeper slope than the previous upsweep. The inset shows the V_{BG} routine applied.*

The observed density increase during a waiting time in the upsweep cycle is counterintuitive and, at first sight, contrary to our CTM developed with a system with a TG. One would expect to loose electrons from the QW to DDLs sites in the InAlAs towards the BG as this InAlAs inherits a significant trough while a $\mathrm{V_{BG}}$ upsweep bends the CB edge downwards. However, the observed density increase can be explained consistently within our CTM:

Due to the trough-like shape of the InAlAs towards the BG (also towards the TG but reduced due to only 50 nm InAlAs compared to > 120 nm towards the BG), the 2DES in the QW faces a triangular-shaped potential barrier both towards the BG and the TG. When $\mathrm{V_{BG}}$ is now increased, the CB edge on the BG-side of the QW shifts downwards, enabling a multi-step tunneling of electrons out of the QW into the DDLs in the InAlAs towards the BG. At the same time, the CB edge on the TG-side of the QW is shifted upwards. As a consequence, the electrons, which were transferred previously into DDLs in the InAlAs towards the TG and the interface to the dielectric, are transferred via multi-step tunneling back into the QW. During the $\mathrm{V_{BG}}$ upsweep before the onset of a saturation, the density increases linearly with $\mathrm{V_{BG}}$. This suggests, that the rate of electron re-transferred from the TG side into the QW is higher than the loss-rate of electrons transferred into the InAlAs towards the BG. The situation changes when a certain $\mathrm{V_{BG}}$ is applied, for which the density saturates: From this $\mathrm{V_{BG}}$ onwards, the two rates of increase and decrease are equal, resulting in the observed density saturation. We do not observe a decrease of the density with even higher $\mathrm{V_{BG}}$, which suggests that after a certain $\mathrm{V_{BG}}$ is applied, the BG electric field is screened by a large accumulation of electrons between the BG and the QW. This is possible because during the complete $\mathrm{V_{BG}}$ upsweep, electrons are transferred from the QW into the InAlAs towards the BG. As the CB edge on this BG-side is shifted downwards, they may accumulate at a location within the heterostructure and cause a screening, similar to the accumulation of electrons at the interface to the dielectric described in regime IV and V (see Sec. 5.3.5 and 5.3.6). The saturation density during the $\mathrm{V_{BG}}$ upsweep is coincidentally smaller compared to the $\mathrm{V_{TG}}$ upsweep. Although both saturation mechanisms are basically similar, they do depend individually on the exact bandstructure and electrostatic configuration in their respective part of the heterostructure. Regarding a possible electron accumulation position between the QW and the BG: below (towards the BG) the constant composition InAlAs, i.e. the virtual substrate, the overshoot of the $\mathrm{In}_x\mathrm{Al}_{1-x}\mathrm{As}$ step-graded buffer offers a energetically favorable place for electrons[12]. A multi-step tunneling of electrons out of the QW via the DDLs into the BG-side InAlAs could cause these electrons to accumulate in this overshoot layer. This could lead to the observed screening. However we do not measure these electrons in the magnetotransport of the sample.

We have experimental evidence to support our model of these described complex transfer processes: Fig. 7.7 shows the electron density n of sample J as a function of $\mathrm{V_{BG}}$ upsweeps, for which we simultaneously apply different $\mathrm{V_{TG}}$. The sample was cooled down with $\mathrm{V_{BG}} = \mathrm{V_{TG}} = 0\,\mathrm{V}$, then the various $\mathrm{V_{TG}} \neq 0$ V were applied and a $\mathrm{V_{BG}}$ downsweep below MIT was performed, which is not shown here. Between each $\mathrm{V_{TG}}$, the sample was brought to RT to fully reset the system. The traces in Fig. 7.7 show the $\mathrm{V_{BG}}$ upsweeps subsequent to the initial downsweep. All traces exhibit a linear increase of the density with increasing $\mathrm{V_{BG}}$ before a density saturation sets. For $\mathrm{V_{TG}} > 0$ V (blue and red traces in Fig. 7.7), the saturation density increases significantly compared to $\mathrm{V_{TG}} = 0$ V (black), while $\mathrm{V_{TG}} < 0$ V (olive) reduces the saturation density. In our understanding, $\mathrm{V_{TG}}$ alters the transparency of the triangular-shaped potential barrier between the QW and InAlAs towards the BG. As previously discussed, this barrier governs the saturation density during a $\mathrm{V_{BG}}$ sweep. By applying a positive $\mathrm{V_{TG}}$, the CB edge on the side of the QW towards the TG is shifted downwards. Interestingly, this leads also to a reaction on the opposite side of the QW, where the triangular-shaped potential barrier towards the BG becomes more opaque. As a consequence, tunneling of electrons out of the QW and into the DDLs in the InAlAs towards the BG is significantly hampered. Hence, the evolution of a screening

---

[12] The overshoot contains a InAlAs layer with a maximum indium concentration of 85%. This is the highest indium concentration in InAlAs in the heterostructures, thus providing a energetically favorable layer for electrons.

of the BG electric field is hampered. As a result, more electrons are in the QW when screening sets in compared to $V_{TG} = 0$ V.

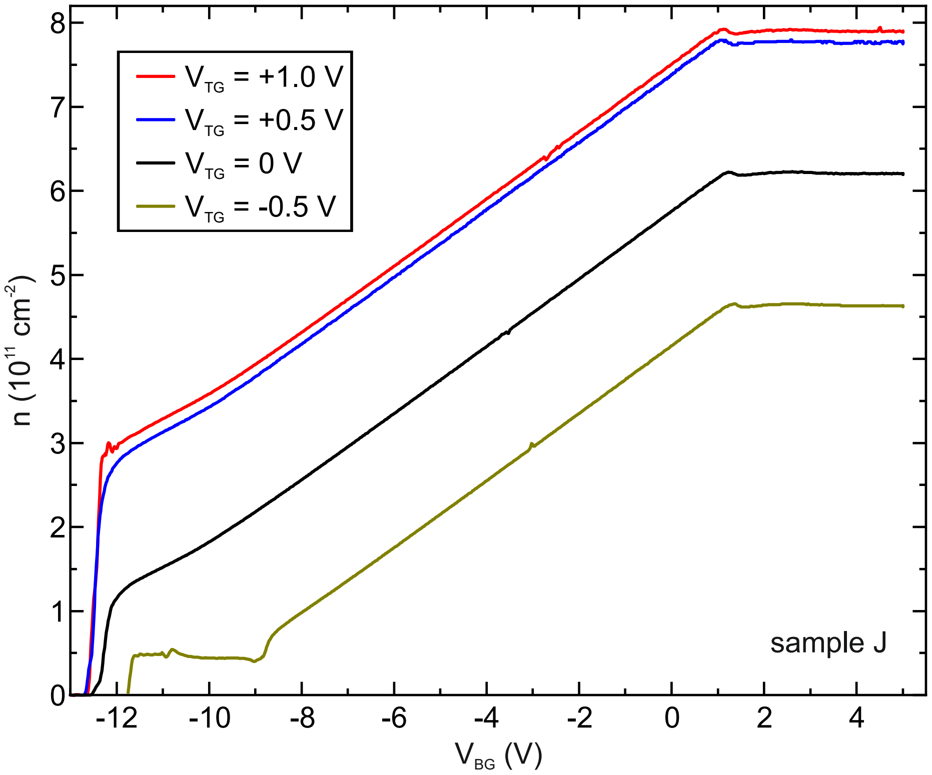

Fig. 7.7: *Electron density n of sample J as a function of a V_{BG} upsweep at different fixed V_{TG}. Between each V_{TG}, the sample was brought to RT to fully reset the system. After each cooldown, a V_{BG} downsweep below MIT was performed.*

When a negative V_{TG} is applied, the CB edge on the side of the QW towards the TG is shifted upwards. This results on the opposite side of the QW to a more transparent triangular-shaped potential barrier towards the BG. Accordingly, electron tunneling out of the QW into the DDLs in the InAlAs towards the BG is enhanced and as a consequence, the saturation density reduces. Note the marginal increase of the saturation density between $V_{TG} = +0.5$ V (blue in Fig. 7.7) and $V_{TG} = +1$ V (red): as we observed in Fig. 7.2(a), sample J is already in regime IV for $V_{TG} > +0.6$ V, which represents a partial screening of the TG electric field. Thus, for $V_{TG} > +0.6$ V, the impact of the TG on the electrostatic configuration is marginal as observed in Fig. 7.7.

7.1.3. Conclusion

In conclusion, we observe a charge transfer over the complete BG gate response. Each adjustment of V_{BG} triggers a charge transfer in the heterostructure, which can traced be back to the DDLs in the InAlAs. Due to the InAlAs on both sides of the QW and the intrinsically present DDLs, electrons can be transferred via multi-step tunneling in both directions, towards the TG and towards the BG, depending on the specific applied voltages at the gate electrodes. We have performed several approaches to prevent the charge transfer (i.e. setting the sample in an electrostatically stable configuration) induced by the V_{BG} with the use of biased-cooldown cycles (similarly to the processes discussed in Sec. 5.2) each for the TG and BG. However, these approaches did not provide configurations in which a stable BG operation was possible. The simple idea of two separate capacitive circuits, as presented in Fig. 7.1(b), does not apply here because of the DDLs in the InAlAs - both circuits mutually impact each other.

7.2. Spin-orbit interaction with two gates

The following section attends the investigation of the Rashba spin-orbit interaction by specifically adjusting the electrostatics within the system via both gate electrodes. We begin our study by an analysis of the evolution of the Rashba parameter extracted from both TG and BG individually.

7.2.1. SOI for separately operated gates

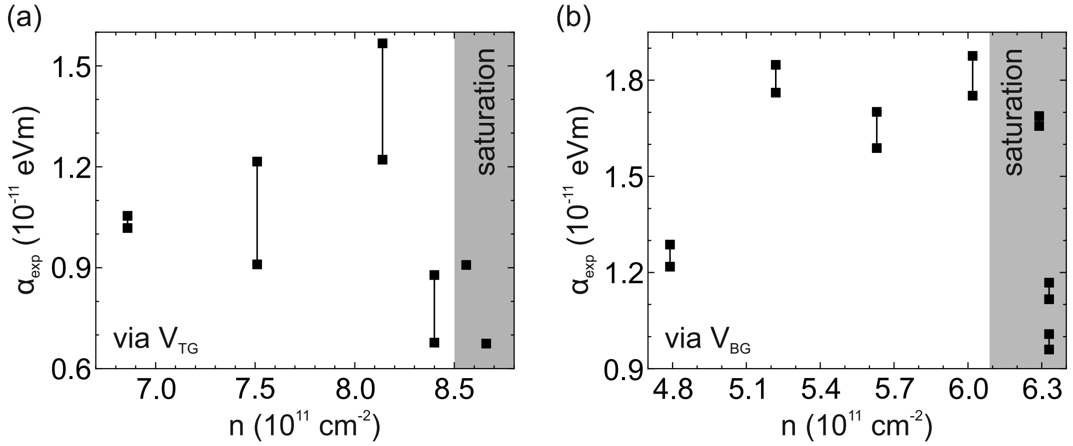

Fig. 7.8: *Rashba parameter α_{exp} of sample J as a function of electron density n extracted from the FFT density analysis of the SOI induced beating patterns for positive and negative magnetic field. (a) n adjusted via V_{TG} with $V_{BG} = 0$ V. (b) n adjusted via V_{BG} with $V_{TG} = 0$ V. The shaded area indicates the saturation regime of the density.*

Fig. 7.8(a) depicts the experimentally extracted Rashba parameter α_{exp} of sample J as a function of the electron density n adjusted via V_{TG} while the BG was kept constant at $V_{BG} = 0$ V. This measurement should be compared to sample G in Fig. 6.9(b), as the heterostructure is, apart from the BG and SiO_x as TG dielectric, identical. α_{exp} decreases with increasing density in a similar density range with extracted values in the same order of magnitude as sample G in Fig. 6.9(b). This shows, that the BG at $V_{BG} = 0$ V as well as the use of SiO_x instead of Al_2O_3 as TG electric has, as we would expect, no significant influence on the Rashba SOI in this heterostructure. In contrast, Fig. 7.8(b) shows α_{exp} of sample J as a function of the electron density n adjusted via V_{BG} while the TG was kept constant at $V_{\mathrm{TG}} = 0$ V. Strikingly, α_{exp} is higher compared to the TG induced α_{exp} values with a peak value at $\alpha_{exp} = 1.88 \times 10^{-11}$ eVm. We do not observe a clear trend of α_{exp} with increasing density - α_{exp} fluctuates. These high values suggest, that the constantly ongoing charge transfer during the BG operation significantly enhances the Rashba SOI in the system similarly to what we discussed in Sec. 6.1.3. Note, that our extracted α_{exp} peak value is among the highest reported in the literature in comparable heterostructures [10, 26, 51, 53, 84–90]. Most interestingly, Grundler [9] reported some of the highest experimentally extracted values in such heterostructures ($\alpha = 4.5 \times 10^{-11}$ eVm) only when a BG electric field is applied additionally to a TG electric field. Only a TG electric field did not result in any beating patterns. Unfortunately, no comment or data was given in this report regarding the gate response of both gate electrodes. This raises the question, in which electrostatic configuration these reported α values were obtained.

The ongoing charge transfer in our heterostructures also explains the fluctuating α_{exp}, as the charge transfer results in a dynamic fluctuation of the electrostatics in the system. Interestingly, with the onset of the density saturation (grey shaded area in Fig. 7.8(b)), α_{exp} decreases down to a minimum value of $\alpha_{exp} = 0.96 \times 10^{-11}$ eVm further within the saturation. Screening of the BG electric field increases when going further within the density saturation. As a consequence, charge transfer should be reduced with ongoing density saturation. The observed decrease of α_{exp} in the density saturation can thus be assigned to this reduced charge transfer resulting in a degraded Rashba SOI.

7.2.2. SOI in a dual-gated operation

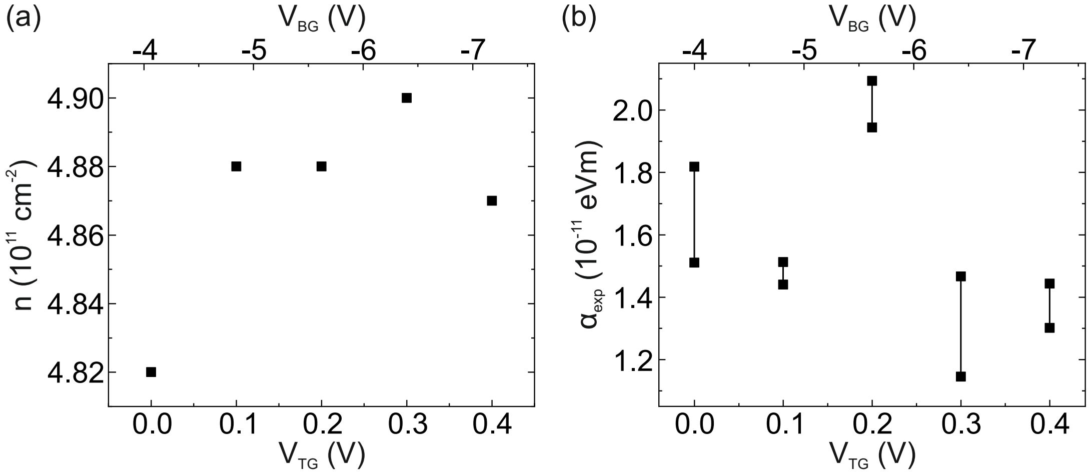

Fig. 7.9: *Electron density n (a) and Rashba parameter α_{exp} (b) of sample J as a function of V_{TG} and V_{BG}. The density is kept constant with appropriately choosing V_{TG} and V_{BG} obeying the ratio of their capacitive coupling constants. Here, gate voltages are set to $V_{\mathrm{TG}} > 0$ V while $V_{\mathrm{BG}} < 0$ V.*

We have characterized the gate response as well as the Rashba SOI of both gate electrodes individually, which allows us to utilize operation of both gates simultaneously. With this, we are able to investigate the Rashba SOI for variable electrostatic configuration while keeping the density constant. We refer to this operation as dual-gating. In order to enhance the electric field in the QW from both gate electrodes, the sign of the applied voltage of each gate has to be opposite. From the gate response characterization in Fig. 7.2(a), we extracted the capacitive coupling constants $c_{\mathrm{TG}} = 3.25\ \mathrm{cm}^{-2}\mathrm{V}^{-1}$ and $c_{\mathrm{BG}} = 0.40\ \mathrm{cm}^{-2}\mathrm{V}^{-1}$, yielding a ratio of 8.1. With this ratio, we can determine the V_{BG} adjustment we have to make to counteract a specific V_{TG}, ultimately keeping the electron density constant. From Fig. 7.2(a), we also extract an operation window, each for the TG and the BG, in which the density can be adjusted linearly to an applied gate voltage before density saturation sets in:

$$\Delta\mathrm{V}_{\mathrm{TG}} : [-1.4\ \mathrm{V};\ +0.8\ \mathrm{V}],$$
$$\Delta\mathrm{V}_{\mathrm{BG}} : [-10.0\ \mathrm{V};\ +0.5\ \mathrm{V}].$$

Thus, we use the largest voltage range for both gates with the condition of opposite signs, to enforce a electric field enhancement in the QW with a constant electron density. This results in a configuration with a starting point $\mathrm{V}_{\mathrm{TG}} = 0$ V and $\mathrm{V}_{\mathrm{BG}} = -4.0$ V yielding $n = 4.8 \times 10^{11}\ \mathrm{cm}^{-2}$. From there, V_{TG} is increased up to $\mathrm{V}_{\mathrm{TG}} = +0.4$ V while V_{BG} is decreased simultaneously down to $\mathrm{V}_{\mathrm{BG}} = -7.24$ V (with the ratio 8.1 from the capacitive coupling constants). Fig. 7.9(a) shows the electron density of sample J as a function of V_{TG} and V_{BG} in this described gate voltage sequence. n varies only marginally between $4.82 - 4.90 \times 10^{11}\ \mathrm{cm}^{-2}$, thus validating our approach for a constant density. For these measurement points, Fig. 7.9(b) depicts the extracted Rashba parameter α_{exp} as a function of V_{TG} and V_{BG} from both magnetic field orientations. The values fluctuate significantly between a minimum at $\alpha_{exp} = 1.15 \times 10^{-11}$ eVm and a maximum value of $\alpha_{exp} = 2.10 \times 10^{-11}$ eVm, exceeding all our samples presented up to here. The fluctuation can be traced back to an ongoing charge transfer due to the BG operation (see Sec. 7.1). The comparably high α_{exp} values would suggest to also origin only from the BG-induced charge transfer. However, most interestingly, SOI-induced beating patterns at the voltages for BG and TG used here, did not result in observable beating patterns when the gates were operated individually - i.e. one was kept at 0 V while the other gate was operated. Also, the maximum and minimum extracted α_{exp} values in dual-gate operation are higher compared to individual operation. This suggests, that an enhancement of the Rashba SOI by dual-gate operation compared to single-gate operation was achieved.

The fluctuation of α_{exp} in Fig. 7.9(b) can also be seen as a decreasing trend when the data points at $\mathrm{V}_{\mathrm{TG}} = +0.2$ V are seen as an outlier. A decreasing trend would fit with the tilting of the bandstructure due to the applied gate voltages. The wavefunction probability density in the QW in this sample J has its maximum towards the substrate, as the comblike-structure is on this substrate-side of the QW (see. Fig. 6.9(a) & (b) and 7.1(a)). The gate configuration here with $\mathrm{V}_{\mathrm{TG}} > 0$ V, while $\mathrm{V}_{\mathrm{BG}} < 0$ V, ultimately tilts the bandstructure downwards in direction from the substrate towards the heterostructure surface. Thus, the maximum of the wavefunction probability density shifts towards the center of the QW and thus, less interfaces within the comb-like inset in the QW overlap (strongly) with the wavefunction probability density. As a consequence, the Rashba SOI decreases as experimentally observed in Fig. 7.9(b).

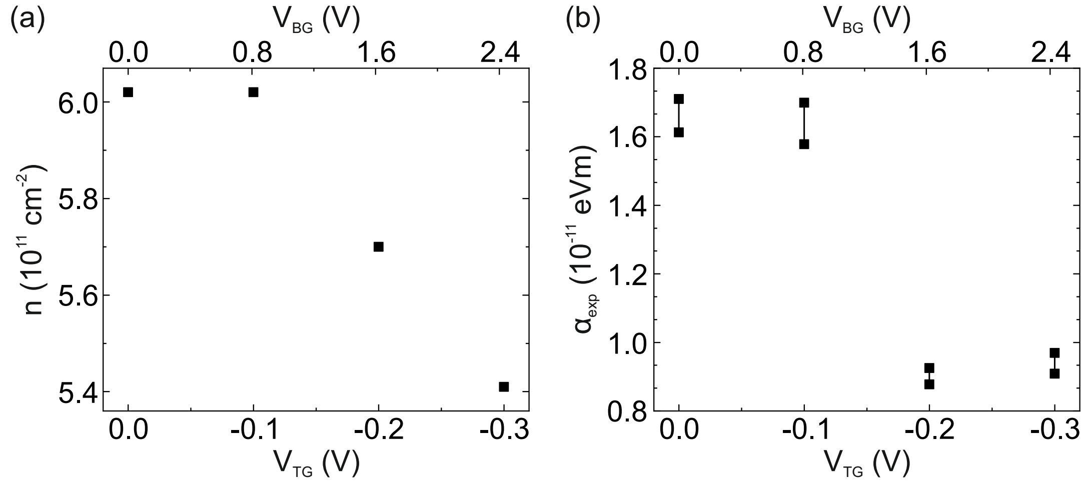

Fig. 7.10: *Electron density n (a) and Rashba parameter α_{exp} (b) of sample J as a function of V_{TG} and V_{BG}. The density is kept constant with appropriately choosing V_{TG} and V_{BG} obeying the ratio of their capacitive coupling constants. Here, gate voltages are set to $V_{\mathrm{TG}} < 0$ V while $V_{\mathrm{BG}} > 0$ V.*

By reversing the signs of both gate voltages, $\mathrm{V_{TG}} < 0$ V while $\mathrm{V_{BG}} > 0$ V, the tilting of the bandstructure changes its direction. As a consequence, the wavefunction probability density should shift more towards the substrate and thus more effectively overlapping the interfaces within the QW. The electron density n of sample J as a function of $\mathrm{V_{TG}}$ and $\mathrm{V_{BG}}$ for this gate configuration is depicted in Fig. 7.10(a). For 0 V $< \mathrm{V_{BG}} < +0.8$ V, the density stays constant at $n = 6.0 \times 10^{11}$ cm^{-2}. With increasing $\mathrm{V_{BG}}$, the density decreases from $n = 6.0 \times 10^{11}$ cm^{-2} to $n = 5.4 \times 10^{11}$ cm^{-2} although $\mathrm{V_{TG}}$ is decreased simultaneously. The density can not be kept constant, as the BG yields a density saturation due to a partial screening for $\mathrm{V_{BG}} > 0.5$ V (see. Sec. 7.1). Thus, from there, the depletion of the TG dominates the gate response while at the same time the BG electric field is screened. This manifests itself also in the analysis of α_{exp} extracted for this configuration, depicted in Fig. 7.10(b): for 0 V $< \mathrm{V_{BG}} < +0.8$ V, α_{exp} is almost constant at $\alpha_{exp} = 1.71 \times 10^{-11}$ eVm. This is comparable to the values extracted from BG operation with $\mathrm{V_{TG}} = 0$ V (see Fig. 7.8(b)), governed by BG-induced charge transfer. Increasing $\mathrm{V_{BG}}$ in Fig. 7.10(b), i.e. the density decreases due to screened BG electric field, α_{exp} decreases significantly to $\alpha_{exp} = 0.88 \times 10^{-11}$ eVm. This is comparable to values extracted from a TG operation with $\mathrm{V_{BG}} = 0$ V (see Fig. 7.8(a)). This suggests, that due to the screened BG electric field, the TG dominates the electrostatic configuration in the system, i.e. it is comparable to individual TG operation, and thus leads to a smaller SOI compared to a dual-gate operation.

7.2.3. Conclusion

In conclusion we observe a strongly enhanced Rashba SOI when the BG is operated while $\mathrm{V_{TG}}$ is kept constant. We assign this to the constantly ongoing charge transfer during BG operation. The situation however changes, when we operate the sample with both gates simultaneously. We observe an increase of the SOI compared to the values of the BG operation while the voltage range in which we observe SOI-induced beating patterns increases significantly. This suggests, that the electric field in the QW is enhanced due to the dual-gate operation. However we observe that the BG-induced charge transfer governs the electrostatics and thus the SOI in this heterostructure.

An approach to minimize (the risk of) charge transfer induced by the BG is to reduce the thickness of the InAlAs between the overshoot of the step-graded buffer and the QW. As this InAlAs barrier exhibits a significant trough due to the intrinsically present DDLs, charge transfer originates due to this layer. By reducing the thickness of this layer, the trough shape should diminish and lead to reduced to vanishing charge transfer (see Sec. 5.5.2). This InAlAs barrier serves as the virtual substrate after the step-graded buffer. Traditionally this layer is chosen to be as large as possible as it separates the QW from the crystal defects in the buffer. However a transmission electron microscope image in Fig. C.1 of a comparable heterostructures (sample A) shows that no defects penetrate through the overshoot into this layer. As a consequence, a thin layer of constant composition InAlAs with the aspired indium concentration should serve perfectly as a virtual substrate while the reduced thickness should strongly reduce a charge transfer during BG operation. In sample J, this InAlAs layer (in combination with the recovery from the overshoot, see Sec. 3.1.2) is $\approx$ 230 nm. From Sec. 5.5.2, we observe a reduction of charge transfer (in TG operation) for 50 nm compared to 130 nm. Thus, we suggest in a first approach to reduce the InAlAs barrier thickness from the QW to the overshoot of the step-graded buffer also to 50 nm.

8. Conclusions and perspective

We investigated two-dimensional electron systems in gated InAlAs-based quantum well heterostructures, as they are considered as a promising platform for spin-orbitronic and computational solid-state applications. This thesis aimed at filling the gap of conducting a systematic study on the connection between the gate response and the heterostructure layout in InAs/InGaAs-based QWs embedded in InAlAs. Our study combined custom-tailored InAlAs-based heterostructures, grown via molecular beam epitaxy, with thorough gate response studies in magnetotransport. The major outcome of our study highlights the key role of intrinsically present deep donor levels in InAlAs barriers. They provide n-type doping, creating two-dimensional electron systems with high electron mobility and well-controllable electron densities. However, at the same time, they govern the gate response and the electrostatics of gated heterostructures - a fact that has not been pointed out in the literature until now.

Within the custom-tailoring of the heterostructures, it turned out that a precise indium growth rate is required. In-situ analysis of RHEED oscillations by growth of InAlAs layers on a GaAs substrate yield a limited range of calibrated rates, while at the same time exhibiting significant statistical error. By also utilizing ex-situ post-growth calibration methods like (S)TEM, SIMS and EDX we were able to increase the range of calibrated indium rates, while at the same time minimizing variation. This allowed us to consistently and reliably adjust the indium concentration across all of the heterostructures used in this thesis.

We have found significant differences in the gate responses in InAlAs-based heterostructures, differing only in the indium concentration in the active layers, in particular between 75% and 81%. Although both heterostructures exhibit a pronounced hysteresis in the gate response, characterized by a maximum density peak and a density saturation, the one with 81% indium offers a smaller available maximum density (4.9×10^{11} cm^{-2} compared to 8.5×10^{11} cm^{-2}), while at the same time an initialization point within the hysteresis loop on a different branch, characterized by metastable control over the electron density. We have developed a phenomenological microscopic model based on our experiments, which allows us to not only explain but also to predict the gate response behavior of these heterostructures. This model is based on a charge transfer of electrons from the 2DES in the QW via the deep donor level states in the InAlAs into the interface with the dielectric and back, resulting in six distinct regimes within the gate response. These regimes can be reproducibly found across all of the heterostructures shown in this thesis, covering different heterostructure layouts. In these regimes we demonstrated the origin of a vanishing capacitive coupling of the gate to the 2DES as well as metastable electrostatic configurations. We have also shown gate operation techniques based on biased-cooling to suppress the metastability and enhance the gate response into stable operation. Although several reports on similarly designed heterostructures can be found in the literature, reported gate responses differ quite significantly from each other. Our model allows to connect the differing gate responses and link them to the heterostructure layout. We emphasize that the DDLs in the InAlAs play a crucial role in the design process of such heterostructures as they govern the electrostatic configuration and reaction of these systems.

The spin-orbit interaction in these InAlAs-based heterostructures is dominated by a Rashba-type SOI and can thus be characterized by the Rashba parameter. As the latter can be separated into contributions from the electric field and the interfaces in the QW, we included an exploration of the question into our study, whether the interface term can be specifically optimized by custom-tailoring the heterostructure. The latter included a systematic variation of the position of an InAs-inset as well as the introduction of multiple insets in an InGaAs QW embedded in InAlAs. The optimization of the interface contribution turned out to be very subtle, because a corresponding heterostructure adjustment always also impacted the internal electric field, often counteracting each other. As the interface contribution turned also out to be small compared to internal electric fields resulting from the heterostructure layout in our heterostructures, this part of the thesis also again points out the key role of the DDLs in the InAlAs on the electrostatics and hence the internal electric fields in the heterostructure. Indeed our developed charge transfer model allowed us to link resulting internal electric fields with the nature of the DDLs in the InAlAs, often governing the outcome of the SOI. An ongoing charge transfer in specific gate response regimes resulted in a significantly increased Rashba parameter as a consequence of the resulting strong variation of the internal electric fields.

As the Rashba parameter can be tuned with an external electric field, we have introduced a backgate to our heterostructure. In combination with the electric field of the topgate, configurations with an enhanced electric field within the QW can be obtained. Over the whole gate response of the backgate, we obtained metastable gate operation, which we have traced back to the DDLs in the InAlAs embedding the QW from both sides and thus governing the dynamics not only in topgate but also in backgate operation. The use of both gates promoted a pronounced charge transfer across the QW in both directions, towards the dielectric and towards the substrate. This charge transfer caused a strongly enhanced SOI similarly to the findings where only a topgate was used. Despite the permanent metastability, we obtained gate voltage regimes where the density could be kept constant while varying the gate electric field. We have found that a charge transfer maintains also in constant density regimes, where it again governs the magnitude of the Rashba-type SOI.

In conclusion we have shown that the deep donor levels, which are intrinsically present in InAlAs, dominantly govern the electrostatics in this popular heterostructure materials platform. Most interestingly, this fact was up until now not reported in the literature. Our systematic study now provides a comprehensive framework for seemingly very different gate responses in such heterostructures. Not only is the overall gate response of a sample affected, but therewith also the Rashba parameter, which characterizes the SOI in the system. Hence, while our study supports the potential of InAlAs-based heterostructures for planar spintronic application concepts, it also clearly demonstrates that the DDLs have to be accounted for in the design process of gated heterostructures.

A. Sample labeling

- Sample A: C200116B
- Sample B: C190515A
- Sample C: C211108B
- Sample D: C211019A
- Sample E: C210601A
- Sample F: C190924A
- Sample G: C210426B
- Sample H: C210615A
- Sample I: C211122A
- Sample J: C210716A

B. InSb and InGaSb in InAs-based QWs

The challenge with the introduction of Sb-based structures within the As-based system is a significant lattice mismatch between InSb and InAs of 9.3%. Due to the already strained growth of InAs on $In_{0.75}Al_{0.25}As$, the addition of Sb-based materials has to be carefully conducted. We estimated the critical thickness of InSb and $In_{0.75}Ga_{0.25}Sb$ on $In_{0.75}Al_{0.25}As$ to be 1.8 nm and 2.2 nm. Based on this, we designed the QW in the heterostructure of a sample I by using only 0.5 nm InSb and 0.5 nm $In_{0.75}Ga_{0.25}Sb$ followed by 5 nm InAs and 5 nm $In_{0.75}Ga_{0.25}As$ (in direction from the surface towards the substrate) embedded in $In_{0.75}Al_{0.25}As$, as depicted in Fig. B.1(a). This allows, in theory, a strained growth within the QW which does not exceed the critical thickness of each of the layers, thus keeping a reasonable electron mobility. The course of the CB edge and the VB edges (black) are depicted in Fig. B.1(b) along with the wavefunction probability density (red). Note, that the transition from $In_{0.75}Al_{0.25}As$ to InSb as well as the transition from $In_{0.75}Ga_{0.25}Sb$ to InAs lead to a crucial band offset in the HH/LH band. Although they add up to each other with different signs, their residual amount (which is positive) of contribution is two orders of magnitude higher compared to all the other transitions. Additionally, for a situation similar to $V_{TG} = 0$ V, the electric field contribution is also positive, thus promoting this specific design as a promising candidate for an enhanced Rashba-type SOI.

Shortly before this thesis was finished, sample I was grown as a first test. During the growth of the two Sb containing layers, the RHEED diffraction pattern suggested a rather poor two-dimensional growth, which was later proven to be right by magnetotransport: The sample exhibits a maximum electron mobility of only $\mu = 1.2 \times 10^4\,\mathrm{cm^2/Vs}$ at $n = 9.9 \times 10^{11}\,\mathrm{cm^{-2}}$ while SdH oscillations are barely visible. This suggests, that the growth parameters for this first test were not ideal, resulting in a crucial amount of crystalline defects at the Sb-based interfaces within the QW. A further investigation of this and similar heterostructure designs is carrying on.

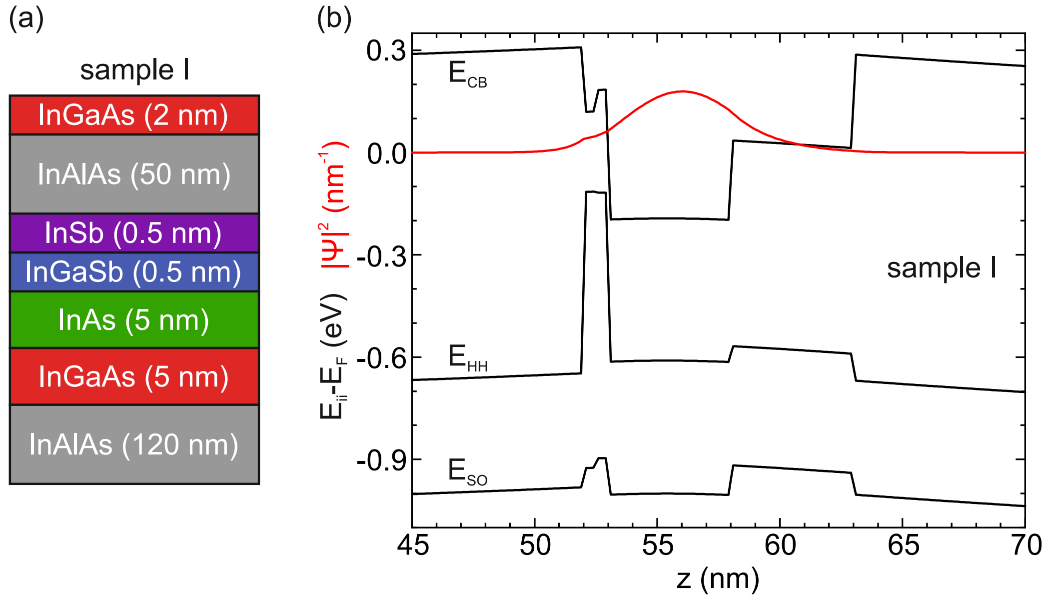

Fig. B.1: *(a) Heterostructure layout of sample I. (b) Band edges of CB and VBs (black) and wavefunction probability density* $|\Psi|^2$ *of the first subband (red) of sample I. The QW consists of thin InSb and* $In_{0.75}Ga_{0.25}Sb$ *layers followed by InAs and* $In_{0.75}Ga_{0.25}As$*, embedded in* $In_{0.75}Al_{0.25}As$*. This design yields crucial bandoffsets at the As-to-Sb-based transitions within the QW and thus to significant interface contributions to the Rashba parameter.*

C. Growth guide for an InAlAs-based step-graded buffer

During the course of this thesis, growth parameters for a step-graded $\mathrm{In}_x\mathrm{Al}_{1-x}\mathrm{As}$ buffer were developed to reliably create 2DES with high electron mobility at reasonable electron densities. In this section we present a short guide for the critical parts during the growth of this buffer.

- III/V ratio: No benefit from using high or low ratios. Typical arsenic beam equivalent pressure (BEP) in our chamber is $6 - 12 \times 10^{-6}$ Torr.
- Aluminum growth rate: constant at 0.6 Å/s. This ensures the indium rate ≤ 4.2Å/s (and thus the indium cell temperature $\leq 900°$C) at a maximum indium concentration 87.5% in the overshoot.
- Starting indium concentration: $5 - 10\%$, no real benefit at a specific value.
- Concentration step width: 5% steps up to 10% before the target concentration in the active layers. From there, steps are reduced to 2.5% up to the maximum in the overshoot.
- Overshoot: As Capotondi *et al.* [58] reported, an overshoot in the step-graded buffer significantly enhances the electron mobility in the 2DES. We recommend to take the overshoot to 10% above the target concentration, similarly to Capotondi. However

for target concentrations $> 75\%$, we observed no benefit for a overshoot maximum $> 87.5\%$.

- Recovery to target concentration: This is done in a single step back from the overshoot maximum to the target concentration. As the indium cell temperature ramps with 9°C/min, the concentration declines linearly. The resulting decline of the rate is then sufficient.

- Step thickness: 50 nm is traditionally used and what we also recommend.
  However, a strict pre-definition of the thickness is not feasible due to the adjustment of the rate with the cell temperature and the definition of a growth time for a specific thickness: The thickness for each buffer layer is defined via the growth time assuming the rate of the final concentration. This is with no significant consequence for $\mathrm{In}_x\mathrm{Al}_{1-x}\mathrm{As}$ layers below 70% (i.e. rates ≤ 2.0 Å/s with 0.6 Å/s for Al and 1.4 Å/s) as the temperature steps of the indium cell are sufficiently small to ensure ≥ 30 nm constant composition thickness in the step after the rate adjustment for the given time for 50 nm. For $\mathrm{In}_x\mathrm{Al}_{1-x}\mathrm{As}$ layers above 70%, temperature steps are bigger and overall rates are higher, hence reducing the growth time for otherwise predefined 50 nm width significantly. As a consequence, there would be no sufficiently thick constant composition layer in this step after the rate adjustment as latter takes almost the full growth time. Thus, we set a minimum growth time of 250 s for layers with $> 70\%$. SIMS analysis of our buffer structures reveal that only the rate adjustment in these layers covers already ≈ 60 nm.

- Substrate Temperature: $320°\mathrm{C} < \mathrm{T}_{substrate} < 345°\mathrm{C}$. Ideally at $\mathrm{T}_{substrate} = 335°\mathrm{C}$. The temperature should be kept constant during the steps as well as during the rate recovery after the overshoot. A fast temperature increase already during the recovery significantly increases the risk of crystalline defects piercing through into the active layers. The recovery takes about 180 s (corresponds to ≈ 70 nm).

These parameters ensure the growth of a step-graded buffer, in which abrupt step-interfaces are created. As a consequence of these interfaces, crystalline defects arising from the lattice mismatch in each step are confined within the steps and thus do not pierce through the buffer and into the active layers of the heterostructure. The transmission electron microscope (TEM) image of one of our structures depicted in Fig. C.1 shows exactly this. The resolution allows to identify each of the steps in the buffer. Crystalline defects penetrate into the beginning of the overshoot, in which they disappear up to the maximum. Thus, the recovery layer to the constant composition layer (virtual substrate) and following the active layers with the QW are (at least visually) defect-free.

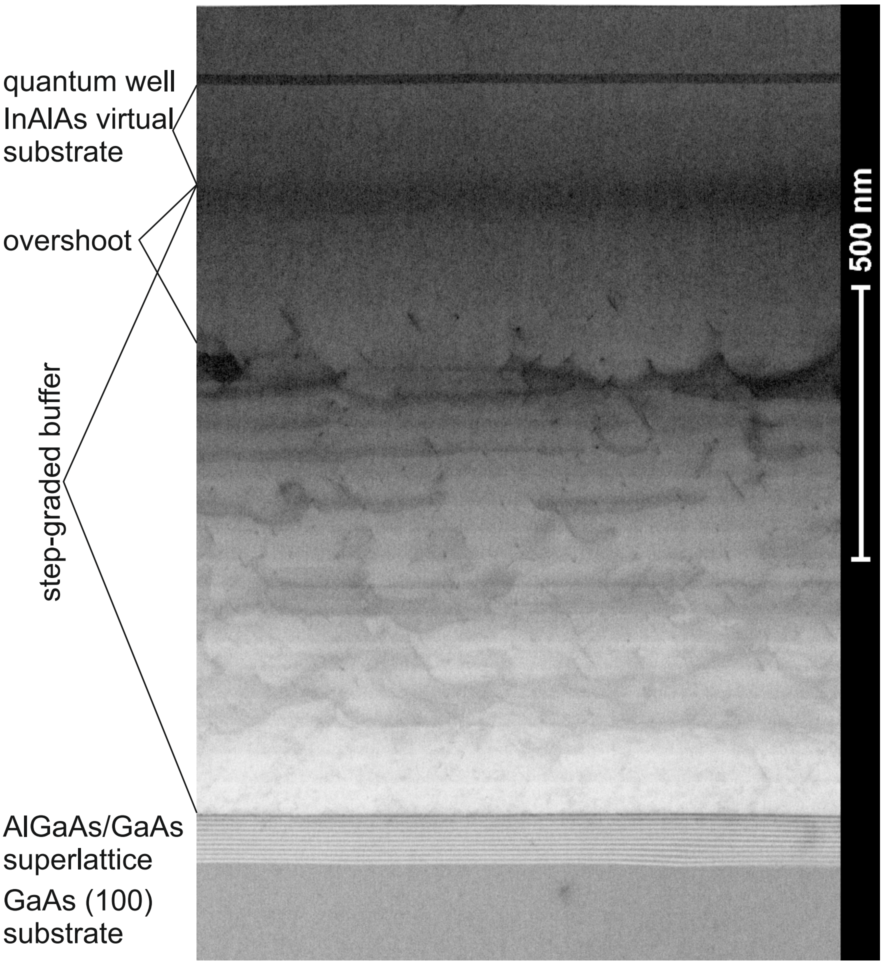

Fig. C.1: *Transmission electron microscope image of sample A. Crystal defects are created in the step-graded buffer due to the lattice mismatch. These defects do not penetrate through the overshoot into the InAlAs virtual substrate.*

D. Fabrication recipes

All the samples in this work have been fabricated in a Hall bar geometry. Starting point for the samples is a 2-inch wafer. With a tungsten carbide needle, the wafer is scribed along high symmetry cleaving directions and pieces with a size of 4.5 mm × 4.5 mm are cleaved. If the wafer was glued with liquid gallium to the substrate holder from the MBE, the residual gallium on the backside is removed with hydrochloric acid (HCl) and a prior cleaning in acetone and isopropanol. The following fabrication steps require cleanroom ambience.

Defining the mesa:

- Standard cleaning: $\geq$ 60 s Acetone (Ac) in ultrasonic bath, $\geq$ 2 min Ac, $\geq$ 2 min isopropanol (Prop), blow-dry with N_2

- Spin resist S1813: 30 s, 2000 rpm/s, 8000 rpm
- Softbake 4 min at 90°C
- Exposure with mesa mask 4 min at 275 W lamp power (time depends strongly on the condition of the lamp)
- Develop in MF26-A 45 s with flea 200 rpm, rinse 10 s in ultrapure water (UPW)
- Check developed mesa in microscope (yellow filter!)
- Etching: $C_6H_8O_7 : H_2O : H_2O_2$ (30%) : H_3PO_4 (98%) $= 22 : 88 : 2 : 1.2$, etch rate ≈ 0.75 nm/s, rinse 10s in UPW (etch depth ≥ 50 nm below QW or doping layer)
- Lift-off in Ac, Ac, Prop (see also standard cleaning)
- Check for properly defined mesa in microscope and profilometer

Ohmic contacts:

- Standard cleaning Remover PG (RPG), RPG, Prop
- Prebake ≥ 5 min at 120°C
- Spin resist LOR 3A: 45 s, 2000 rpm/s, 4000 rpm
- Softbake 4 min at 120°C
- Spin resist S1813: 30 s, 2000 rpm/s, 8000 rpm
- Softbake 4 min at 90°C
- Exposure with contact mask 5 : 30 min at 275 W lamp power (time depends strongly on the condition of the lamp)
- Develop in MF26-A 45 s with flea 200 rpm, rinsing 10 s in UPW
- Check developed contact windows in microscope (yellow filter!)
- Oxide removal with HCl-Dip H_2O : HCl (37%) $= 1 : 1$ 60 s, rinse 10 s in UPW
- Evaporation of 260 nm AuGe (88%/12%) and 66 nm Ni
- Lift-off in RPG (60°C) ≥ 20 min, RPG, Prop
- Check for properly defined contacts in microscope
- Forming-gas-assisted annealing: 10 mbar, 350°C 120 s, 450°C 75 s

Dielectric:

- Standard cleaning Ac, Ac Prop
- Oxide removal with HCl-Dip H_2O : HCl (37%) = 1 : 1 60 s, rinse 10 s in UPW
- Al_2O_3: via atomic layer deposition (ALD), 0.1 nm/cycle, $T = 300°C$, 20 sccm N_2 flow, 0.015 s pulse time, 4 s purge time
- SiO_x: via plasma-enhanced chemical vapor deposition (PECVD), SiH_4 and N_2O, 10 nm in 15 s, max. 30 nm at one ignited plasma, $T = 350°C$
- Standard cleaning Ac, Ac, Prop (no ultrasonic!)

Metallic topgate:

- Standard cleaning Ac, Ac, Prop (no ultrasonic!)
- Spin resist S1813: 30 s, 2000 rpm/s, 8000 rpm
- Softbake 4 min at 90°C
- Exposure with topgate mask 4 min at 275 W lamp power (time depends strongly on the condition of the lamp)
- Develop in MF26-A 45 s with flea 200 rpm, rinse 10 s in UPW
- Check developed topgate mask in microscope (yellow filter!)
- Evaporation of 10 nm Ti and 100 nm Au
- Lift-off in Ac (60°C) $\geq$ 1 h or better overnight, Ac (short ultrasonic pulses if necessary), Prop
- Check for properly defined topgate in microscope

Mounting in Chipcarrier:

- Standard cleaning of sample with Ac, Ac, Prop (no ultrasonic!)
- Standard cleaning of chipcarrier with Ac, Ac, Prop
- Only topgate: glue with polymethyl methacrylate (PMMA) resist, bake $\geq$ 10 min at 60°C
- With backgate: glue with silver conductive paint, bake $\geq$ 90 min at 100°C

References

1. Žutić, I., Fabian, J. & Das Sarma, S. Spintronics: Fundamentals and applications. *Rev. Mod. Phys.* **76,** 323 (2004).
2. Arute, F., Arya, K., Babbush, R., Bacon, D., Bardin, J. C., Barends, R., Biswas, R., Boixo, S., Brandao, F. G. S. L., Buell, D. A., Burkett, B., Chen, Y., Chen, Z., Chiaro, B., Collins, R., Courtney, W., Dunsworth, A., Farhi, E., Foxen, B., Fowler, A., Gidney, C., Giustina, M., Graff, R., Guerin, K., Habegger, S., Harrigan, M. P., Hartmann, M. J., Ho, A., Hoffmann, M., Huang, T., Humble, T. S., Isakov, S. V., Jeffrey, E., Jiang, Z., Kafri, D., Kechedzhi, K., Kelly, J., Klimov, P. V., Knysh, S., Korotkov, A., Kostritsa, F., Landhuis, D., Lindmark, M., Lucero, E., Lyakh, D., Mandrà, S., McClean, J. R., McEwen, M., Megrant, A., Mi, X., Michielsen, K., Mohseni, M., Mutus, J., Naaman, O., Neeley, M., Neill, C., Niu, M. Y., Ostby, E., Petukhov, A., Platt, J. C., Quintana, C., Rieffel, E. G., Roushan, P., Rubin, N. C., Sank, D., Satzinger, K. J., Smelyanskiy, V., Sung, K. J., Trevithick, M. D., Vainsencher, A., Villalonga, B., White, T., Yao, Z. J., Yeh, P., Zalcman, A., Neven, H. & Martinis, J. M. Quantum supremacy using a programmable superconducting processor. *Nature* **574,** 505 (2019).
3. Loss, D. & DiVincenzo, D. P. Quantum computation with quantum dots. *Phys. Rev. A* **57,** 120 (1998).
4. Das Sarma, S., Freedman, M. & Nayak, C. Topological quantum computation. *Phys. Today* **59,** 32 (2006).
5. Shabani, J., Kjaergaard, M., Suominen, H. J., Kim, Y., Nichele, F., Pakrouski, K., Stankevic, T., Lutchyn, R. M., Krogstrup, P., Feidenhans'l, R., Kraemer, S., Nayak, C., Troyer, M., Marcus, C. M. & Palmstrøm, C. J. Two-dimensional epitaxial superconductor-semiconductor heterostructures: A platform for topological superconducting networks. *Phys. Rev. B* **93,** 155402 (2016).
6. Datta, S. & Das, B. Electronic analog of the electro-optic modulator. *Appl. Phys. Lett.* **56,** 665 (1990).
7. Dresselhaus, G. Spin-Orbit Coupling Effects in Zinc Blende Structures. *Phys. Rev.* **100,** 580 (1955).
8. Bychkov, Y. A. & Rashba, E. I. Oscillatory effects and the magnetic susceptibility of carriers in inversion layers. *J. Phys. C: Solid State Phys.* **17,** 6039 (1984).
9. Grundler, D. Large Rashba Splitting in InAs Quantum Wells due to Electron Wave Function Penetration into the Barrier Layers. *Phys. Rev. Lett.* **84,** 6074 (2000).
10. Nitta, J., Akazaki, T., Takayanagi, H. & Enoki, T. Gate Control of Spin-Orbit Interaction in an Inverted $\mathrm{In_{0.53}Ga_{0.47}As/In_{0.52}Al_{0.48}As}$ Heterostructure. *Phys. Rev. Lett.* **78,** 1335 (1997).
11. Choi, H., Kakegawa, T., Akabori, M., Suzuki, T. & Yamada, S. Spin–orbit interactions in high In-content InGaAs/InAlAs inverted heterojunctions for Rashba spintronic devices. *Phys. E: Low-Dimens. Syst. Nanostructures* **40,** 2823 (2008).

12. Kohda, M., Lechner, V., Kunihashi, Y., Dollinger, T., Olbrich, P., Schönhuber, C., Caspers, I., Bel'kov, V. V., Golub, L. E., Weiss, D., Richter, K., Nitta, J. & Ganichev, S. D. Gate-controlled persistent spin helix state in (In,Ga)As quantum wells. *Phys. Rev. B* **86,** 081306(R) (2012).

13. Holmes, S. N., Simmonds, P. J., Beere, H. E., Sfigakis, F., Farrer, I., Ritchie, D. A. & Pepper, M. Bychkov-Rashba dominated band structure in an $In_{0.75}Ga_{0.25}As$-$In_{0.75}Al_{0.25}As$ device with spin-split carrier densities of $< 10^{11}$ cm^{-2}. *J. Phys. Condens. Matter* **20,** 472207 (2008).

14. Nitta, J., Bergsten, T., Kunihashi, Y. & Kohda, M. Electrical manipulation of spins in the Rashba two dimensional electron gas systems. *J. Appl. Phys.* **105,** 122402 (2009).

15. Simmonds, P. J., Holmes, S. N., Beere, H. E., Farrer, I., Sfigakis, F., Ritchie, D. A. & Pepper, M. Molecular beam epitaxy of high mobility $In_{0.75}Ga_{0.25}As$ for electron spin transport applications. *J. Vac. Sci. Technol., B* **27,** 2066 (2009).

16. Kunihashi, Y., Kohda, M. & Nitta, J. Enhancement of Rashba Spin–Orbit Interaction Due to Wave Function Engineering. *J. Supercond. Nov. Magn.* **23,** 49 (2009).

17. Manchon, A., Koo, H. C., Nitta, J., Frolov, S. M. & Duine, R. A. New perspectives for Rashba spin-orbit coupling. *Nat. Mater.* **14,** 871 (2015).

18. Chuang, P., Ho, S.-C., Smith, L. W., Sfigakis, F., Pepper, M., Chen, C.-H., Fan, J.-C., Griffiths, J. P., Farrer, I., Beere, H. E., Jones, G. A. C., Ritchie, D. A. & Chen, T.-M. All-electric all-semiconductor spin field-effect transistors. *Nat. Nanotechnol.* **10,** 35 (2015).

19. Suominen, H. J., Kjaergaard, M., Hamilton, A. R., Shabani, J., Palmstrøm, C. J., Marcus, C. M. & Nichele, F. Zero-Energy Modes from Coalescing Andreev States in a Two-Dimensional Semiconductor-Superconductor Hybrid Platform. *Phys. Rev. Lett.* **119,** 176805 (2017).

20. Lee, J. S., Shojaei, B., Pendharkar, M., McFadden, A. P., Kim, Y., Suominen, H. J., Kjaergaard, M., Nichele, F., Zhang, H., Marcus, C. M. & Palmstrøm, C. J. Transport Studies of Epi-Al/InAs Two-Dimensional Electron Gas Systems for Required Building-Blocks in Topological Superconductor Networks. *Nano Lett.* **19,** 3083 (2019).

21. Fornieri, A., Whiticar, A. M., Setiawan, F., Portolés, E., Drachmann, A. C. C., Keselman, A., Gronin, S., Thomas, C., Wang, T., Kallaher, R., Gardner, G. C., Berg, E., Manfra, M. J., Stern, A., Marcus, C. M. & Nichele, F. Evidence of topological superconductivity in planar Josephson junctions. *Nature* **569,** 89 (2019).

22. Frolov, S. M., Manfra, M. J. & Sau, J. D. Topological superconductivity in hybrid devices. *Nat. Phys.* **16,** 718 (2020).

23. Capotondi, F., Biasiol, G., Ercolani, D. & Sorba, L. Scattering mechanisms in undoped $In_{0.75}Ga_{0.25}As/In_{0.75}Al_{0.25}As$ two-dimensional electron gases. *J. Cryst. Growth* **278,** 538 (2005).

24. Chen, C., Farrer, I., Holmes, S. N., Sfigakis, F., Fletcher, M. P., Beere, H. E. & Ritchie, D. A. Growth variations and scattering mechanisms in metamorphic $\mathrm{In_{0.75}Ga_{0.25}As/In_{0.75}Al_{0.25}As}$ quantum wells grown by molecular beam epitaxy. *J. Cryst. Growth* **425,** 70 (2015).

25. Desrat, W., Giazotto, F., Pellegrini, V., Beltram, F., Capotondi, F., Biasiol, G., Sorba, L. & Maude, D. K. Magnetotransport in high-g-factor low-density two-dimensional electron systems confined in $\mathrm{In_{0.75}Ga_{0.25}As/In_{0.75}Al_{0.25}As}$ quantum wells. *Phys. Rev. B* **69,** 245324 (2004).

26. Hatke, A. T., Wang, T., Thomas, C., Gardner, G. C. & Manfra, M. J. Mobility in excess of 10^6 $\mathrm{cm^2/Vs}$ in InAs quantum wells grown on lattice mismatched InP substrates. *Appl. Phys. Lett.* **111,** 142106 (2017).

27. Richter, A., Koch, M., Matsuyama, T., Heyn, C. & Merkt, U. Transport properties of modulation-doped InAs-inserted-channel $\mathrm{In_{0.75}Al_{0.25}As/In_{0.75}Ga_{0.25}As}$ structures grown on GaAs substrates. *Appl. Phys. Lett.* **77,** 3227 (2000).

28. Shabani, J., Das Sarma, S. & Palmstrøm, C. J. An apparent metal-insulator transition in high-mobility two-dimensional InAs heterostructures. *Phys. Rev. B* **90,** 161303(R) (2014).

29. Shabani, J., McFadden, A. P., Shojaei, B. & Palmstrøm, C. J. Gating of high-mobility InAs metamorphic heterostructures. *Appl. Phys. Lett.* **105,** 262105 (2014).

30. Ihn, T. *Semiconductor Nanostructures: Quantum states and electronic transport* ISBN: 9780199534425 (Oxford University Press, 2009).

31. Drude, P. Zur Elektronentheorie der Metalle. *Ann. Phys.* **306,** 566 (1900).

32. Coleridge, P. T., Stoner, R. & Fletcher, R. Low-field transport coefficients in $\mathrm{GaAs/Ga}_{1-x}\mathrm{Al}_1\mathrm{As}$ heterostructures. *Phys. Rev. B* **39,** 1120 (1989).

33. Das Sarma, S. & Stern, F. Single-particle relaxation time versus scattering time in an impure electron gas. *Phys. Rev. B* **32,** 8442 (1985).

34. V. Klitzing, K., Dorda, G. & Pepper, M. New Method for High-Accuracy Determination of the Fine-Structure Constant Based on Quantized Hall Resistance. *Phys. Rev. Lett.* **45,** 494 (1980).

35. Prange, R. E. Quantized Hall resistance and the measurement of the fine-structure constant. *Phys. Rev. B* **23,** 4802 (1981).

36. Büttiker, M. Absence of backscattering in the quantum Hall effect in multiprobe conductors. *Phys. Rev. B* **38,** 9375 (1988).

37. Winkler, R. *Spin-orbit Coupling Effects in Two-Dimensional Electron and Hole Systems* ISBN: 9783540011873 (Springer Berlin, Heidelberg, 2003).

38. Raikh, M. E. & Shahbazyan, T. V. Magnetointersubband oscillations of conductivity in a two-dimensional electronic system. *Phys. Rev. B* **49,** 5531 (1994).

39. Coleridge, P. T. Inter-subband scattering in a 2D electron gas. *Semicond. Sci. Technol.* **5,** 961 (1990).

40. Leadley, D. R., Fletcher, R., Nicholas, R. J., Tao, F., Foxon, C. T. & Harris, J. J. Intersubband resonant scattering in GaAs-$Ga_{1-x}Al_xAs$ heterojunctions. *Phys. Rev. B* **46,** 12439 (1992).
41. Bergmann, G. Physical interpretation of weak localization: A time-of-flight experiment with conduction electrons. *Phys. Rev. B* **28,** 2914 (1983).
42. Ganichev, S. D. & Golub, L. E. Interplay of Rashba/Dresselhaus spin splittings probed by photogalvanic spectroscopy -A review. *Phys. Status Solidi B* **251,** 1801 (2014).
43. Cardona, M., Christensen, N. E. & Fasol, G. Relativistic band structure and spin-orbit splitting of zinc-blende-type semiconductors. *Phys. Rev. B* **38,** 1806 (1988).
44. Schäpers, T. *Semiconductor Spintronics* ISBN: 9783110425444 (De Gruyter, 2016).
45. Rashba, E. I. Properties of semiconductors with an extremum loop. I. Cyclotron and combinational resonance in a magnetic field perpendicular to the plane of the loop. *Sov. Phys. Solid State* **2,** 1109 (1960).
46. Zhai, Y., Baniya, S., Zhang, C., Li, J., Haney, P., Sheng, C.-X., Ehrenfreund, E. & Vardeny, Z. V. Giant Rashba splitting in 2D organic-inorganic halide perovskites measured by transient spectroscopies. *Sci. Adv.* **3,** e1700704 (2017).
47. Hvazdouski, D. C., Baranava, M. S. & Stempitsky, V. R. Spin splitting in band structures of BiTeX (X = Cl, Br, I) monolayers. *IOP Conf. Ser.: Mater. Sci. Eng.* **347,** 012017 (2018).
48. Wu, K., Chen, J., Ma, H., Wan, L., Hu, W. & Yang, J. Two-Dimensional Giant Tunable Rashba Semiconductors with Two-Atom-Thick Buckled Honeycomb Structure. *Nano Lett.* **21,** 740 (2021).
49. Lommer, G., Malcher, F. & Rossler, U. Spin splitting in semiconductor heterostructures for B→ 0. *Phys. Rev. Lett.* **60,** 728 (1988).
50. Luo, J., Munekata, H., Fang, F. F. & Stiles, P. J. Effects of inversion asymmetry on electron energy band structures in GaSb/InAs/GaSb quantum wells. *Phys. Rev. B* **41,** 7685 (1990).
51. Schäpers, T., Engels, G., Lange, J., Klocke, T., Hollfelder, M. & Lüth, H. Effect of the heterointerface on the spin splitting in modulation doped $In_xGa_{1-x}As$/InP quantum wells for B→ 0. *J. Appl. Phys.* **83,** 4324 (1998).
52. Faniel, S., Matsuura, T., Mineshige, S., Sekine, Y. & Koga, T. Determination of spin-orbit coefficients in semiconductor quantum wells. *Phys. Rev. B* **83,** 115309 (2011).
53. Engels, G., Lange, J., Schäpers, T. & Lüth, H. Experimental and theoretical approach to spin splitting in modulation-doped $In_xGa_{1-x}As$/InP quantum wells for B→ 0. *Phys. Rev. B* **55,** R1958 (1997).
54. Bergmann, G. Weak anti-localization - An experimental proof for the destructive interference of rotated spin 12. *Solid State Commun.* **42,** 815 (1982).

55. Inoue, K., Harmand, J. & Matsuno, T. High-quality $In_xGa_{1-x}As$/InAlAs modulation-doped heterostructures grown lattice-mismatched on GaAs substrates. *J. Cryst. Growth* **111,** 313 (1991).

56. Gozu, S.-i., Kita, T., Sato, Y., Yamada, S. & Tomizawa, M. Characterization of high indium content metamorphic InGaAs/InAlAs modulation-doped heterostructures. *J. Cryst. Growth* **227,** 155 (2001).

57. Capotondi, F., Biasiol, G., Vobornik, I., Sorba, L., Giazotto, F., Cavallini, A. & Fraboni, B. Two-dimensional electron gas formation in undoped $In_{0.75}Ga_{0.25}As$/ $In_{0.75}Al_{0.25}As$ quantum wells. *J. Vac. Sci. Technol. B* **22,** 702 (2004).

58. Capotondi, F., Biasiol, G., Ercolani, D., Grillo, V., Carlino, E., Romanato, F. & Sorba, L. Strain induced effects on the transport properties of metamorphic InAlAs/InGaAs quantum wells. *Thin Solid Films* **484,** 400 (2005).

59. Romanato, F., Napolitani, E., Carnera, A., Drigo, A. V., Lazzarini, L., Salviati, G., Ferrari, C., Bosacchi, A. & Franchi, S. Strain relaxation in graded composition $In_xGa_{1-x}As$/GaAs buffer layers. *J. Appl. Phys.* **86,** 4748 (1999).

60. Löhr, S., Mendach, S., Vonau, T., Heyn, C. & Hansen, W. Highly anisotropic electron transport in shallow InGaAs heterostructures. *Phys. Rev. B* **67,** 045309 (2003).

61. Ercolani, D., Biasiol, G., Cancellieri, E., Rosini, M., Jacoboni, C., Carillo, F., Heun, S., Sorba, L. & Nolting, F. Transport anisotropy in $In_{0.75}Ga_{0.25}As$ two-dimensional electron gases induced by indium concentration modulation. *Phys. Rev. B* **77,** 235307 (2008).

62. Jiang, Z., Wang, W., Gao, H., Liu, L., Chen, H. & Zhou, J. Strain relaxation and surface morphology of high indium content InAlAs metamorphic buffers with reverse step. *Appl. Surf. Sci.* **254,** 5241 (2008).

63. Loher, J. *Two-dimensional hole systems in indium-based quantum well heterostructures* Universität Regensburg. 2016.

64. Ebnet, L. *Untersuchung der Spin-Bahn-Kopplung in maßgeschneiderten InGaAs/ InAlAs-Heterostrukturen* Universität Regensburg. 2022.

65. Prager, M., Trottmann, M., Schmidt, J., Ebnet, L., Schuh, D. & Bougeard, D. Gating of Two-Dimensional Electron Systems in (In, Ga)As/(In, Al)As Heterostructures: The Role of Intrinsic (In, Al)As Deep Donor Defects. *Phys. Rev. Appl.* **16,** 064028 (2021).

66. Vurgaftman, I., Meyer, J. R. & Ram-Mohan, L. R. Band parameters for III–V compound semiconductors and their alloys. *J. Appl. Phys.* **89,** 5815 (2001).

67. Trottmann, M. *Characterisation of III-V semiconductor hybrid systems for spinorbitronic functionality* Universität Regensburg. 2020.

68. Choi, M., Janotti, A. & van de Walle, C. G. Native point defects and dangling bonds in α-Al_2O_3. *J. Appl. Phys.* **113,** 044501 (2013).

69. Hoshii, T., Lee, S., Suzuki, R., Taoka, N., Yokoyama, M., Yamada, H., Hata, M., Yasuda, T., Takenaka, M. & Takagi, S. Reduction in interface state density of Al_2O_3/InGaAs metal-oxide-semiconductor interfaces by InGaAs surface nitridation. *J. Appl. Phys.* **112,** 073702 (2012).

70. Lin, L. & Robertson, J. Defect states at III-V semiconductor oxide interfaces. *Appl. Phys. Lett.* **98,** 082903 (2011).

71. Lin, L. & Robertson, J. Passivation of interfacial defects at III-V oxide interfaces. *J. Vac. Sci. Technol. B* **30,** 04E101 (2012).

72. Robertson, J. Model of interface states at III-V oxide interfaces. *Appl. Phys. Lett.* **94,** 152104 (2009).

73. Taoka, N., Yokoyama, M., Hyeon Kim, S., Suzuki, R., Lee, S., Iida, R., Hoshii, T., Jevasuwan, W., Maeda, T., Yasuda, T., Ichikawa, O., Fukuhara, N., Hata, M., Takenaka, M. & Takagi, S. Impact of Fermi level pinning inside conduction band on electron mobility of $In_xGa_{1-x}As$ MOSFETs and mobility enhancement by pinning modulation. *Appl. Phys. Lett.* **103,** 143509 (2013).

74. Wang, W., Hinkle, C. L., Vogel, E. M., Cho, K. & Wallace, R. M. Is interfacial chemistry correlated to gap states for high-k/III–V interfaces? *Microelectron. Eng.* **88,** 1061 (2011).

75. Ahn, J., Kent, T., Chagarov, E., Tang, K., Kummel, A. C. & McIntyre, P. C. Arsenic decapping and pre-atomic layer deposition trimethylaluminum passivation of Al_2O_3/InGaAs(100) interfaces. *Appl. Phys. Lett.* **103,** 071602 (2013).

76. Hinkle, C., Milojevic, M., Sonnet, A., Kim, H., Kim, J., Vogel, E. M. & Wallace, R. M. Surface Studies of III-V Materials: Oxidation Control and Device Implications. *ECS Trans.* **19,** 387 (2009).

77. Huang, M. L., Chang, Y. C., Chang, C. H., Lee, Y. J., Chang, P., Kwo, J., Wu, T. B. & Hong, M. Surface passivation of III-V compound semiconductors using atomic-layer-deposition-grown Al_2O_3. *Appl. Phys. Lett.* **87,** 252104 (2005).

78. McIntyre, P. C., Oshima, Y., Kim, E. & Saraswat, K. C. Interface studies of ALD-grown metal oxide insulators on Ge and III–V semiconductors. *Microelectron. Eng.* **86,** 1536 (2009).

79. Milojevic, M., Aguirre-Tostado, F. S., Hinkle, C. L., Kim, H. C., Vogel, E. M., Kim, J. & Wallace, R. M. Half-cycle atomic layer deposition reaction studies of Al_2O_3 on $In_{0.2}Ga_{0.8}As$ (100) surfaces. *Appl. Phys. Lett.* **93,** 202902 (2008).

80. Park, M.-S., Razaei, M., Barnhart, K., Tan, C. L. & Mohseni, H. Surface passivation and aging of InGaAs/InP heterojunction phototransistors. *J. Appl. Phys.* **121,** 233105 (2017).

81. Shahrjerdi, D., Tutuc, E. & Banerjee, S. K. Impact of surface chemical treatment on capacitance-voltage characteristics of GaAs metal-oxide-semiconductor capacitors with Al_2O_3 gate dielectric. *Appl. Phys. Lett.* **91,** 063501 (2007).

82. Timm, R., Fian, A., Hjort, M., Thelander, C., Lind, E., Andersen, J. N., Wernersson, L.-E. & Mikkelsen, A. Reduction of native oxides on InAs by atomic layer deposited Al_2O_3 and HfO_2. *Appl. Phys. Lett.* **97,** 132904 (2010).

83. Schmidt, J. *Controlling the gating behavior in high indium-content heterostructures for spin-orbitronic application* Universität Regensburg. 2021.

84. Kohda, M., Shibata, T. & Nitta, J. Spin-Orbit Interaction in an $In_{0.53}Ga_{0.47}As$ / $In_{0.7}Ga_{0.3}As$ Shallow Two-Dimensional Electron Gas Located 5 nm below InP Surface Barrier. *Jpn. J. Appl. Phys.* **49,** 04DM02 (2010).

85. Ho Park, Y., Kim, H.-j., Chang, J., Hee Han, S., Eom, J., Choi, H.-J. & Cheol Koo, H. Separation of Rashba and Dresselhaus spin-orbit interactions using crystal direction dependent transport measurements. *Appl. Phys. Lett.* **103,** 252407 (2013).

86. Nitta, J., Akazaki, T., Takayanagi, H. & Enoki, T. Gate Control of spin-orbit interaction in an InAs-inserted $In_{0.53}Ga_{0.47}As/In_{0.52}Al_{0.48}As$ heterostructure. *Phys. E: Low-Dimens. Syst. Nanostructures* **2,** 527 (1998).

87. Kim, K.-H., Park, Y. H., Koo, H. C., Chang, J., Kim, Y. K. & Kim, H.-J. Gate-Controlled Spin-Orbit Coupling in InAs/InGaAs Quantum Well Structures. *J. Nanosci. Nanotechnol.* **14,** 5212 (2014).

88. Hu, C.-M., Nitta, J., Akazaki, T., Takayanagi, H., Osaka, J., Pfeffer, P. & Zawadzki, W. Zero-field spin splitting in an inverted $In_{0.53}Ga_{0.47}As/In_{0.52}Al_{0.48}As$ heterostructure: Band nonparabolicity influence and the subband dependence. *Phys. Rev. B* **60,** 7736 (1999).

89. Koga, T., Nitta, J., Akazaki, T. & Takayanagi, H. Rashba Spin-Orbit Coupling Probed by the Weak Antilocalization Analysis in InAlAs/InGaAs/InAlAs Quantum Wells as a Function of Quantum Well Asymmetry. *Phys. Rev. Lett.* **89,** 046801 (2002).

90. Schäpers, T., Knobbe, J., van der Hart, A. & Hardtdegen, H. Rashba effect in strained InGaAs/InP quantum wire structures. *Sci. Technol. Adv. Mater.* **4,** 19 (2003).

91. Matsuda, T. & Yoh, K. Enhancement of Spin-Orbit Interaction by Bandgap Engineering in InAs-Based Heterostructures. *J. Electron. Mater.* **37,** 1806 (2008).

92. Sato, Y., Kita, T., Gozu, S. & Yamada, S. Large spontaneous spin splitting in gate-controlled two-dimensional electron gases at normal $In_{0.75}Ga_{0.25}As/In_{0.75}Al_{0.25}As$ heterojunctions. *J. Appl. Phys.* **89,** 8017 (2001).

93. Kunihashi, Y., Nihei, T., Kohda, M. & Nitta, J. Rashba spin-orbit interaction of $In_{0.53}Ga_{0.47}As/In_{0.7}Ga_{0.3}As/In_{0.53}Ga_{0.47}As$ shallow two-dimensional electron gas by surface etching. *Phys. Status Solidi (c)* **5,** 322 (2008).

94. Hao, Y.-F. Spin-orbit interaction in multiple quantum wells. *J. Appl. Phys.* **117,** 013911 (2015).

95. Hao, Y.-F. Spin-orbit modulation by asymmetric quantum wells structure. *Phys. Lett. A* **379,** 2853 (2015).

96. Kohda, M., Bergsten, T. & Nitta, J. Manipulating Spin-Orbit Interaction in Semiconductors. *J. Phys. Soc. Japan* **77,** 031008 (2008).
97. Kunihashi, Y., Kohda, M. & Nitta, J. Experimental demonstration of resonant spin-orbit interaction effect. *Phys. Procedia* **3,** 1261 (2010).
98. Kohda, M. & Nitta, J. Enhancement of spin-orbit interaction and the effect of interface diffusion in quaternary InGaAsP/InGaAs heterostructures. *Phys. Rev. B* **81,** 115118 (2010).
99. Lin, Y., Koga, T. & Nitta, J. Effect of an InP/$In_{0.53}Ga_{0.47}As$ interface on spin-orbit interaction in $In_{0.52}Al_{0.48}As/In_{0.53}Ga_{0.47}As$ heterostructures. *Phys. Rev. B* **71,** 045328 (2005).
100. Hao, Y.-F. Zero field spin splitting in asymmetric quantum wells. *Phys. B: Condens. Matter* **407,** 3622 (2012).
101. Lee, T. Y., Chang, J., Hickey, M. C., Koo, H. C., Kim, H.-j., Han, S. H. & Moodera, J. S. Quantum well thickness dependence of Rashba spin–orbit coupling in the InAs/InGaAs heterostructure. *Appl. Phys. Lett.* **98,** 202504 (2011).
102. Schäpers, T., Guzenko, V. A., Bringer, A., Akabori, M., Hagedorn, M. & Hardtdegen, H. Spin-orbit coupling in $Ga_xIn_{1-x}As$/InP two-dimensional electron gases and quantum wire structures. *Semicond. Sci. Technol.* **24,** 064001 (2009).
103. Prager, M. *Realisation of near-surface two-dimensional electron gases in InAs-based quantum wells* Universität Regensburg. 2018.
104. Speckner, M. *Designing InAs-based quantum wells for epitaxial superconductor-semiconductor heterostructures* Universität Regensburg. 2020.
105. Warren, A. C., Woodall, J. M., Freeouf, J. L., Grischkowsky, D., McInturff, D. T., Melloch, M. R. & Otsuka, N. Arsenic precipitates and the semi-insulating properties of GaAs buffer layers grown by low-temperature molecular beam epitaxy. *Appl. Phys. Lett.* **57,** 1331 (1990).
106. Chen, C.-L., Smith, F., Clifton, B., Mahoney, L., Manfra, M. & Calawa, A. High-power-density GaAs MISFETs with a low-temperature-grown epitaxial layer as the insulator. *IEEE Electron Device Lett.* **12,** 306 (1991).
107. Miller, J. & Low, T. Low-temperature growth of GaAs and AlGaAs by MBE and effects of post-growth thermal annealing. *J. Cryst. Growth* **111,** 30 (1991).
108. Look, D. C. Molecular beam epitaxial GaAs grown at low temperatures. *Thin Solid Films* **231,** 61 (1993).
109. Liu, X., Prasad, A., Chen, W. M., Kurpiewski, A., Stoschek, A., Liliental-Weber, Z. & Weber, E. R. Mechanism responsible for the semi-insulating properties of low-temperature-grown GaAs. *Appl. Phys. Lett.* **65,** 3002 (1994).
110. Missous, M. Stoichiometric low-temperature GaAs and AlGaAs: A reflection high-energy electron-diffraction study. *J. Appl. Phys.* **78,** 4467 (1995).

111. Shojaei, B., O'Malley, P. J. J., Shabani, J., Roushan, P., Schultz, B. D., Lutchyn, R. M., Nayak, C., Martinis, J. M. & Palmstrøm, C. J. Demonstration of gate control of spin splitting in a high-mobility InAs/AlSb two-dimensional electron gas. *Phys. Rev. B* **93,** 075302 (2016).

Acknowledgements

I would like to express my deep gratitude to everybody contributing in any way to this thesis and my work at the university.

First and foremost I would like to thank **Dominique Bougeard** for the opportunity to realize this project in his research team, providing a communicative and supportive environment. Thank you Dominique, for passing on your knowledge and valuable experience, your friendly ear at any time about everything and for all of the discussions we had, whether they were about science or other aspects in life.

I thank **Mariusz Ciorga** for his kind interest in my work as the co-examiner of this thesis and for the fruitful discussions on III/V heterostructures and low-dimensional transport.

A big thank you is dedicated to **Dieter Schuh** as without him this thesis and overall my work would have turned out to be far more complicated. Thank you Didi, for teaching me the high art of III/V MBE growth with all of its voodoo (especially exploiting the moon phases), your experimental experience and the indulgence of good coffee.

I am very grateful to **Andreas Schützenmeier** and **Imke Gronwald** for their constant support and help in all aspects of daily life at the campus. Andi and Imke, you are the backbone of this group, as you keep this machinery running. Thank you for the fun we had over the years.

A huge thank you goes out to **Martin Speckner**, **Jaydean Schmidt** and **Lucia Ebnet** for all of your contributions to my projects and thus to this thesis. Without your effort and time (and patience with me), this would have not been possible. I really enjoyed the time we have spent together and all of our discussions, whether about football referees, bad local transport or house construction.

I would like to thank **Matthias Kronseder** for teaching me MBE growth of metals and oxides. Thank you for all of the discussions we had about everything and everybody including fine guitars and guitar music.

Another humongous thank you is dedicated to **Michaela Trottmann**. Ela, you have taught me everything I know about InAlAs, cleanroom fabrication and electric transport. Without your knowledge and work, especially on InAlAs heterostructures, this project could not have been realized. Thank you for all of the conversations we had.

I want to thank **Paulo Eduardo de Faria Junior** for the numerous discussions about spin-orbit interaction and bandstructure calculations.

I thank **Dieter Weiss** for granting me access to the cleanroom facilities and access to temperature dependent measurements. A huge thank you goes out to **Albert Koop** for his technical assistance with these measurements.

A huge thank you is dedicated to **Christian Haimerl** and **Thomas Solleder** for the constant (and often spontaneous) supply of liquid helium and nitrogen.

I am very grateful to all of the former and current members of our work group I was lucky enough to meet and work with. Thank you for the environment you have created, characterized by steady helpfulness in all aspects. Especially, I have to thank **Maike Halbhuber** and **Thomas Mayer** for all of the time we have spent together in and out of the office and the fun we had over the years. A big shout-out goes to the *Füßikers* including, among already mentioned members, **Viola Zeller**, **Laura Diebel**, **Andreas Schmidbauer**, **Florian Dirnberger** and **Floyd Schauer**. Without all of you, life would have been utterly boring.

Last but not least my deepest gratitude is dedicated to my wife, my parents, my sister and overall my whole family for their constant and endless support in all aspects of life. **Elisa**, you have gifted me **Mimi** and both of you transform every second in a beautiful moment - thank you for your patience with me and my idiosyncrasies.